Control and tracing of ultrafast electron dynamics in dielectric nanoparticles

Qingcao Liu

München 2019

Control and tracing of ultrafast electron dynamics in dielectric nanoparticles

Qingcao Liu

Dissertation
an der Fakultät für Physik
der Ludwig–Maximilians–Universität
München

vorgelegt von
Qingcao Liu
aus Hubei, China

München, den 16. Oktober 2019

Erstgutachter: Prof. Dr. Matthias Kling
Zweitgutachter: Prof. Dr. Jörg Schreiber
Tag der mündlichen Prüfung: 26. November 2019

Zusammenfassung

Diese Arbeit konzentriert sich auf die Interaktion von wellenformgesteuerten ultrakurzen Laserpulsen mit isolierten Siliziumdioxid-Nanopartikeln. Hierbei wurde die ultraschnelle Elektronendynamik untersucht, einschließlich: i) Elektronenstreuung in dem nanoskaligen Festkörper, die auf einer Zeitskala von Attosekunden aufgelöst wird, ii) Steuerung der Elektronenemission aus Nanosphären und iii) Demonstration einer ionisations-induzierten dielektrischen Metallisierung.

Die Streuung von Elektronen in dielektrischen Materialien ist von zentraler Bedeutung für die Laserbearbeitung, lichtgesteuerte Elektronik und für Strahlenschäden. Wir haben die Attosekunden-Schmierbild Technik erstmals auf isolierte Siliziumdioxid-Nanokugeln ausgeweitet und damit Echtzeitmessungen der inelastischen Streuzeit in dielektrischen Materialien ermöglicht. In den Nanopartikeln werden Photoelektronen erzeugt, und sowohl ihr Transport durch das Material als auch ihre Photoemission auf einer Attosekunden-Zeitskala verfolgt. Im Rahmen dieser Arbeit habe ich Folgendes implementiert: Single-Shot-Datenerfassung und Analyse von Velocity-Map Imaging Daten, die es ermöglichen, die aufgezeichnete Anzahl der Elektronen auszuwerten. Es wurde ein theoretischer Rahmen für die Attosekunden-Schmierbild Spektroskopie in Dielektrika entwickelt, der zeigt, dass das Vorhandensein des inneren Feldes im Material den Einfluss der elastischen Streuung aufhebt und die selektive Charakterisierung der inelastischen Streuzeit ermöglicht. Für elektronenkinetische Energien von 20–30 eV wurden in Siliziumdioxid-Nanopartikeln inelastische mittlere freie Weglängen extrahiert. Unser Ansatz ermöglicht die Charakterisierung der inelastischen Streuung in verschiedenen dielektrischen Festkörpern, Clustern und Flüssigkeiten, einschließlich Wasser, das in Form von Tröpfchen untersucht werden kann.

Die Feldlokalisierung durch Nanostrukturen, die mit Laserpulsen mit genau definierter Wellenform interagieren, ermöglicht eine räumlich-zeitliche Kontrolle der Nahfelder mit subzyklen und nanoskaliger Auflösung für die Steuerung der Elektronendynamik. Wir haben intensive, linear polarisierte zweifarbige Laserpulse für die rein optische Kontrolle der Emission hochenergetischer Elektronen aus Siliziumdioxid-Nanopartikeln angewendet. Für das Größenregime, in dem Lichtausbreitungseffekte eine wichtige Rolle spielen, haben wir die Möglichkeit demonstriert, den bevorzugten Emissionswinkel eines beträchtlichen Teils der schnellsten Elektronen durch Variation der relativen Phase des Zweifarbenfelds zu steuern. Trajektorien-basierte semi-klassische Simulationen zeigten, dass für den untersuchten Nanopartikel Größenbereich die Richtungssteuerung auf den Zweifarbeneffekt auf

die Elektronenpropagation zurückzuführen ist. Hingegen hat die Änderung der räumlichen Verteilung der Ionisationsrate auf der Nanopartikeloberfläche nur eine geringe Auswirkung.

Die Interaktion von intensiven Laserpulsen mit nanoskaligen Materialien kann unter extremen Bedingungen Materie weit entfernt vom Gleichgewicht erzeugen. Zu den damit verbundenen Phänomenen mit Relevanz für die Nanoelektronik und -technologien gehören die Metallisierung von Dielektrika, die Erzeugung von harmonischer Strahlung höherer Ordnung und die Erzeugung von Plasmen. In unseren experimentellen Studien verwendeten wir zyklische Pulse mit kontrollierter Träger-Einhüllenden-Phase (carrier-envelope phase, CEP) und unterdrücken damit die Kerndynamik während der Laser-Materie Wechselwirkung. Wir haben die Subzyklus-Elektronendynamik im Zusammenhang mit der Metallisierung von Siliziumdioxid-Nanopartikeln aufgeklärt, die im untersuchten Intensitätsbereich zwischen $10^{14}\,\mathrm{W/cm^2}$ und $4{\times}10^{14}\,\mathrm{W/cm^2}$ auftritt. Die CEP-abhängige Elektronenemission aus den Siliziumdioxid-Nanopartikeln stellt eine empfindliche Sonde für die Metallisierung dar, die oberhalb einer Schwellenintensität von etwa $1.8{\times}10^{14}\,\mathrm{W/cm^2}$ erfolgt. Semiklassische Monte-Carlo-Simulationen decken den physikalischen Mechanismus auf und zeigen, dass der beobachtete rasche Anstieg der Elektronen Grenzenergie mit der Intensität und die charakteristische CEP-abhängige, gerichtete Emission eine Änderung der Elektronendichte innerhalb des Teilchens im Femtosekundenbereich bedeuten. Bei Intensitäten über $3{\times}10^{14}\,\mathrm{W/cm^2}$ führt die Sättigung der Elektronenbeschleunigung zu einer Skalierung der Grenzenergie mit dem 90-100-fachen des ponderomotiven Potentials. Die Ergebnisse weisen darauf hin, dass beschleunigte Elektronen in Feldern mit wenigen Zyklen die elektronische Dynamik von ultraschnellen Phasenübergängen nicht nur für Nanopartikel, sondern auch für Festkörper, einschließlich dünner Schichten oder anderer Nanotargets, die für die Elektronenbeschleunigung mit ultrakurzen Laserpulsen von Bedeutung sind, aufklären können.

Abstract

This work focusses on the interaction of waveform controlled ultra-short laser pulses with isolated silica nanoparticles. Ultrafast electron dynamics had been studied, including: i) electron scattering in the nanosphere resolved on an attosecond timescale, ii) controlling electron emission from nanospheres and iii) ionization-induced dielectric metallization are demonstrated.

The scattering of electrons in dielectric materials is central to laser nanomachining, light-driven electronics and radiation damage. We extended the attosecond streaking metrology to isolated silica nanospheres for the first time, enabling real-time measurements of the inelastic scattering time in dielectric materials. Photoelectrons are generated inside the nanoparticles and both their transport through the material and photoemission are tracked on an attosecond timescale. In the framework of this thesis, I implemented single-shot data acquisition and analysis of velocity-map images, which permits to evaluate the recorded number of electrons. A theoretical framework for attosecond streaking spectroscopy in dielectrics was developed, which shows that the presence of the internal field inside the material cancels the influence of elastic scattering, enabling the selective characterization of the inelastic scattering time. Inelastic mean-free paths were extracted for electron kinetic energies of 20–30 eV in silica nanoparticles. Our approach enables the characterization of inelastic scattering in various dielectric solids, clusters, and liquids, including water, which can be studied in the form of droplets.

Field localization by nanostructures illuminated with laser pulses of well-defined waveform enables spatio-temporal tailoring of the near-fields for sub-cycle control of electron dynamics at the nanoscale. We applied intense linearly-polarized two-color laser pulses for all-optical control of the highest energy electron emission from silica nanoparticles. For the size regime where light propagation effects become important, we demonstrated the possibility to control the preferential emission angle of a considerable fraction of the fastest electrons by varying the relative phase of the two-color field. Trajectory based semi-classical simulations showed that for the investigated nanoparticle size range the directional steering can be attributed to the two-color effect on the electron trajectories, while the accompanied modification of the spatial distribution of the ionization rate on the nanoparticle surface has only a minor effect.

The interaction of intense laser pulses with nanoscale materials can create matter under extreme conditions, far from equilibrium. Among the associated phenomena with relevance for nanoelectronics and -technologies are metallization of dielectrics, generation of higher

order harmonic radiation, and creation of plasma plumes. In our experimental studies, we employed few-cycle pulses with controlled carrier-envelope phase (CEP), and thereby suppress nuclear dynamics during the laser-matter interaction. We elucidated the sub-cycle electron dynamics associated with the metallization of silica nanoparticles that occurs in the investigated intensity range between $10^{14}\,\mathrm{W/cm^2}$ and $4{\times}10^{14}\,\mathrm{W/cm^2}$. The CEP-dependent electron emission from the silica nanoparticles provides a sensitive probe for the metallization, which occurs above a turnover intensity of around $1.8{\times}10^{14}\,\mathrm{W/cm^2}$. Semi-classical Monte-Carlo simulations reveal the physical mechanism, and demonstrate that the observed rapid increase in the electron cutoff energy with intensity and the characteristic CEP-dependent directional emission signify a sub-femtosecond change in electron density inside the particle. At intensities above $3{\times}10^{14}\,\mathrm{W/cm^2}$, metallization results in the cutoff energy scaling with about 90-100 times the ponderomotive potential. The results indicate that accelerated electrons in few-cycle fields can elucidate the sub-cycle electronic dynamics of ultrafast phase transitions, not only for nanoparticles, but also for bulk solids, including thin films or other nanotargets, which are of relevance for few cycle laser driven electron acceleration.

Contents

List of Figures

Chapter 1

Introduction

The conceptual framework for studying time-resolved microscopic phenomena was established before 1900 [1]. The resolution of transient spectroscopy was limited by the development of shorter light flashes. In 1999, Zewail was awarded the Nobel Prize by observing the breakage and formation of chemical bonds in real-time by employing the well developed femtosecond technology [2, 3]. But the temporal resolution was limited to few femtoseconds when the pulse duration approached the oscillation period of the light wave carrying the pulse. In 2001, Krausz reported the first successful generation of light pulses with attosecond time duration, and broke the femtosecond barrier providing real-time access to intraatomic electron dynamics [4]. Nowadays, attosecond pulse trains or isolated attosecond pulses are generated routinely in various labs [5–8]. The time-resolved measurements with attosecond time resolution can be performed by using an isolated attosecond pulse (pump) to excite the system and a delayed femtosecond infrared pulse (probe) to detect the dynamics [9, 10].

The interaction of a dielectric material with photons that have above-bandgap energies inevitably leads to the production of hot electrons propagating through the material. During propagation these electrons can undergo a number of elastic and inelastic scattering events. The inelastic scattering of such electrons can give rise to rapid carrier multiplication via impact ionization, enabling laser nanomachining and limiting the scaling of electronic signal processing towards optical (petahertz-scale) frequencies by dielectric breakdown [9, 11]. Moreover, secondary electrons represent the main source of radiation damage following tissue irradiation. Thus, knowledge of inelastic electron scattering in a dielectric, such as liquid water, is essential to fully understand how radiation affects living organisms [12–14].

To understand the phenomena above, one must be able to study collision dynamics in dielectrics for energies ranging from the bandgap energy up to the hard-X-ray regime. However, methods for measuring collision dynamics have been mostly limited to electron energies above 50 eV [15]. These methods include the measurement of inelastic mean-free paths (IMFPs), where a mean-free path is the average distance that an electron will travel in a solid between adjacent collision events. Standard IMFP measurements are based on the dielectric description of inelastic scattering of charged particles in condensed

matter and elastic peak electron spectroscopy [16]. While progress has been made toward determining IMFPs for very low kinetic energy (of a few electronvolts) by angle-resolved photoelectron spectroscopy [17], data in the tens-of-electronvolt range, where the impact ionization of valence band electrons strongly dominates the IMFP, are largely missing. Moreover, amorphous dielectric solids such as SiO_2 and liquid water, which can be accessed with our approach, are challenging for rigorous ab initio calculations of IMFPs. For electron energies in the tens-of-electronvolt range, collisions typically occur in the sub-femtosecond range.

To date, attosecond streaking metrology has been successfully applied to metals or adlayer-covered metals [18–27], where the NIR streaking field takes effect only on the surface of the material. The physics for dielectrics, however, is fundamentally different as the released electrons are streaked by the NIR field also inside the solid. Most importantly, until now accumulative charging induced by the XUV pulse has prevented the application of attosecond streaking to dielectrics. We solve this problem by using a continuous stream of nanoscopic targets. By merging the attosecond streaking metrology and nanoparticle aerosol generation technology, the proof-of-concept study on attosecond chronoscopy of electron scattering in 50 nm SiO_2 nanoparticles has been carried out. The single shot detection and data discrimination enables recording attosecond photoemission from aerosolized nanotargets and the gas at the very same experimental conditions. The gas thereby provides a temporal ruler, which permits relative attosecond streaking delay measurements with isolated nanotargets.

Ultrafast intense laser pulses with tailored waveforms have proven to be a powerful tool for the control of electron dynamics in atomic, molecular, and solid targets [28–38]. The laser electric field of such pulses exerts a force that varies on the attosecond time scale for visible light and enables the steering of electron motion on sub-cycle time scales and on nanometre spatial dimensions [9, 39–42]. Nanostructures can concentrate laser light in highly localized near-fields with dimensions below the incident wavelength [43]. The intrinsic time and length scales naturally merge the ultrafast science and nanoscale physics. Ultrafast phenomena on the nanoscale enables unprecedented insights into fundamental electronic processes in solids while ultrafast laser pulses can be employed to probe electronice behavior, e.g. plasmonic energy localization, electron scattering, the skin effect and the steering of electronic matter waves [40, 42, 44, 45]. Furthermore, the electronic response of the optically driven nanostructures could lead to new ultrafast and highly-nonlinear effects such as ultrafast plasmonics, high-harmonic generation in nanoscopic volumes and electron-based signal processing at optical frequencies [41, 46, 47].

Recently, Süßmann *et al.* reported field propagation-induced tunability of the emission direction of fast recollision electrons by illuminating silica nanospheres with a series of diameters with CEP controlled few-cycle laser pulses [48]. We demonstrated an effective yet simple way of realizing this control by combining the fundamental laser pulse with its second harmonic pulse [32, 38, 49–52]. The relative phase between two laser fields of different frequencies entails the ability to control and shape not only the envelopes of the laser pulses but also the sub-cycle structure of the field oscillations. Tailored optical fields in combination with propagation effects in isolated nanostructures permit all-optical spatio-

temporal control of electron emission from silica nanospheres. Insight into the resulting changes in the photoelectron spectra helped identify certain ionization scenarios. The angular and phase-resolved electron cutoffs reveal how the nanofocusing induced a near-field directionality and the tailored near-field driven electron dynamics.

Ultrashort laser pulses with a few optical oscillations open up routes to study strong field phenomena in solids during periods of time too short for the lattice ions to move significantly [41]. The nonlinear response of solid materials to excitation with ultrashort, intense laser fields has become a subject of extensive research [9]. Recent ab-initio calculations [53] have reproduced the Zener breakdown in silica induced by a laser pulse of intensity $10^{15}\,\mathrm{W/cm^2}$. Optical fields can drive (nanoscale) solids far from equilibrium leading to the generation of higher order harmonic radiation [54, 55]. They can also cause a reduction of the band gap in semiconductors and insulators [56–58], leading to the control of macroscopic currents [59], and opening up a perspective for petahertz nanoelectronics [9]. At intensities, where carrier generation and carrier avalanching dominate the nonlinear response, rapid plasma formation initiated by femtosecond laser pulses occurs and forms the basis for nanomachining [11].

The field of optical breakdown has been studied extensively with respect to laser ablation and the damage thresholds of bulk dielectrics [11, 60–62]. As the measurement of ablation depths and efficiencies is a rather indirect method, it is desirable to have more direct experimental access to the processes involving charge carrier creation. Recently, Schultze *et al.* could observe a reversible 10 % increase of the XUV transmittance through a bulk SiO_2 sample at an NIR field strength of $2.5\,\mathrm{V/Å}$[59]. At very similar intensities, Schiffrin *et al.* could measure a CEP dependent current across a bulk SiO_2 sample [59]. It was concluded that charge carrier injection happens on a time scale shorter than an optical half-cycle. The insulator-to-metal transition in nanoscale materials at intensities above $10^{14}\,\mathrm{W/cm^2}$ has been explored via IR-pump / X-ray diffraction probe experiments at the free electron laser LCLS [63, 64]. These studies have shown that femtosecond laser irradiation of Xe clusters leads to the generation of an overdense material with successive surface softening. The corresponding dynamics were predicted theoretically employing microscopic particle-in-cell (MicPIC) simulations [65]. Experimental studies of insulator-to-metal transitions in clusters thus far were, however, limited to the nuclear dynamics on timescales of hundreds of femtoseconds, where the much faster electron dynamics could not be resolved.

Field localization in nanostructured materials allows control of electron acceleration in strong optical fields that can be tailored on sub-wavelength spatial and attosecond temporal scales. Enhanced strong-field electron acceleration in nanolocalized fields has been explored for isolated nanoparticles [48, 66–68], nanotips [69–73], and surface based nanostructures [74]. At intensities below $10^{14}\,\mathrm{W/cm^2}$, a variety of effects have been discovered that contribute to the electron acceleration and determine the cutoff of the electron spectrum. These include the modification of elastic electron backscattering by field enhancement [75], nanofocusing [48], as well as local and non-local charge interactions [75, 76]. For SiO_2 nanoparticles in this intensity regime, cutoff energies up to about 50 times ponderomotive potential were observed [66–68]. We elucidated the sub-cycle electron dynamics associated

with the metallization of SiO_2 nanoparticles that occurs in the investigated intensity range between $10^{14}\,W/cm^2$ and $4\times10^{14}\,W/cm^2$. The CEP-controlled few-cycle pulses suppress nuclear dynamics during the laser-matter interaction enabling the probing of the ultrafast insulator-to-metal transition in SiO_2 nanoparticles via recording the CEP-dependent electron emission. Simulations reveal the physical origin and relevant time scale of the phase transition.

This thesis is organized as follows. In Chapter 2 the most central theoretical backgrounds for describing the interaction of laser light with nanospheres are presented. The experimental techniques and data analysis methods are described in detail in Chapter 3. From Chapter 4 to Chapter 6, a series of investigations on the interaction of waveform controlled ultra-short laser pulses with isolated silica nanoparticles are presented. Chapter 4 contains the results of attosecond streaking metrology for isolated silica nanospheres. Chapter 5 reports the all-optical spatio-temporal control of electron emission from SiO_2 nanospheres with an intense linearly-polarized femtosecond two-color laser field. Chapter 6 focuses on the sub-cycle electron dynamics associated with metallization of SiO_2 nanoparticles probed via CEP-dependent electron acceleration.

Publications with relevance to the work presented in this thesis

[1] Attosecond chronoscopy of electron scattering in dielectric nanoparticles

L. Seiffert, Q. Liu, S. Zherebtsov, A. Trabattoni, P. Rupp, M. C. Castrovilli, M. Galli, F. Süßmann, K.Wintersperger, J. Stierle, G. Sansone, L. Poletto, F. Frassetto, I. Halfpap, V. Mondes, C. Graf, E. Rühl, F. Krausz, M. Nisoli, T. Fennel, F. Calegari and M. F. Kling

Nature Physics, **13**, 766 (2017)

[2] Photoemission from Nanomaterials in Strong Few-Cycle Laser Fields

Q. Liu, P. Rupp, B. Förg, J. Schötz, F. Süßmann, W. Okell, J. Passig, J. Tiggesbäumker, K. H. Meiwes-Broer, L. Seiffert, T. Fennel, E. Rühl, M. Förster, P. Hommelhoff, S. Zherebtsov and M. F. Kling

Nano-Optics: Principles Enabling Basic Research and Applications, **104302**, 283 (2017)

[3] Attosecond streaking metrology with isolated nanotargets

Q. Liu, L. Seiffert, A. Trabattoni, M. C. Castrovilli, M. Galli, P. Rupp, F. Frassetto, L. Poletto, M. Nisoli, E. Rühl, F. Krausz, T. Fennel, S. Zherebtsov, F. Calegari and M. F. Kling

Journal of Optics, **20**, 024002 (2018)

[4] All-optical spatio-temporal control of electron emission from SiO_2 nanospheres with femtosecond two-color laser fields

Q. Liu, S. Zherebtsov, L. Seiffert, S. Skruszewicz, D. Zietlow, S. Ahn, P. Rupp, P. Wnuk, S. Sun, A. Kessel, S. Trushin, A. Schlander, D. Kim, E. Rühl, M. F. Ciappina, J. Tiggesbäumker, M. Gallei, T. Fennel, M. F. Kling

New Journal of Physics, **21**, 073011 (2019)

[5] Interplay of pulse duration, peak intensity, and particle size in laser-driven electron emission from silica nanospheres

J. A. Powell, A. M. Summers, Q. Liu, S. J. Robatjazi, P. Rupp, J. Stierle, C. Trallero-Herrero, M. F. Kling and A. Rudenko

Optics Express, **27**, 027124 (2019)

[6] Sub-cycle metallization of SiO_2 nanoparticles probed via carrier-envelope phase dependent electron acceleration

Q. Liu, S. Zherebtsov, F. Süßmann, J. Passig, L. Seiffert, V. Mondes, A. Kessel, S. Trushin, C. Graf, E. Rühl, J. Tiggesbäumker, K. H. Meiwes-Broer, M. I. Stockman, L. Veisz, T. Fennel and M. F. Kling

In preparation (2019)

Other publications

[7] Quenching of material dependence in few-cycle driven electron acceleration from nanoparticles under many-particle charge interaction

P. Rupp, L. Seiffert, Q. Liu, F. Süßmann, B. Ahn, B. Förg, C. G. Schäfer, M. Gallei, V. Mondes, A. Kessel, S. Trushin, C. Graf, E. Rühl, J. Lee, M. S. Kim, D. E. Kim, T. Fennel, M. F. Kling and S. Zherebtsov

Journal of Modern Optics, **64**, 995 (2017)

[8] Sub-cycle steering of the deprotonation of acetylene by intense few-cycle mid-infrared laser fields

H. Li, Nora G. Kling, T. Gaumnitz, C. Burger, R. Siemering, J. Schötz, Q. Liu, L. Ban, Y. Pertot, J. Wu, A. M. Azzeer, R. de Vivie-Riedle, H. J. Wörner, and M. F. Kling

Optics Express, **25**, 14192 (2017)

Chapter 2

Theoretical background

2.1 Few-cycle laser pulses

In 1960, Theodore Maiman observed the generation of coherent light via stimulated emission from the solid-state pink ruby laser. Laser technology has made enormous progress since then. The increase of the spectral bandwidth and consequently the reduction of the pulse duration permit generation of ultrashort laser pulses consisting of only few oscillations of the optical field. Such few-cycle pulses enable time-resolved studies of ultrafast processes in atoms and molecules [77–79]. Amplification of such few-cycle pulses provides sufficient energy to drive highly-nonlinear processes in gases such as high harmonic and attosecond pulse generation, opening the door to a whole variety of new applications [28, 80–82].

The electric field of a laser pulse can be described as

$$\mathbf{E}(t) = \mathbf{E_0} \cos\left(\omega t + \varphi_{\mathrm{ce}}\right) \exp\left[-2\ \ln 2\ (t/\tau)^2\right]. \tag{2.1}$$

Here, $\mathbf{E_0}$ is the peak electric field amplitude, ω is the carrier frequency, φ_{ce} is the carrier-envelope phase (CEP) and τ is the pulse length (full-width-half-maximum, FWHM). The CEP is the difference between the phase of the carrier wave and the envelope position. For few cycle laser pulses where the pulse length is on the order of the period of an optical cycle $\mathrm{T} = 2\pi/\omega$, the CEP strongly governs the field evolution during the pulse and permits to manipulate the motion of electrons on sub-femtosecond timescales [28, 59, 77, 83–85]. Figure 2.1(a) shows electric field with different CEPs. The pulse length τ is 4 fs (1 fs = $1 \times 10^{-15} s$), and the optical cycle T is 2.4 fs which corresponds to a laser wavelength of 720 nm.

In strong field applications, the ponderomotive potential is a relevant quantity for electron dynamics in an oscillating electric field. The ponderomotive potential is defined as the average oscillation energy that is acquired by a free electron in the field of the laser pulse, and is given by:

$$U_p\,[e\mathrm{V}] = \frac{e^2 E_0^2}{4 m_{\mathrm{e}} \omega^2} = 9.337 \times 10^{-20} \times (\lambda\ [\mathrm{nm}])^2 \times\ I\left[W/cm^2\right], \tag{2.2}$$

where e is the electron charge, m_e is the mass of the electron, ω is the angular frequency of the laser radiation, λ is the central wavelength, and I is the laser field intensity. The ponderomotive potential (figure 2.1(b)) is linearly dependent on the laser intensity and proportional to the square of the wavelength. Interestingly, the ponderomotive potential is independent of the sign of the particle's charge, thus all charged particles are expelled from high laser intensity regions to lower intensity regions.

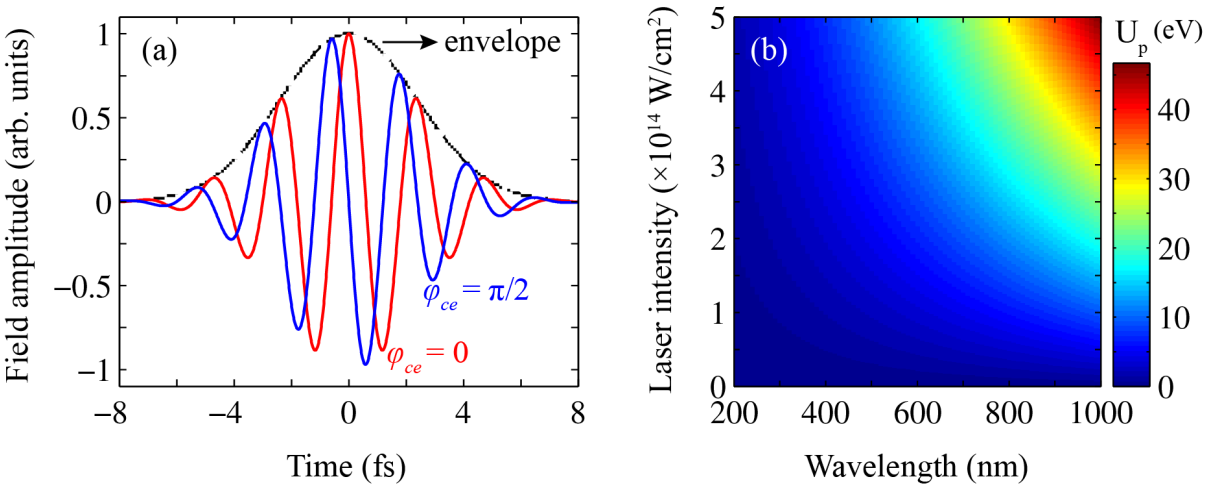

Figure 2.1: (a) Electric field of a 4 fs few-cycle laser pulse with different CEPs. (b) Ponderomotive potential as a function of laser intensity and wavelength.

2.2 Strong-field photoionization

The development of ultrashort intense laser technology accelerates the studies on light-matter interactions [80, 86–89]. State-of-the-art laser systems can deliver ultrashort laser pulses with a pulse duration less than tens of femtoseconds and a peak power at the Terawatt (1 terawatt $= 1\times10^{12}$ watt) level [90, 91]. The focused laser intensity is sufficiently strong and competes the Coulomb electric field that binds electrons to the nuclei. The relationship between the laser intensity I, and the electric field strength E is ruled by

$$I = \frac{1}{2}\varepsilon_0 c E^2 \tag{2.3}$$

where ε is the dielectric constant and c the speed of light in vacuum. For short, $I = 1.33\times10^{-3}E^2$ or $E = 27.4\sqrt{I}$ when I is in the unit of W/cm^2, and E in V/cm. The Coulomb electric field in a hydrogen atom is $E \simeq 5\times10^9 V/cm$, corresponding to an intensity of $I = 3.51\times10^{16} W/cm^2$. With such a strong electric field in the visible wavelength range, the electron can be accelerated to a velocity of $0.01c$. Since the typical velocity is much

less than speed of light the influence of the magnetic field on the electron dynamics can be neglected and in the rest of the thesis only the electric field of the laser pulse is considered.

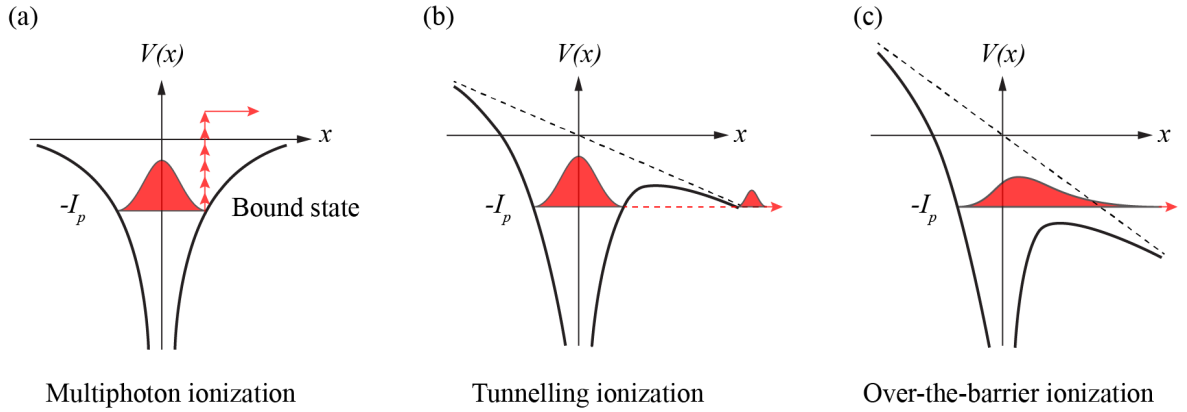

Figure 2.2: Schematic diagram showing the three possible mechanisms for ionization at low (a), intermediate (b) and high (c) laser intensities.

An adiabatic parameter γ from the theoretical work defined by Keldysh is an approximate indicator to distinguish the different ionization mechanisms. It is given by

$$\gamma = \sqrt{\frac{I_\mathrm{p}}{2U_\mathrm{p}}}, \tag{2.4}$$

where U_p is the ponderomotive potential as defined in Eq. 2.2. When the electric field strength of the incident laser is smaller than the Coulomb electric field (*e.g.* with a low laser intensity and/or a high laser frequency) where $\gamma > 1$, multiphoton ionization will be most significant. When $\gamma < 1$ (a high laser intensity and/or a low laser frequency), tunneling ionization or over-the barrier ionization will dominate.

Photoionization plays a crucial role in modelling the interaction of ultrashort intense laser pulses with matter. Three ionization mechanisms are briefly summarized as following:

(1) Multiphoton ionization (MPI). At modest intensities ($I < 10^{14}\mathrm{W/cm^2}$) when the atomic potential is barely affected by the incident laser field (as shown in Fig. 2.2(a)), the electron can be ionized through multiphoton ionization [92, 93]. The energy of the photoelectron can be expressed as

$$E_\mathrm{kin} = n\hbar\omega - I_p, \tag{2.5}$$

where n is the minimum number of absorbed photons required to overcome the atomic potential I_p (as illustrated in Fig. 2.2(a)). The lowest-order perturbation theory (LOPT) predicts that the n-photon ionization rate scales with the corresponding power of the laser intensity as $W^\mathrm{n}_\mathrm{MPI} = \sigma_n I^n$, where σ_n is the generalized cross section [94, 95]. When the field-induced distortion of the atomic potential is not negligible, where the absorption of photons

by the exiting photoionizing electron still under the influence of the atomic potential. It results to more photons than the minimum required number being absorbed during the ionization, called above-threshold ionization (ATI) [96, 97]. Perturbation theory has been employed to model ATI rates with further generalization of Eq. 2.5:

$$W_{\mathrm{ATI}}^{\mathrm{n+s}} \propto I^{\mathrm{n+s}}, \tag{2.6}$$

where s is number of above-threshold photons absorbed [94, 98]. The energy of photoelectrons is given by

$$E_{\mathrm{kin}}^{\mathrm{s}} = (n+s)\hbar\omega - I_p. \tag{2.7}$$

(2) Tunneling ionization (TI). If the incident laser field is strong enough, the instantaneous electric field (dashed line in Fig. 2.2(b)) is able to distort the atomic potential. A potential barrier with finite width is formed which the electron can tunnel through within a quasi-stationary approximation. The ionization occurs in a fraction of an optical cycle, therefore the electric field can be considered as quasi-static. The analytic calculation of instantaneous ionization rate was given by the ADK theory as

$$W_{\mathrm{ADK}} = C_{n^*}^2 f(l,m) \frac{Z^2}{2n^{*2}} \sqrt{\frac{3E(t)n^{*3}}{\pi Z^3}} \left(\frac{2Z^3}{E(t)n^{*3}}\right)^{2n^*-|m|-1} \exp\left(-\frac{2Z^3}{3n^{*3}E(t)}\right), \tag{2.8}$$

where $C_{n^*} = (2e/n^*)^{n^*}(2\pi n^*)^{-1/2}$, $E(t)$ is the amplitude of the laser electric field, n^* is the effective quantum number $Z/(2I_{\mathrm{p}})^{1/2}$, $e \simeq 2.71828$ is a mathematical constant, l and m are the azimuthal and magnetic quantum numbers. For circularly polarized laser pulses, an additional term $(\pi Z^3/3E(t)n^{*3})^{1/2}$ need to be multiplied [99]. The tunneling ionization in intense field has proven to be a crucial element in current theories of strong-field physics [92, 100–105].

(3) Over-the-barrier ionization (OTBI). As the incident laser field strength is increased even stronger ($I > 10^{15}\,\mathrm{W/cm^2}$), the gradient of the potential becomes increasingly more negative and the barrier narrower and lower (as shown in Fig. 2.2(c)). The ground state is no longer bound while the peak of the barrier is lower than $-I_{\mathrm{p}}$, where I_{p} is the ionization potential. The critical electric field where OTBI takes place is obtained by equating the saddle-point (local maximum as shown in Fig. 2.2(b)) energy induced by the laser field in the atomic potential to the binding energy. The critical electric field for OTBI leads to a critical laser intensity

$$I_{\mathrm{OTBI}}[\mathrm{W/cm^2}] = 4 \times 10^9 (\mathrm{I_p[eV]})^4 \mathrm{Z}^2, \tag{2.9}$$

where Z is the charge state of the relevant atom or ion.

2.3 Semiclassical modeling of strong field-matter interaction

The classical picture of strong-field-induced ionization dynamics is usually intuitively described by the famous simple man‘s model (SMM) [106]. It states that photoionization can

be described as three-step process. Once ionization removes an electron from an atom or a molecule through the potential barrier, the freed electron acts as a classical point charge in the strong oscillating laser field. The electron's motion during these oscillations depends on the phase of the electric field $E_L(t)$ at which ionization has occurred, see the inset in figure 2.3. Newton's equations of motion show that, the electron is first strongly accelerated away from the ion and within one or a few cycles after ionization driven back when the laser field reverses its direction. The electron may escape as free electron (above-threshold ionization) or return to the parent ion. During the reencounter, also called recollision, a consequence of processes may take place as illustrated in figure 2.2 (i) the electron is scattered elastically and emitted as energetic electron [82, 107]; (ii) the electron returns to the vicinity of its parent ion and recombines to its ground state. The energy it carries can be emitted as a high energy photon. This process is known as high harmonic generation (HHG), since the produced photons are harmonics of the fundamental driving laser field [8, 28]; (iii, iv) the electron is scattered inelastically leading to electron impact excitation or ionization of the parent ion. This is often called non-sequential double ionization (NSDI) [108, 109]. The three-step model reveals the heart of strong field science, the key of high-harmonic spectroscopy and the generation of attosecond XUV pulses: field-driven recollision and the recombination of the accelerated electron with the ion.

In order to calculate the electron trajectory and the kinetic energy cutoff in a certain laser field, we need to know the initial conditions for the electron right after ionization. These conditions are specified within the simple man's model, which makes the following assumptions:

1. The single active electron approximation (SAE). It assumes that only one electron actively participates in the ionization of the atom or molecule by the low frequency laser field [110, 111].
2. The electron is born in the continuum at any time within the laser cycle, t_b.
3. The electron is born near the ionic core with zero initial momentum, $p(t_b) = 0$.
4. The Coulomb attraction to the parent ion is neglectable [28].

After ionization, the electron momentum and position at times $t > t_b$ are given by

$$p(t > t_b) = -\int_{t_b}^{t} dt' E(t') = A(t) - A(t_b), \tag{2.10}$$

$$r(t) = \int_{t_b}^{t} dt' A(t') - A(t_b)(t - t_b) = \alpha(t) - \alpha(t_b) - A(t_b)(t - t_b). \tag{2.11}$$

Here $A(t)$ is the vector potential of the laser field and $A(0) = A(T_\mathrm{p}) = 0$, $\alpha(t)$ is the excursion, T_p is the laser pulse duration. The final drift momentum of "direct" electrons are given by the vector potential at the time of ionization, $p(\infty) = -A(t_b)$, so that the final energy is

$$\xi(\infty) = \frac{1}{2} A^2(t_b) \leq 2U_\mathrm{p}. \tag{2.12}$$

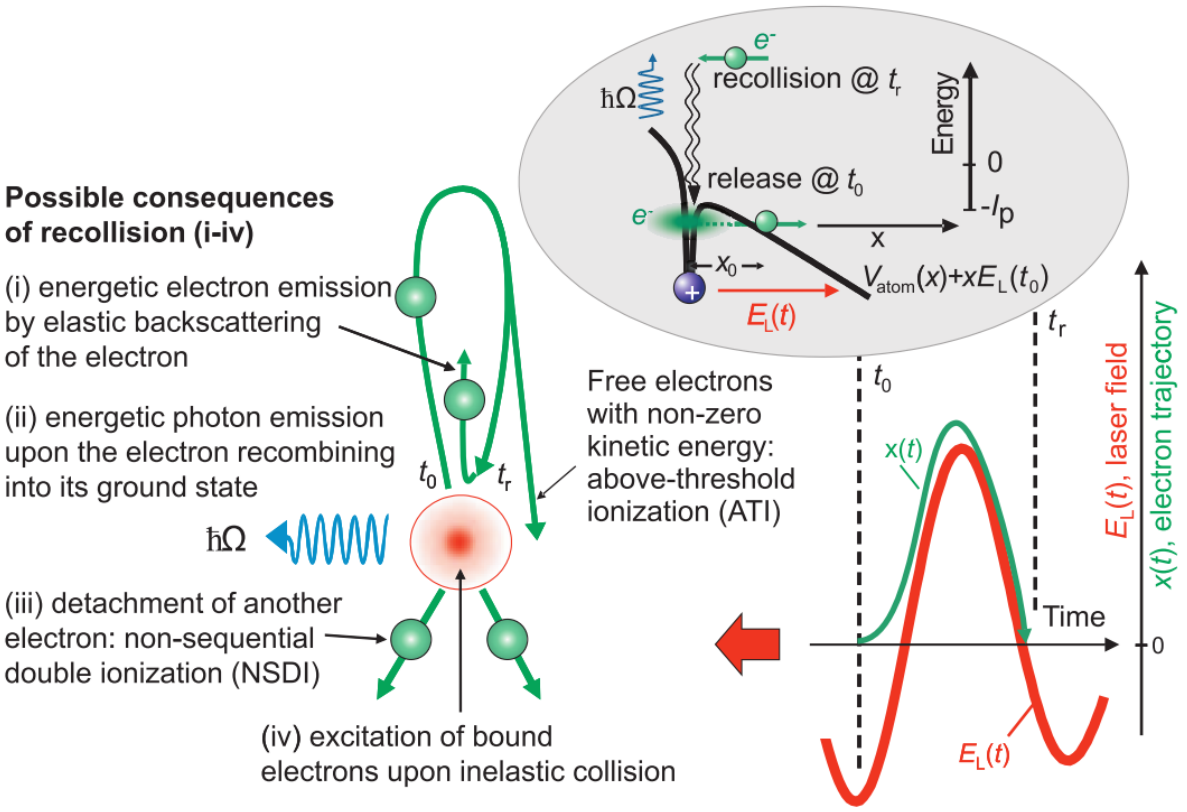

Figure 2.3: Optical field ionization of an atom (at moment t_b) and subsequent recollision of the detached electron (at moment t_r) with the parent ion in a strong, linearly polarized ultrashort-pulsed laser field. (i) - (iv) Possible consequences of recollision. Inset: Release and recollision of electron that returns with highest energy to the parent ion, resulting - via process (ii) - in the highest-energy photons emitted. Taken from [28].

The "direct" electrons are classically restricted to energies up to $2U_\mathrm{p}$. This limit is known as the classical cut-off energy for "direct" electrons in strong field physics.

If we consider one rescattering event upon the recollision, i.e., at the time t_resc the electron returns to the parent ion. By elastically scattering off the parent ion with 180° in back-reflection, the electron changes the sign of its momentum and is accelerated further in the laser field. The electron momentum at later time is given by

$$p_1\left(t > t_\mathrm{resc}\right]) = A\left(t\right) - 2A\left(t_\mathrm{resc}\right) + A\left(t_\mathrm{b}\right), \tag{2.13}$$

thus the final momentum is $p_1\left(T_b\right) = A\left(t_b\right) - 2A\left(t_\mathrm{resc}\right)$, and the final kinetic energy is

$$\xi_1\left(\infty\right) = \frac{1}{2}[A\left(t_\mathrm{b}\right) - 2A\left(t_\mathrm{resc}\right)]^2 \leq 10U_\mathrm{p}. \tag{2.14}$$

The maximum energy of the rescattered electron is $10U_p$, which corresponds to the cut-off energy of the measured photoelectron spectra [112].

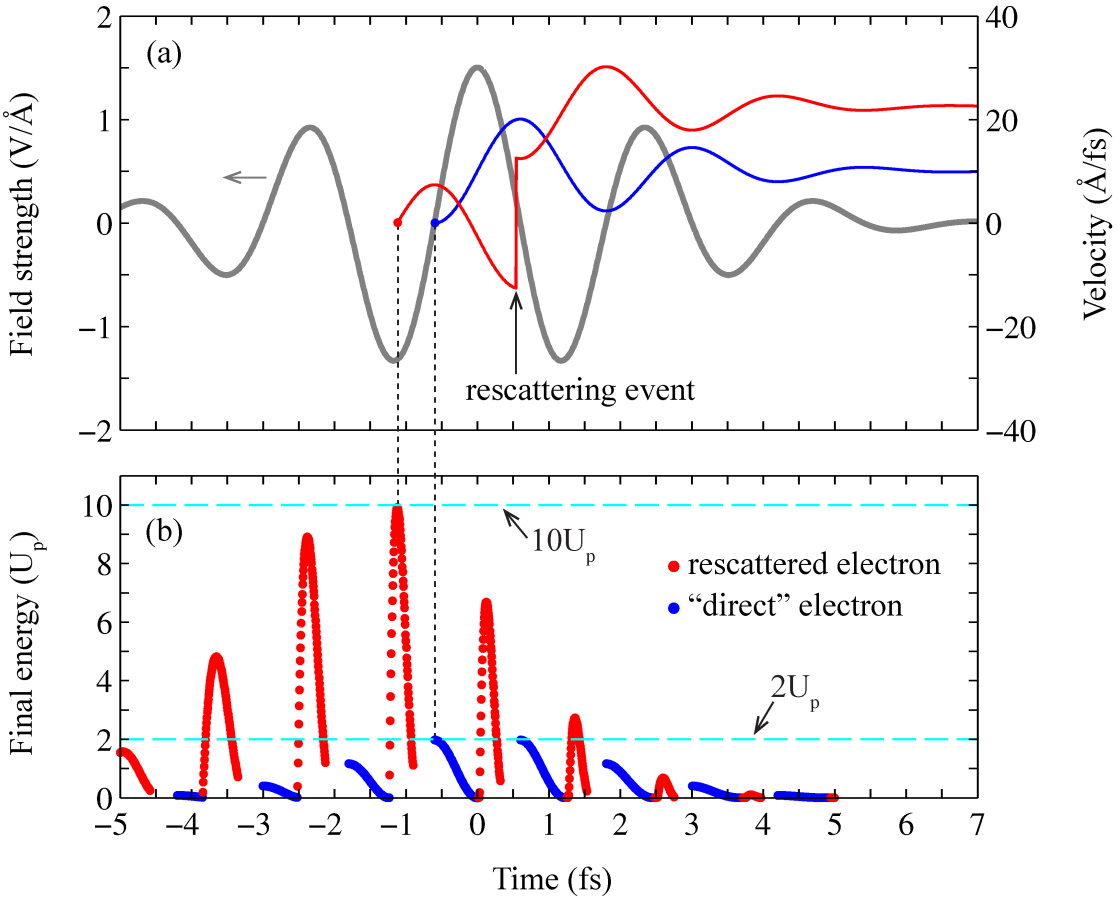

Figure 2.4: (a) Temporal variation of the electron velocity component parallel to the linearly polarized electric field (grey line) for typical "direct" electrons (blue line) and rescattered electrons (red line). (b) Final energies of "direct" electrons (blue dot) and rescattered electrons (red dot) those are released at different moments. The cyan dashed lines indicate the classical $2U_\mathrm{p}$ and $10U_\mathrm{p}$ cut-off energies.

Figure 2.4(a) shows the temporal variation of the electron velocity for two different release times. The driving electric field (gray line) is linearly polarized and defined in Eq. 2.1. The oscillating period of the field is $T_\mathrm{osc} = 2.4$ fs, which corresponds to a wavelength of 720 nm. The rescattered electron (red line) is born at about $T_\mathrm{osc}/20$ after one of the peaks of the electric filed and elastically back scattered at about $2T_\mathrm{osc}/3$ after the release. This electron gains more energy from the driving field and the final energy reaches up to $10U_p$. Figure 2.4(b) shows the final energies of electrons those were released at different times. The cutoff energies of the "direct" electrons and rescattered electrons are $2U_\mathrm{p}$ and $10U_\mathrm{p}$, respectively.

2.4 M^{3}C model

When an atom is exposured to an intense linearly polarized laser pulse, the dynamics of a single atomic electron can be modelled precisely by solving the time dependent Schrödinger equation (1D-TDSE). The interaction of intense laser pulses with complex matter, such as a larger molecule, liquid droplet, cluster and nanosphere, involves collective electron dynamics. A quantum simulation is out of reach for a detailed description of complex geometries, coupled with realistic near-fields. Furthermore, the electron scattering inside the material and multi-electron effects complicate the quantum mechanical treatment.

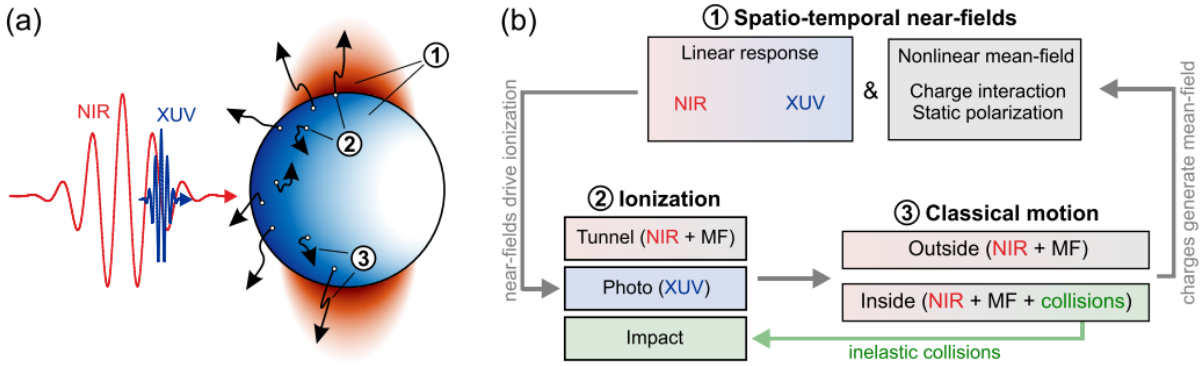

Figure 2.5: Illustration (a) and visualization (b) of a typical M^{3}C simulation scenario. The model contains spatio-temporal near-fields (red and blue shades), ionization channels (white dots) and classical trajectory motion (black arrows). Taken from [113].

In order to achieve quantitative accuracy for laser-nanoparticle interaction, T. Fennel *et al.* coupled the near-field, ionization, and scattering models into the classical trajectory Monte-Carlo scheme as illustrated schematically in Fig. 2.5 [113]. The name for the quasi-classical model M^{3}C stands for Mean field, Mie theory, and Monte Carlo. The model contains three key ingredients: (1) spatio-temporal near-fields, (2) ionization channels and (3) classical trajectory motion. The M^{3}C model had been successfully employed to describe a series of laser-nanosphere interaction experiments [42, 48, 67, 68, 75, 76, 114], in particular, the model unraveled a novel acceleration mechanism from dielectric nanospheres with intense ultrashort laser fields [68], identified the field propagation-induced directionality of CEP-controlled photoemission from nanospheres [48, 76], and revealed the dynamics of electron scattering in dielectric nanoparticles in real time [42, 114].

In the M^{3}C model, the electromagnetic response of the nanoparticle (red and blue in Fig. 2.5(a)) is calculated using the analytically correct Mie solution (subsection 2.4.1). Electron trajectories can be generated via Monte-Carlo sampling (white dots in Fig. 2.5(a)) of the surface tunnel ionization (subsection 2.4.3), photoionization (subsection 2.4.4) and/or impact ionization (subsection 2.4.5). Electron trajectories are calculated by integration of

classical equations of motion in an effective electric field (subsection 2.4.6) in 3D space. The mean-field describes the Coulomb interaction with free charges (electrons and residual ions) in the presence of the dielectric sphere via high-order multipole expansion 2.4.7. Elastic electron-atom collisions are described by isotropic scattering events using an energy-dependent mean free path. Inelastic collisions are modelled with Lotz's electron impact ionization cross-sections (subsection 2.4.8).

2.4.1 Mie theory of spherical particles

The solution of scattering of a plane wave at a sphere has been discussed by the electromagnetic scattering theory [115, 116]. Gustav Mie introduced an analytical solution to Maxwell's equations in the spherical coordinate frame in 1908, and enabled a precise description of the electric field evolution surrounding a sphere [117].

The macroscopic Maxwell equations describe the evolution of the linear response fields of a neutral medium without free charges and currents placed in an external electromagnetic field [115]:

$$\begin{aligned} \nabla \cdot \mathbf{D} &= 0 \\ \nabla \cdot \mathbf{B} &= 0 \\ \nabla \times \mathbf{E} &= -\dot{\mathbf{B}} \\ \nabla \times \mathbf{H} &= \dot{\mathbf{D}}, \end{aligned} \tag{2.15}$$

where $\mathbf{E}$ is the electric field, $\mathbf{D}$ is the displacement field, $\mathbf{B}$ is the magnetic field strength, and $\mathbf{H}$ is the magnetizing field. For a homogeneous, linear response and isotropic medium, the constitutive relations are

$$\begin{aligned} \mathbf{D} &= \varepsilon_0 \varepsilon_r \mathbf{E} \\ \mathbf{B} &= \mu_0 \mu_r \mathbf{H}, \end{aligned} \tag{2.16}$$

where ε_0 and μ_0 are the permittivity and permeability of free space, respectively. ε_r and μ_r are the constant relative permittivity and relative permeability of the medium, respectively. Eq. 2.15 and 2.16 can derive the Helmholtz equations

$$\begin{aligned} \left[\nabla^2 - \frac{1}{c^2}\frac{\partial^2}{\partial t^2}\right]\mathbf{E} &= 0 \\ \left[\nabla^2 - \frac{1}{c^2}\frac{\partial^2}{\partial t^2}\right]\mathbf{H} &= 0, \end{aligned} \tag{2.17}$$

where ∇^2 is the Laplacian and $c = 1/\sqrt{\varepsilon_0 \varepsilon_r \mu_0 \mu_r}$ is the speed of light in the medium. An incident plane wave can be written as

$$\begin{aligned} \mathbf{E}(\mathbf{r}, t) &= \mathbf{E}_0 e^{i(\kappa \mathbf{r} \pm \omega t)} \\ \mathbf{H}(\mathbf{r}, t) &= \mathbf{H}_0 e^{i(\kappa \mathbf{r} \pm \omega t)}, \end{aligned} \tag{2.18}$$

where the wave number $\kappa = \omega/c$, and ω is the angular frequency. We can derive the wave equations as

$$\begin{aligned} \nabla^2\mathbf{E} + \kappa^2\mathbf{E} &= 0 \\ \nabla^2\mathbf{H} + \kappa^2\mathbf{H} &= 0. \end{aligned} \tag{2.19}$$

Due to the spherical symmetry in the spherical coordinate frame, the wave equations can be translated to a simpler one by constructing two vector functions

$$\mathbf{M} = \nabla \times (\mathbf{r}\psi), \qquad \mathbf{N} = \frac{\nabla \times \mathbf{M}}{k}, \tag{2.20}$$

where $\mathbf{r}$ is an arbitrary constant vector and ψ is a scalar function. The vector functions in Eq. 2.20 satisfy the wave equations in Eq. 2.19 if ψ is a solution to the scalar wave equation in spherical coordinates:

$$\frac{1}{r^2}\frac{\partial}{\partial r}\big(r^2\frac{\partial\psi}{\partial r}\big) + \frac{1}{r^2\sin(\theta)}\frac{\partial}{\partial\theta}\Big(\sin(\theta)\frac{\partial\psi}{\partial\theta}\Big) + \frac{1}{\sin^2(\theta)}\frac{\partial^2\psi}{\partial\phi^2} + k^2\psi = 0. \tag{2.21}$$

The complete set of vector harmonics $\mathbf{M}$ and $\mathbf{N}$ can be constructed from the solution of a single scalar wave equation. By separating the variables with $\psi(r,\theta,\phi) = R(r)\Theta(\theta)\Phi(\phi)$, one can yield two linearly independent odd and even solutions to the generating functions

$$\begin{aligned} \psi_{emn} &= \cos(m\phi)P_n^m(\cos\theta)z_n(kr) \\ \psi_{omn} &= \sin(m\phi)P_n^m(\cos\theta)z_n(kr), \end{aligned} \tag{2.22}$$

where $P_n^m(\cos\theta)$ are the associated Legendre functions of the first kind with degree n and order m, $z_n(kr)$ is any of the four spherical Bessel functions.

For a plane wave scattered by sphere, the fields at a point outside the sphere can be decomposed into the incident fields $(\mathbf{E}_i, \mathbf{H}_i)$ and scattered fields $(\mathbf{E}_s, \mathbf{H}_s)$. The transmitted fields inside the sphere are denoted as $(\mathbf{E}_t, \mathbf{H}_t)$. The expansion of an incident plane wave propagating in z-direction and linearly polarized in x-direction can be expressed as

$$\begin{aligned} \mathbf{E}_i = e^{ikz}\mathbf{e}_x &= \sum_{n=1}^{\infty} i^n \frac{2n+1}{n(n+1)}(\mathbf{M}_{on}^j - i\mathbf{N}_{en}^j) \\ \mathbf{H}_i = \frac{\kappa}{\mu\omega}e^{ikz}\mathbf{e}_y &= \frac{-\kappa}{\mu\omega}\sum_{n=1}^{\infty} i^n \frac{2n+1}{n(n+1)}(\mathbf{M}_{on}^j + i\mathbf{N}_{en}^j). \end{aligned} \tag{2.23}$$

Here only the Bessel functions which are finite at $r \longrightarrow 0$ need to be taken into account. With the interface conditions of the normal components of the fields $(\mathbf{E}, \mathbf{H})$

$$\begin{aligned} (\mathbf{E}_i + \mathbf{E}_s) \times \mathbf{e}_r &= \mathbf{E}_t \times \mathbf{e}_r \\ (\mathbf{H}_i + \mathbf{H}_s) \times \mathbf{e}_r &= \mathbf{H}_t \times \mathbf{e}_r, \end{aligned} \tag{2.24}$$

it is possible to obtain expressions of the scattered and transmitted fields (only the electric fields are shown here):

$$\begin{aligned}\mathbf{E}_s &= \sum_{n=1}^{\infty} i^n \frac{2n+1}{n(n+1)} \left(i^n a_n \mathbf{N}_{en}^{(3)} - b_n \mathbf{M}_{on}^{(3)}\right) \\ \mathbf{E}_t &= \sum_{n=1}^{\infty} i^n \frac{2n+1}{n(n+1)} \left(c_n \mathbf{M}_{on} - i d_n \mathbf{N}_{en}\right),\end{aligned} \tag{2.25}$$

where the superscript (3) demands the use of the spherical Bessel function of the third kind. The expansion coefficients of the reflected fields (a_n and b_n) and the transmitted fields (c_n and d_n) can be calculated by using the orthogonality of the generating functions:

$$a_n = \frac{m^2 j_n(m\rho)\left(\rho j_n(\rho)\right)' - j_n(\rho)\left(m\rho j_n(m\rho)\right)'}{m^2 j_n(m\rho)\left(\rho h_n(\rho)\right)' - h_n(\rho)\left(m\rho j_n(m\rho)\right)'}, \tag{2.26a}$$

$$b_n = \frac{j_n(m\rho)\left(\rho j_n(\rho)\right)' - j_n(\rho)\left(m\rho j_n(m\rho)\right)'}{j_n(m\rho)\left(\rho h_n(\rho)\right)' - h_n(\rho)\left(m\rho j_n(m\rho)\right)'}, \tag{2.26b}$$

$$c_n = \frac{j_n(\rho)\left(\rho h_n(\rho)\right)' - h_n(\rho)\left(\rho j_n(\rho)\right)'}{j_n(m\rho)\left(\rho h_n(\rho)\right)' - h_n(\rho)\left(m\rho j_n(m\rho)\right)'}, \tag{2.26c}$$

$$d_n = \frac{m j_n(\rho)\left(\rho h_n(\rho)\right)' - m h_n(\rho)\left(\rho j_n(\rho)\right)'}{m^2 j_n(m\rho)\left(\rho h_n(\rho)\right)' - h_n(\rho)\left(m\rho j_n(m\rho)\right)'}, \tag{2.26d}$$

where j_n is the nth spherical Bessel function of the first kind, h_n is the spherical Hankel function of the first kind, $m = \sqrt{\epsilon_r}$ is the relative refractive index of a sphere in vacuum, and ρ is the dimensionless propagation parameter $\rho = kR = \frac{2\pi R}{\lambda}$. Note that the solutions above are only valid where the sphere is considered to be non-magnetic ($\mu_r = 1$).

2.4.2 Mie solution with spectral decomposition

A finite laser pulse consists of a spectral decomposition, the incident pulses are described by frequency decomposition based on the complex electric field in the Fourier domain

$$\mathbf{E}(\mathbf{r}, \omega) = \mathbf{E}_0 f(\omega) e^{i\varphi_{\mathrm{CE}}}, \tag{2.27}$$

where $\mathbf{E}_0$ is the peak amplitude of the laser field, φ_{CE} is the carrier envelope phase, and $f(\omega)$ is the spectral amplitude profile which is considered to have a Gaussian amplitude spectrum

$$f(\omega) = \frac{1}{\sigma_\omega} e^{-\frac{1}{2}\left(\frac{\omega-\omega_0}{\sigma_\omega}\right)^2}, \tag{2.28}$$

where $\sigma_\omega = \frac{2\sqrt{\ln 2}}{\tau}$ is the spectral width, τ is the full-width at half-maximum (FWHM) of the electric field envelope. The spatio-temporal evolution of the electric field is calculated

by the Fourier transform

$$\mathbf{E}(\mathbf{r},t) = \frac{1}{2}\frac{1}{\sqrt{2\pi}}\int_{-\infty}^{\infty}\mathbf{E}(\mathbf{r},\omega)e^{-i\omega t}d\omega + c.c. \tag{2.29}$$

2.4.3 Treatment of tunneling ionization

Tunneling ionization is the dominant contribution to the creation of trajectories in the moderate intensity regime ($10^{13} - 10^{14}\,\mathrm{W/cm^2}$). At each time step ($dt = 0.1\,\mathrm{as}$) a number of randomized points in the sphere‘s surface layer is probed. The ionization probability is determined from ADK atomic tunnel ionization rates (as given by Eq. 2.8) using the field gradient averaged over the tunneling path. The electric field used for the evaluation is the effective field, which contains the time-dependent Mie solution and the instantaneous, self-consistent mean-field.

The tunneling events are sampled via Monte Carlo methods. A successful tunneling event generates a residual ion at the sampling point and a free electron at the end point of the tunneling path, both with zero initial velocity. The classical tunnel exit of the free electron is calculated by a simple geometric approximation of $r_\mathrm{b} = R_\mathrm{sphere} - E_\mathrm{r}/I_\mathrm{p}$, where R_sphere and I_p are the radius and the ionization potential of the nanosphere, respectively.

2.4.4 Treatment of photoionization

The local Wigner distribution $W(r,t,\omega)$ for the XUV pulse inside the sphere is used to describe the instantaneous spectral photoionization rate

$$\Gamma(\omega) = \frac{1}{\hbar\omega}\sigma(\omega)\,W(r,t,\omega)\,. \tag{2.30}$$

The spectral photoionization cross-section

$$\sigma(\omega) = \frac{2k(\omega)\,\omega}{n_\mathrm{mol}c_0} \tag{2.31}$$

is calculated using the extinction coefficient $k(\omega)$ for bulk SiO_2 [48, 118], where n_mol is the atomic density and c_0 is the vacuum speed of light.

2.4.5 Treatment of impact ionization

For trajectories propagating inside the nanoparticle, we account for elastic electron-atom scattering and inelastic electron-electron scattering via effective mean-free paths as described in subsection 2.4.8. During the inelastic scattering process, the impact ionization occurs when a fast moving electron scatters with electrons in the valence band of the nanoparticle and transfer energy to them. A second electron at rest is created when the scattered electron has an energy above the ionization potential. The kinetic energy of the scattered electron is slowed down by an energy I_p. The created electron and residual ion are located at the scattering point (inside the sphere) with both zero initial velocity.

2.4.6 Trajectory propagation

The trajectories of photoelectrons are calculated via integration of the classical equation of motion

$$m\ddot{\mathbf{r}} = -e\left[\vec{\varepsilon}_{\mathrm{NIR}}(\mathbf{r},t) + \vec{\varepsilon}_{\mathrm{mf}}(\mathbf{r},t)\right] \tag{2.32}$$

where m is the effective electron mass which is considered to be m_e in the relevant energy range, $\vec{\varepsilon}_{\mathrm{NIR}}(\mathbf{r},t)$ is the effective near-field and $\vec{\varepsilon}_{\mathrm{mf}}(\mathbf{r},t)$ is the charge interaction induced mean-field. Eq. 2.32 is performed utilizing the Velocity-Verlet algorithm that follows from Taylor expansion. The position vector of a charge around time $t+\Delta t$ can be expressed as

$$\mathbf{r}(t+\Delta t) = \mathbf{r}(t) + \frac{\partial \mathbf{r}}{\partial t}\Delta t + \frac{1}{2}\frac{\partial^2 \mathbf{r}}{\partial t^2}(\Delta t)^2 + \mathrm{O}(\Delta t^3) \tag{2.33}$$

and the momentum vector as

$$\mathbf{p}(t+\Delta t) = \mathbf{p}(t) + \frac{\partial \mathbf{p}}{\partial t}\Delta t + \frac{1}{2}\frac{\partial^2 \mathbf{p}}{\partial t^2}(\Delta t)^2 + \mathrm{O}(\Delta t^3), \tag{2.34}$$

where $\mathbf{p}/m = \partial\mathbf{r}/\partial t$, and $\mathbf{F} = \partial\mathbf{p}/\partial t$. The evolution of momentum vector requires the time-derivative of the force expressed as

$$\frac{\partial \mathbf{F}}{\partial t} = \frac{\mathbf{F}(t+\Delta t) - \mathbf{F}(t)}{\Delta t} + \mathrm{O}(\Delta t). \tag{2.35}$$

In each time step of the simulation, the Velocity-Verlet scheme described above is performed by firstly updating the positions of all charges, secondly calculating the electric fields at these new positions, and lastly updating all momenta of all charges.

2.4.7 Mean-field approximation of charge distributions

When a nanoparticle is exposed to an intense laser field, the ionization processes liberate electrons and create residual ions. The Coulomb interaction of the free charges in the presence of a homogeneous dielectric sphere can be evaluated by multipole expansions. The following derivation is given here as a courtesy of Prof. Thomas Fennel, Universität Rostock.

The potential of a free charge q_i at position $\mathbf{r}_i$ in a medium with relative permittivity ϵ_r is given by Coulomb's law

$$\Phi_i(\mathbf{r}) = \frac{1}{4\pi\epsilon_0\epsilon_r}\frac{q_i}{|\mathbf{r}-\mathbf{r}_i|} = \frac{1}{4\pi\epsilon_0\epsilon_r}\frac{q_i}{|\mathbf{r}_> - \mathbf{r}_<|} \tag{2.36}$$

Here, $r_>$ is the larger value of the two absolute values $|\mathbf{r}|$ and $|\mathbf{r}_i|$, while $r_<$ is the smaller value. At all positions $\mathbf{r} \neq \mathbf{r}_i$, the Laplace equation must be fulfilled:

$$\triangle\Phi_i(\mathbf{r}) = 0 \quad \forall \mathbf{r} \neq \mathbf{r}_i \tag{2.37}$$

In spherical coordinates this yields [115]:

$$\frac{1}{r}\frac{\partial}{\partial r}(r\Phi) + \frac{1}{r^2\sin(\theta)}\frac{\partial}{\partial\theta}\Big(\sin(\theta)\frac{\partial\Phi}{\partial\theta}\Big) + \frac{1}{\sin^2(\theta)}\frac{\partial^2\Phi}{\partial\phi^2} = 0 \tag{2.38}$$

After a separation of variables the solution can be written as a product of functions of the spherical coordinates:

$$\Phi = \sum_{l=0}^{\infty}\sum_{m=-\infty}^{\infty}\frac{U_l(r)}{r}P_l(\cos\theta)Q_m(\phi) \tag{2.39}$$

with

$$U_l(r) = A_l r^{l+1} + B_l r^{-l} \tag{2.40a}$$

$$Q_m(\phi) = C_m e^{im\phi} \tag{2.40b}$$

$$P_l(x) = \frac{1}{2^l l!}\frac{\partial^l}{\partial x^l}(x^2-1)^2 \tag{2.40c}$$

$P_l(x)$ are the well-known Legendre polynomials. The coefficients A_l, B_l and C_m have to be determined from the boundary conditions. For finding these coefficients for a single charge at $\mathbf{r}_i$, a trick can be used by rotating the coordinate system such the z-axis aligns with $\mathbf{r}_i$. Now the problem has cylindrical symmetry around this axis, which implicates the problem does no more depend on ϕ ($C_0 = 1, C_m = 0 \quad \forall m \neq 0$). This yields

$$\Phi_i(\mathbf{r}) = \sum_{l=0}^{\infty}[A_l r^l + B_l r^{-(l+1)}]P_l(\cos(\theta)) \tag{2.41}$$

A Taylor expansion of (2.36) around $r_< = 0$ and a comparison of coefficients yields expressions for the A_l and B_l resulting in

$$\Phi_i(\mathbf{r}) = \frac{q_i}{4\pi\epsilon_0\epsilon_r}\sum_{l=0}^{\infty}\frac{r_<^l}{r_>^{l+1}}P_l(\cos(\theta_{\mathbf{r}\mathbf{r}_i})), \tag{2.42}$$

where $\theta_{\mathbf{r}\mathbf{r}_i}$ is the angle between $\mathbf{r}$ and $\mathbf{r}_i$. Equation (2.42) is equivalent to (2.36). The potential of multiple charges can be obtained by simply superimposing the individual contributions.

We will now assume a sphere with a relative permittivity ϵ_r and a radius R to be placed at $\mathbf{r} = \mathbf{0}$. Both solutions for the potential outside Φ_i^{out} and inside of the sphere Φ_i^{in} have to obey the boundary conditions at the surface. At first, one has to distinguish whether a charge is placed inside the sphere or outside. As the solution has to be finite, this leads to an ansatz for the case $r_i < R$:

$$\Phi_i^{\text{in}}(\mathbf{r}) = \frac{q_i}{4\pi\epsilon_0\epsilon_r}\sum_l\frac{r_<^l}{r_>^{l+1}}P_l(\cos\theta_{\mathbf{r}\mathbf{r}_i}) + \sum_l A_l r^l P_l(\cos\theta_{\mathbf{r}\mathbf{r}_i}) \qquad r < R \tag{2.43a}$$

$$\Phi_i^{\text{out}}(\mathbf{r}) = \sum_l B_l r^{-(l+1)}P_l(\cos\theta_{\mathbf{r}\mathbf{r}_i}) \qquad r > R \tag{2.43b}$$

while for $r_i > R$

$$\Phi_i^{\text{in}}(\mathbf{r}) = \sum_l C_l r^l P_l(\cos\theta_{\mathbf{r}\mathbf{r}_i}) \qquad r < R \tag{2.44a}$$

$$\Phi_i^{\text{out}}(\mathbf{r}) = \frac{q_i}{4\pi\epsilon_0}\sum_l \frac{r_<^l}{r_>^{l+1}} P_l(\cos\theta_{\mathbf{r}\mathbf{r}_i}) + \sum_l D_l r^{-(l+1)} P_l(\cos\theta_{\mathbf{r}\mathbf{r}_i}) \qquad r > R \tag{2.44b}$$

The boundary conditions at the sphere surface demand for a continuity of the potential itself and the normal component of the dielectric displacement $\mathbf{D}$ [115]:

$$\Phi^{\text{in}}(\mathbf{R}) = \Phi^{\text{out}}(\mathbf{R}) \tag{2.45a}$$

$$\mathbf{D}_\perp^{\text{in}}(\mathbf{R}) = \epsilon_r \frac{\partial \Phi^{\text{in}}}{\partial r}(\mathbf{R}) = \epsilon_r \frac{\partial \Phi^{\text{out}}}{\partial r}(\mathbf{R}) = \mathbf{D}_\perp^{\text{out}}(\mathbf{R}) \tag{2.45b}$$

Inserting equations (2.43) and (2.44) into these boundary conditions again gives solutions for the coefficients A_l, B_l, C_l and D_l. The final solution for a all charges i inside the sphere reads

$$\Phi^{\text{in}}(\mathbf{r}) = \frac{1}{4\pi\epsilon_0\epsilon_r}\sum_l \left[\sum_{\substack{r_i<R \\ r_i<r}} \frac{q_i r_i^l}{r^{l+1}} P_l(\alpha_i) + \sum_{\substack{r_i<R \\ r_i>r}} \frac{q_i r^l}{r_i^{l+1}} P_l(\alpha_i) + \sum_{r_i<R} a_l r^l q_i r_i^l P_l(\alpha_i) \right] \tag{2.46a}$$

$$\Phi^{\text{out}}(\mathbf{r}) = \frac{1}{4\pi\epsilon_0}\left[\sum_l \sum_{r_i<R} b_l \frac{q_i r_i^l}{r^{r+1}} P_l(\alpha_i) \right] \tag{2.46b}$$

while for charges outside the sphere

$$\Phi^{\text{in}}(\mathbf{r}) = \frac{1}{4\pi\epsilon_0}\left[\sum_l \sum_{r_i<R} q_i \frac{c_l r^l}{r_i^{r+1}} P_l(\alpha_i) \right] \tag{2.47a}$$

$$\Phi^{\text{out}}(\mathbf{r}) = \frac{1}{4\pi\epsilon_0\epsilon_r}\sum_l \left[\sum_{\substack{r_i>R \\ r_i<r}} \frac{q_i r_i^l}{r^{l+1}} P_l(\alpha_i) + \sum_{\substack{r_i>R \\ r_i>r}} \frac{q_i r^l}{r_i^{l+1}} P_l(\alpha_i) + \sum_{r_i>R} q_i \frac{d_l q_i}{r_i^{l+1} r^{l+1}} P_l(\alpha_i) \right] \tag{2.47b}$$

The coefficients a_l, b_l, c_l and d_l can again be determined from the boundary conditions.

To calculate the potential at an arbitrary position in free space, one has to evaluate the potentials at the positions of all charges, which results in an unfeasible numerical effort. Instead of the direct evaluation of potentials, a strategy for a more efficient numerical implementation based on lookup tables (LUTs) was introduced by Prof. Thomas Fennel. More technical details are outlined in [113].

2.4.8 Elastic and inelastic scattering

Elastic and inelastic collisions are treated as instantaneous scattering events and are described by energy-dependent cross sections. To describe elastic scattering, we used an

atomic all-electron LDA code to calculate the atomic potentials of Si and O and determined the respective atomic differential elastic-scattering cross sections (DCS), $\frac{d\sigma_{el}}{d\Omega}(E_{\text{ekin}}, \theta)$, by quantum scattering calculations using partial wave analysis. Here E is the asymptotic electron kinetic energy and θ is the scattering angle. The effective atomic DCS follows from weighting the DCSs for Si and O with the respective stoichiometric factors for silica. From the resulting effective DCS we calculate the transport cross section

$$\sigma_{\text{el,tr}}(E_{\text{ekin}}) = \int (1 - \cos\theta) \frac{d\sigma_{\text{el,eff}}}{d\Omega}(E_{\text{ekin}}, \theta)\, d\Omega. \tag{2.48}$$

Note that this quantity specifies the total scattering cross section of a hypothetical isotropic scatterer that induces the same average electron-atom momentum transfer per collision as the scatterer characterized by the full DCS. The transport cross section is typically much smaller than the total scattering cross section resulting from the DCS because many individual small angle physical collisions are described by a few effective collisions with large scattering angles. Because of lower resulting collision rates, the elastic scattering is implemented in our model as isotropic scattering which simplifies the numerical treatment in the trajectory propagation substantially.

The cross section for the inelastic collisions is calculated using a simplified Lotz formula [66]

$$\sigma_{\text{inel}}(E_{\text{ekin}}) = 450\text{Å}^2\text{eV}^2 s \frac{\log(E_{\text{ekin}}/I_{\text{p}})}{E_{\text{ekin}} I_{\text{p}}} \tag{2.49}$$

with an ionization potential of $I_{\text{p}} = 9\,\text{eV}$ and the global scaling parameter s, which is varied to match the experimental data. Here, the best agreement is found for $s = 2.1$. The inelastic scattering cross section only includes impact ionization in our model and ignores electron phonon scattering, which is negligible in the relevant energy range.

The above cross sections are connected to elastic and inelastic mean-free paths via

$$L_{\text{emfp}}(E_{\text{ekin}}) = \frac{1}{n_{\text{mol}} \sigma_{\text{el,tr}}(E_{\text{ekin}})} \tag{2.50}$$

and

$$L_{\text{imfp}}(E_{\text{ekin}}) = \frac{1}{n_{\text{mol}} \sigma_{\text{inel}}(E_{\text{ekin}})} \tag{2.51}$$

where n_{mol} is the molecular number density (we used $n_{\text{mol}} = 0.022\text{Å}^{-3}$). Finally, the mean free paths can be expressed as scattering times via

$$\tau_{\text{el/inel(E}_{\text{ekin}})} = \frac{L_{\text{emfp/imfp}}(E_{\text{ekin}})}{v(E_{\text{ekin}})} \tag{2.52}$$

with $v(E) = \sqrt{2E/m_e}$ for the electron velocity and m_e as the electron rest mass. For silica, effective mass effects are negligible in the considered energy range and have therefore been ignored [119].

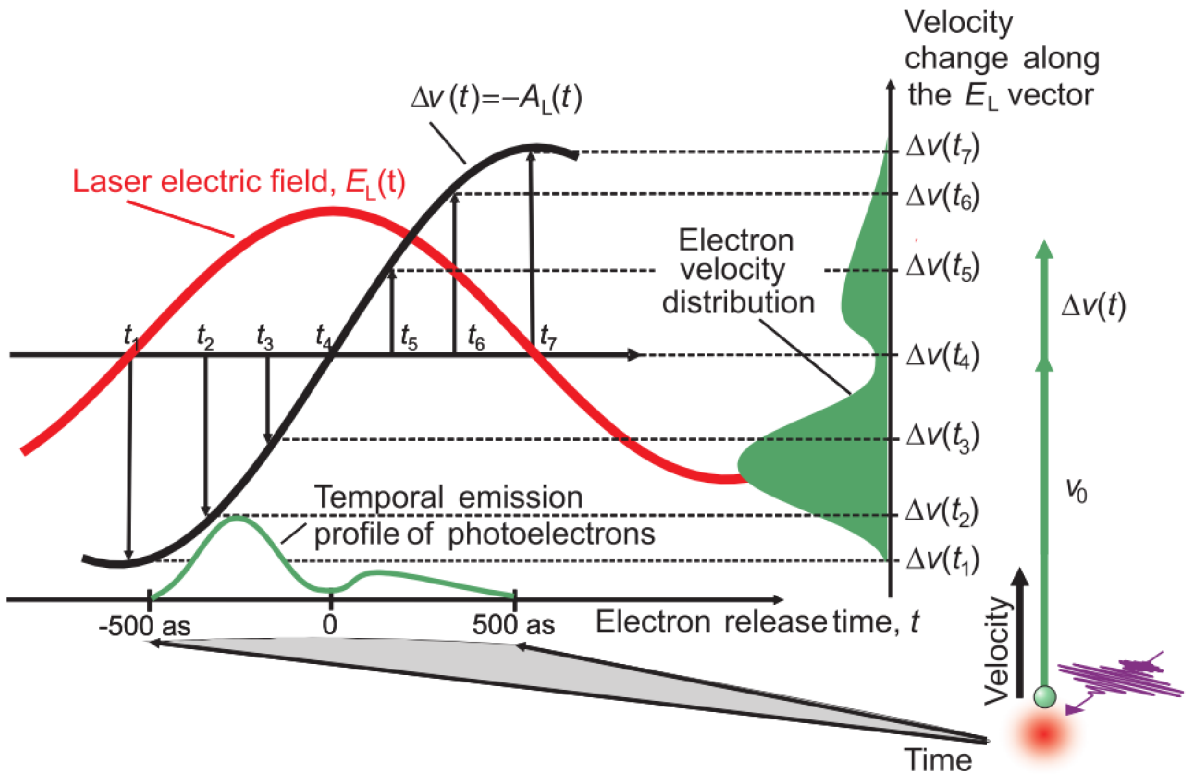

Figure 2.6: Concept of optical-field-driven attosecond streaking. Photoelectrons released in presence of a laser field experience a change of their initial velocities parallel to the direction of electric field (red line) that is proportional to the vector potential of the field (black line) at the instant of release. This function is monotonic within a half wave cycle of the field, mapping the temporal profile of a sub-fs XUV pulse into a corresponding final velocity (or energy) distribution of photoelectrons. Taken from [28].

2.5 Attosecond streaking metrology

The time-resolved measurements with attosecond resolution had been successfully performed by using an isolated attosecond XUV pulse (pump) to ionize the system and a delayed femtosecond IR pulse (probe) to detect the dynamics [28]. In the absence of resonances and a moderate probe pulse, the temporal profile of photoemission rate follows the intensity profile of the XUV pump pulse as shown in figure 2.6. The initial kinetic energy of the released fast photoelectron is assumed to be

$$E_{\mathrm{kin}} = \frac{1}{2} m_{\mathrm{e}} v_0^2 = \hbar\omega_{\mathrm{XUV}} - I_{\mathrm{p}} \geq I_{\mathrm{p}}, \tag{2.53}$$

where ω_{XUV} is the wavelength of the incident XUV pulse, and I_{p} is the ionization potential of the medium. According to Newton's classical law of motion, the final velocity v_{f} of a

photoelectron emitted at time t_e under the approximations: 1) the photoemission process is assumed to happen instantaneously, 2) the photoemitted electron quickly leaves the atom thus the effect of the Coulomb potential of the parent ion is neglectable, can be determined as follows:

$$v_f(t_e) = v_0 - \int_{t_e}^{\infty} \frac{e}{m_e} E(t)dt = v_0 - \frac{e}{m_e} A(t_e), \tag{2.54}$$

where $A(t)$ is the vector potential of the electric field defined as $E(t) = -\frac{\partial}{\partial t}A(t)$ in the Coulomb gauge. The final kinetic energy is obtained by

$$E_{kin}(t_e) = \frac{1}{2} m_e v_0^2 - e v_0 A(t_e) + \frac{e^2}{2m_e} A^2(t_e). \tag{2.55}$$

The quadratic term $A^2(t_e)$ can be neglected in the case of moderate laser fields. From Eq. 2.53 and Eq. 2.55, one obtains the change in the electron's kinetic energy

$$\Delta E_{kin}(t_e) \approx -e v_0 A(t_e) = -eA(t_e)\sqrt{\frac{2}{m_e}(\hbar\omega_{XUV} - I_p)}. \tag{2.56}$$

Within any half cycle between negative and positive maxima of the IR laser field, the vector potential $A(t)$ is a monotonic function of time (see figure 2.6). As a consequence, the temporal distribution of the emitted electron wave packet is mapped onto a corresponding final kinetic energy distribution of photoelectrons. The streaking spectrogram can be obtained by plotting the photoelectron spectra as a function of delay time t_e between pump and probe pulses. The resultant streaking spectrogram provides direct time-domain information on the electron wave packet's emission and propagation. The time resolution is only limited by the attosecond XUV pulse length, and the experimental stability in a practical measurement.

Chapter 3

Experimental techniques

3.1 Nanoparticle samples

3.1.1 Sample preparation and characterization

SiO_2 nanoparticle samples were obtained by wet chemical synthesis. First, small seed nanoparticles were prepared by the Stöber method [120]. Then they were grown by the seeded growth methods until the desired particle size was reached. The typical nanoparticle diameter is in the range from few tens of nanometers to few hundreds nanometer. All nanoparticles were dispersed in ultrapure ethanol ($> 99.99\%$), and characterised by transmission electron microscopy (TEM). Figure 3.1 shows the TEM images of the nanoparticle with different average diameters. The surfaces of the spheres are smooth. The polydispersity of the particles is about 8 %. The SiO_2 samples were produced by the groups of Prof. Eckart Ruhl and Prof. Markus Gallei (TU Darmstadt).

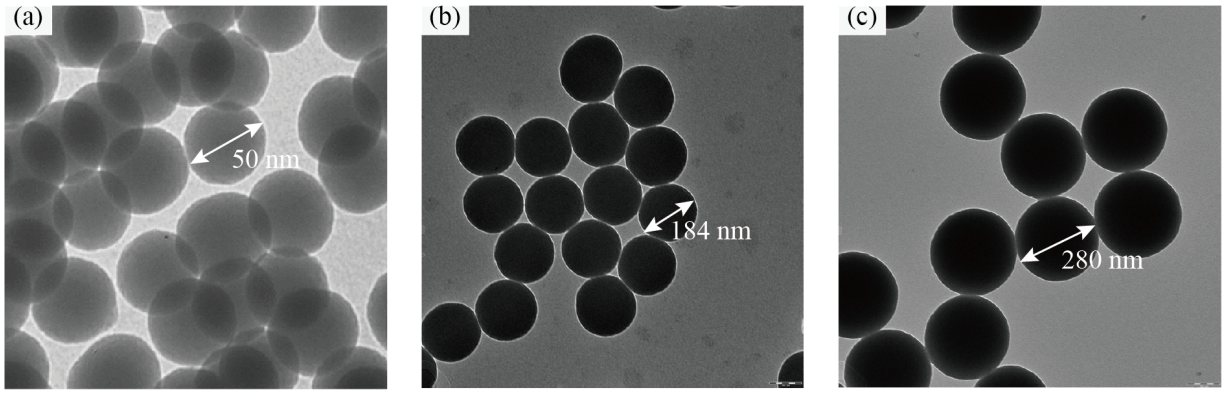

Figure 3.1: Transmission electron micrograph (TEM) of SiO_2 particles with an average diameter of (a) 50 nm, (b) 184 nm and (c) 280 nm.

3.2 Aerosol generation

For generation and delivery of a narrow beam of isolated nanoparticles in the ultra-high vacuum ($< 1 \times 10^{-7}$ mbar). The approach of aerosol generation and aerodynamic lens focusing were employed to deliver tightly collimated particle beams to the analyzing region, such as mass spectrometer, cluster spectroscopy and material synthesis [121].

The aerosol generation system consisted of an evaporator, silica drying stage, impactor, pressure equalizer (Fig. 3.2), and the aerodynamic lens (Fig. 3.3). The aerosol is evaporated from a nanoparticle suspension by a commercial aerosol generator (model 3076, TSI). The typical evaporation pressure of the carrier gas (neon or nitrogen) is 1.75 bar. The nanoparticle density in the aerosol is determined by the nanoparticle concentration in the suspension and the evaporation gas pressure. The wet aerosol is sent through the diffusion dryer (model 3062, TSI) to remove residual solvent from the aerosol. The impactor consists of a sharp 90° turn, and blocks nanoparticle clusters. A capsule filter (HEPA 1602051, TSI) is installed in front of the aerodynamic lens system to level the input pressure to one atmosphere. The exhausted nanoparticles are trapped in the capsule filter.

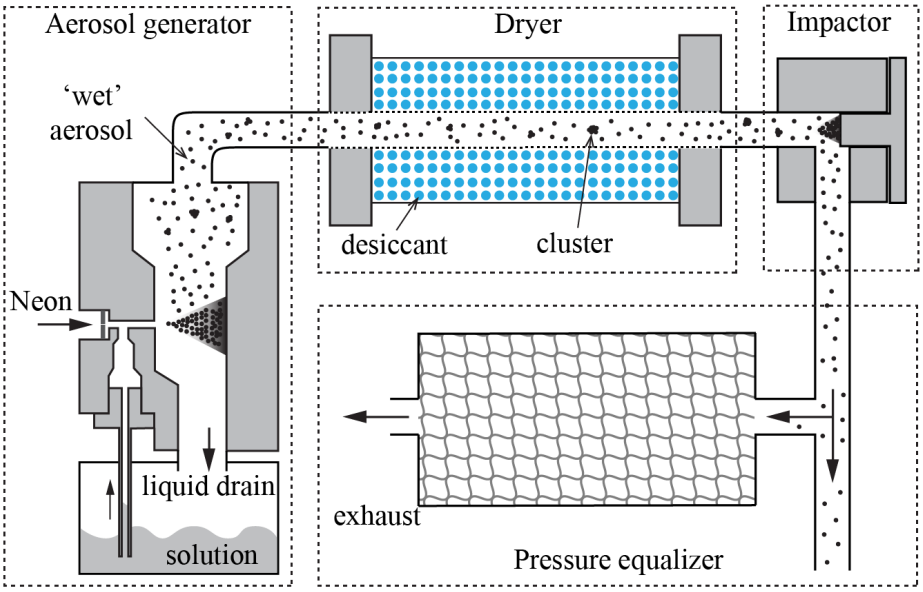

Figure 3.2: Schematic diagram of aerosol generation system. The system consisted of an evaporator, silica drying stage, impactor and pressure equalizer. Taken from [114]

Figure 3.3 shows the cross-section drawing of an aerodynamic lens system, it consists of three parts: a flow control orifice, a series of focusing lenses, an acceleration nozzle with subsequent differential pumping. The initial orifice determines the gas flow through the lens system and reduces pressure from atmosphere to the value required for aerodynamic

focusing. In the current setup, the diameter of the orifice is 130 μm. The inner diameter of the lens is 10 mm. The gas flow is converged and diverged through the focusing lenses which include five apertures. The aperture sizes and distances are labeled in Fig. 3.3. Three stages of differential pumping behind the lens system maintain the pressure in the experimental chamber below 2×10^{-7} mbar with operating nanoparticle source. The inner diameters of the nozzles are 2 mm.

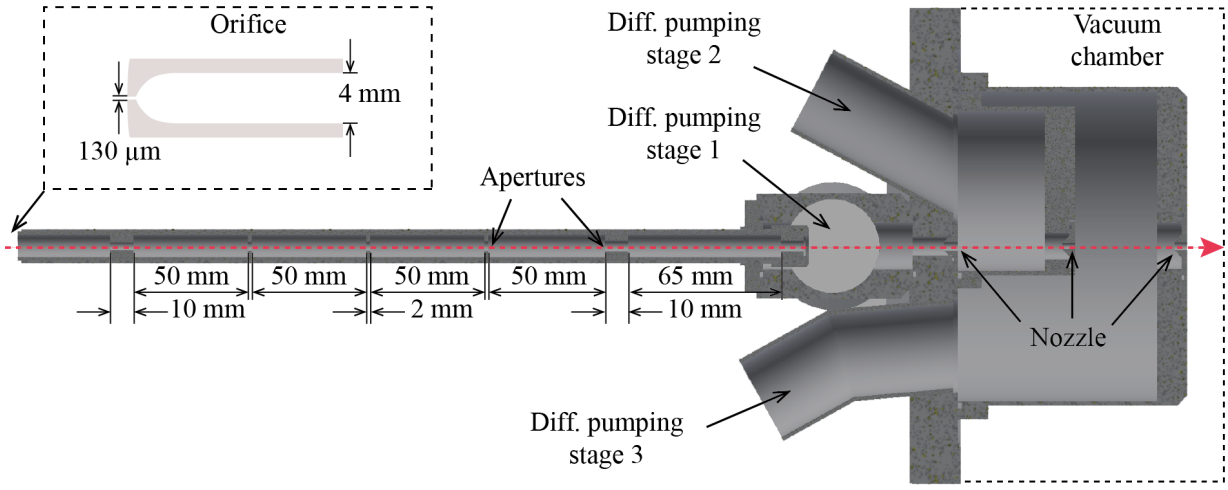

Figure 3.3: The cross-section drawing of an aerodynamic lens system, consisting of three parts: a flow control orifice (inset), a series of focusing lenses, an acceleration nozzle with subsequent three differential pumping stages. The red dashed line indicates the flow direction of the aerosols from the orifice (left) into the vacuum chamber (right). The aperture sizes and distances are labeled, and inner diameters of the nozzles are 2 mm.

With given particle size and gas flow properties, the nanoparticles can efficiently be separated from the carrier gas due to their inertia. The nanoparticles are focused into a tight particle beam (diameter around 500 μm) after the acceleration nozzle, while the carrier gas is efficiently removed after some distance from the last aperture of the aerodynamic lens.

The nanoparticle density in the interaction region is limited by multiple factors: i) the nanoparticle density in the dispersion, ii) the aerosol generation step where evaporation conditions have to be met to avoid cluster formation, iii) the aerosol transport system including liquid reflow, drying stage(s), and pressure equalization, iv) impactor(s) to reduce the amount of clusters in the beam, v) restrictions of the aerodynamic lens system, including aperture sizes and nanoparticle-size dependent throughput, and finally vi) the distance from the last aperture to the interaction region. The use of nanoparticle dispersions with small size distributions (below 10 %) makes it unnecessary to use differential mobility analysis, increasing the nanoparticle density in the interaction region.

3.3 Single-shot velocity map imaging

3.3.1 Eppink-Parker VMI spectrometer

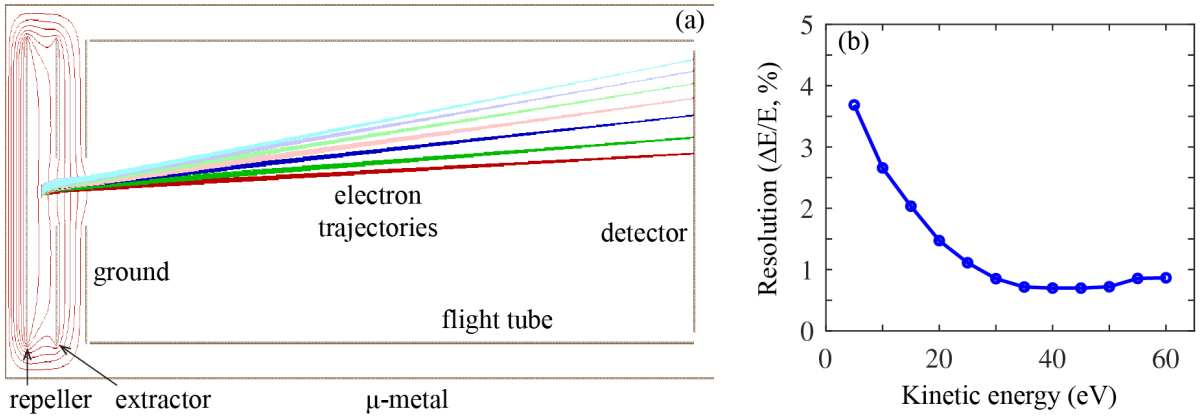

Figure 3.4: (a) The numerical calculations of the photoelectron trajectories and equipotential lines with SIMION8 for Eppink-Parker VMI spectrometer. The red solid lines indicate the equipotential lines. Electron trajectories ($E_{\mathrm{kin}} = 5, 10 - 100\,\mathrm{eV}$) are released in the middle of the repeller and the extractor electrodes in x-direction, and along a line ($z = 0 \pm 0.5\,\mathrm{mm}$) parallels to the electrodes. (b) Energy resolution as function of the kinetic energy of the detected electrons.

The technique of Velocity Map Imaging (VMI) is a direct method for measuring angle- and energy-resolved ion or electron velocity distributions from photoionization or fragmentation. This technique was first introduced by Chandler and Houston [122], and revolutionarily improved by Eppink and Parker [123], who incorporated an ion optics lens design by replacing the grid with an open electrode. The Eppink-Parker design is widely used to detect a two-dimensional projection of the full particle momentum distribution in strong field atomic and molecular physics [48, 66, 67, 75, 124–126].

A VMI spectrometer typically consists of a 2D detector, μ -metal shell and electrostatic lens system, as shown in Fig. 3.4(a). In this work, we employed the classical Eppink-Parker VMI spectrometer [123]. The 2D detector consisted of a pair of microchannel plates (MCPs) followed by a phosphor screen (Hamamatsu F2226-24PX). The supply voltages of the detector are gated by a fast high-voltage switch with a gate width of 300 ns (HTS-41-03 GSM, Behlke) to reduce background contributions. The images on the phosphor screen are recorded by a camera and transferred to a computer for post-processing. The μ-metal shell covers the whole spectrometer to block the stray magnetic field. The electrostatic lens system contains a repeller, an extractor, a ground electrode and a flight tube. The positions and geometries of these electrodes, and the applied voltages are properly tuned via numerical simulation (SIMION8), such that the ions/electrons with the same projection

of the initial velocity will be mapped onto the same position on the 2D detector. The interaction region is located in the center of the repeller and the extractor electrodes. The Eppink-Parker design allows for very high-resolution measurements down to 1 %, in agreement with laboratory experience. This is due the long flight distance (327.5 mm from the interaction region to the detector) and high voltage on the repeller electrode (−10 kV). In the experimental measurements, the resolution of a well-designed VMI is influenced by the size of the interaction volume, the stability of the high-voltage power supply and the detector system. All these features have to be checked carefully before a real measurement.

3.3.2 Energy calibration

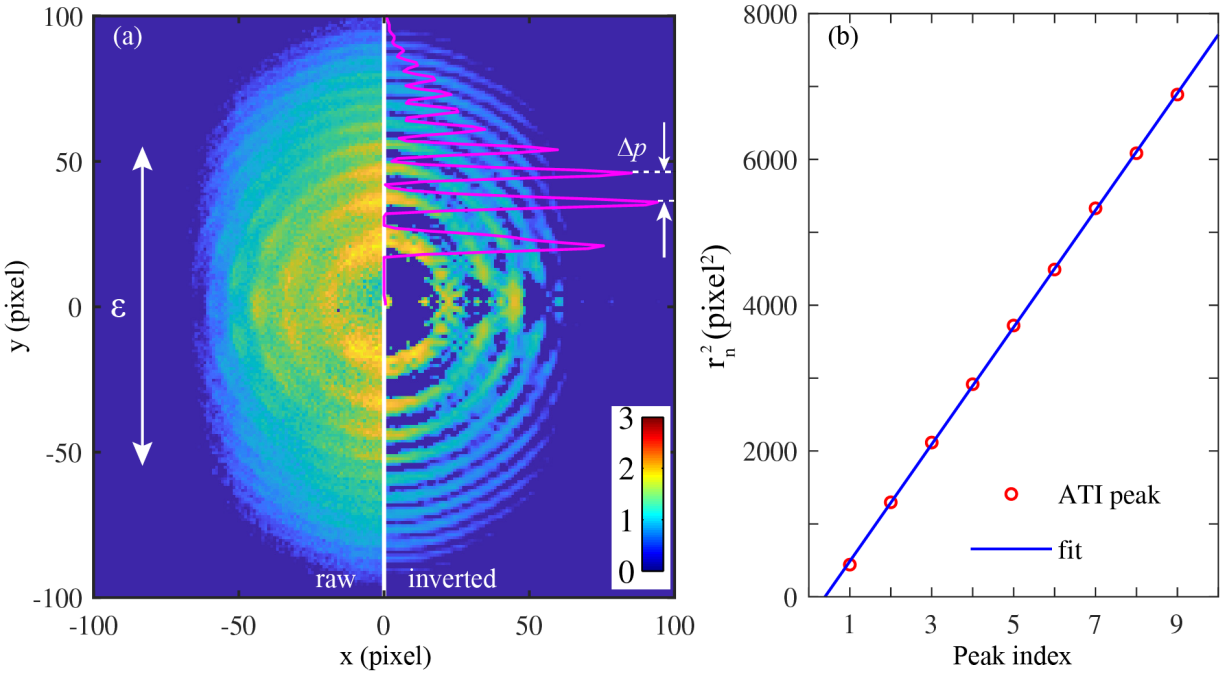

Figure 3.5: Raw (left side) and inverted (right side) photoelectron images (log color scale) recorded with xenon with 25 fs linear polarized NIR pulses at an intensity of $(5 \pm 0.5) \times 10^{13}$ W/cm^2. Laser polarization direction is along the y-axis. The red solid line shows the photoelectron spectrum calculated from the inverted image. (b) Linear fitting (blue line) of the square of the radius of the ATI peaks (red circles) yields the scaling factor of the VMI.

The VMI technique records a two-dimensional (2D) image, where the three-dimensional momenta were projected along the spectrometer axis. If the distribution of charged particles is cylindrically symmetric and its symmetry axis lines in the detector plane, the full three-dimensional (3D) information of the charged particle distribution can be extracted

via Abel-inversion. Figure 3.5(a) shows a typical raw image (left side) obtained from above-threshold-ionization (ATI) of xenon atoms with a near-infrared (NIR) laser pulse, and the inverted image (right side) with the BASEX transformation [127]. The laser intensity was $(5 \pm 0.5) \times 10^{13}\,\mathrm{W/cm^2}$ and the central wavelength was 790 nm. The laser polarization direction was along the y-axis. The specific angular dependent ATI structure in the photoelectron signal is well characterized after the inversion [128]. The ATI peaks can be obtained by angular integration, as shown with the red solid line in Fig. 3.5(a). The spectral spacing between consecutive peaks δE_{kin} equals the photon energy ($\hbar\omega_L = 1.57\,\mathrm{eV}$) of the incident laser pulse.

In order to obtain energy calibration, two different methods can be employed: i) retrieving from the numerical simulations with the exact spectrometer geometry and corresponding parameters; ii) fitting the energy expression to experimental data with well-established photoemission features, e.g. the ATI electron emission from noble gas atoms. As the radius of a pixel with respect to the center is proportional to its initial momentum components in the detector plane, the corresponding electron energy is given by the expression $E_{\mathrm{kin}} = |q|\,V_{\mathrm{rep}} r^2/k^2$, where q is the charge of the particle, V_{rep} is the potential on the repeller, r is the radius in pixel, and k is the calibration coefficient. The calibration coefficient is determined by the spectrometer geometry and was obtained from ATI electron emission from Xe atoms (Fig. 3.5(b)).

With $\Delta E_{\mathrm{kin}} = |q|\,V_{\mathrm{rep}}(r^2_{\mathrm{n+1}} - r^2_{\mathrm{n}})/k^2 = 1.57eV$, the scaling factor $s = |q|\,V_{\mathrm{rep}}/k^2$ can be obtained by fitting the square of the radius of the consecutive ATI peaks to a linear function, as shown in Fig. 3.5(b). In the current configuration, the scaling factor between energy and pixel radius is $s = 1.96 \times 10^{-3}\,\mathrm{eV/pixel^2}$.

3.3.3 Single-shot image acquisition

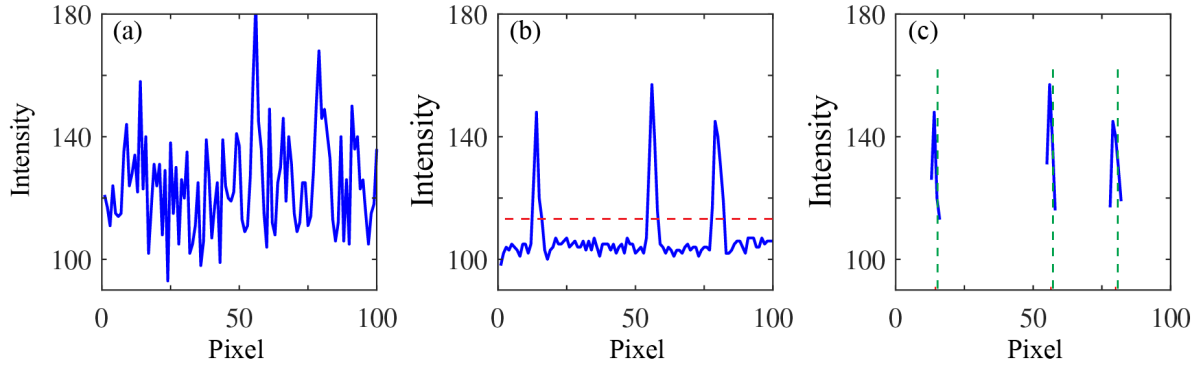

Figure 3.6: Single CMOS line signal (a) before and (b) after the flat-field correction algorithm. The red dashed line corresponds to the intensity threshold set in the thresholding algorithm in the image acquisition software. (c) Signal above threshold. The green dashed lines indicate the center of intensity of isolated events. Adapted from [129].

The images on the phosphor screen were recorded by a high-speed digital complementary metal-oxide-semiconductor (CMOS) camera (GS-Vitec Marathon Ultra). The camera was operated at the laser repetition rate (1 kHz) with a resolution of 800×600 pixels. A real time image post-processing was implemented in the camera software (GS-Vitec Marathon Pro) to reduce the background and most importantly to save the single-shot images separately [129]. Briefly, a flat-field correction algorithm is introduced to the raw CMOS line signal (cf. Fig. 3.6(a)) to correct the inhomogeneous response of the sensor by recording a reference image. Figure 3.6(b) shows the CMOS line signal after the flat-field correction. The signal-to-noise ratio is drastically enhanced. With a properly chosen intensity threshold (red dashed line), only three electron events are valid and stored for later analysis (see Fig. 3.6(c)).

3.3.4 Image centroiding

By employing the flat-field correction and the threshold selection algorithm in the image acquisition software during the measurement, many images consisting the valid pixels that correspond to ions/electrons from a single laser shot are stored. Single-shot imaging provides us the flexibility to trace the photoemission process on the level of a single charge. Image centroiding algorithm reveals the distribution of the charged particle from the pixel blocks of the recorded images, which offer us the probability to count the total number of electrons that were ionized and tag the images by the asymmetrical distribution of the emitted electrons [129].

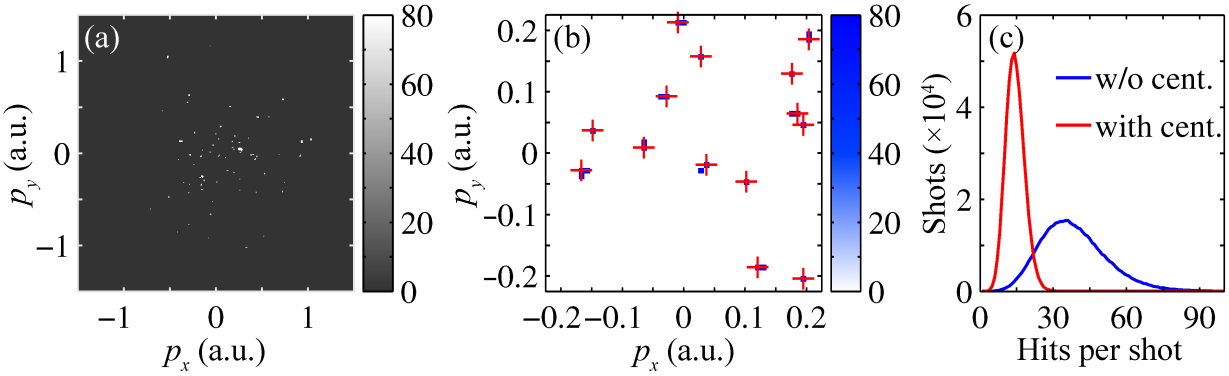

Figure 3.7: (a) A typical raw image obtained from above-threshold ionization (ATI) of Nitrogen gas with a single laser pulse. The laser intensity was 3×10^{13} W/cm^2 and polarized along the y-axis. (b) The center of gravity (red crosses) of individual groups of pixels (false color). (c) The histogram of the hits per shot with (red line) and without (blue line) the centroiding algorithm.

The number of electrons that were recorded in the single-shot images can be obtained under the condition that no hits overlap directly in the single-shot images. Figure 3.7(a)

shows a typical raw image obtained from ATI of nitrogen gas with a single laser pulse. The raw image consisted of few tens of individual spots, where each spot corresponds to a single electron hitting the MCP detector. The spots are combined by groups of pixels due to the magnification setting of the imaging lens (Fig. 3.7(b)). A single electron event can produce several pixels of the CMOS chip. In order to increase the resolution of the VMI measurement, we employed a centroiding algorithm to each individual spots. Using the brightness of pixels located in the same spot, the centroiding algorithm calculates the center of gravity indicated as red crosses in Fig. 3.7(b). Figure 3.7(c) shows the histograms of the hits per shot with and without centroiding algorithm. The histograms were obtained from 5×10^5 images which were acquired in 8.3 minutes at 1 kHz repetition rate. The distribution is narrower, and peaks at low event numbers in case of the images processed with the centroiding algorithm.

3.4 Generation of ultrashort laser pulses

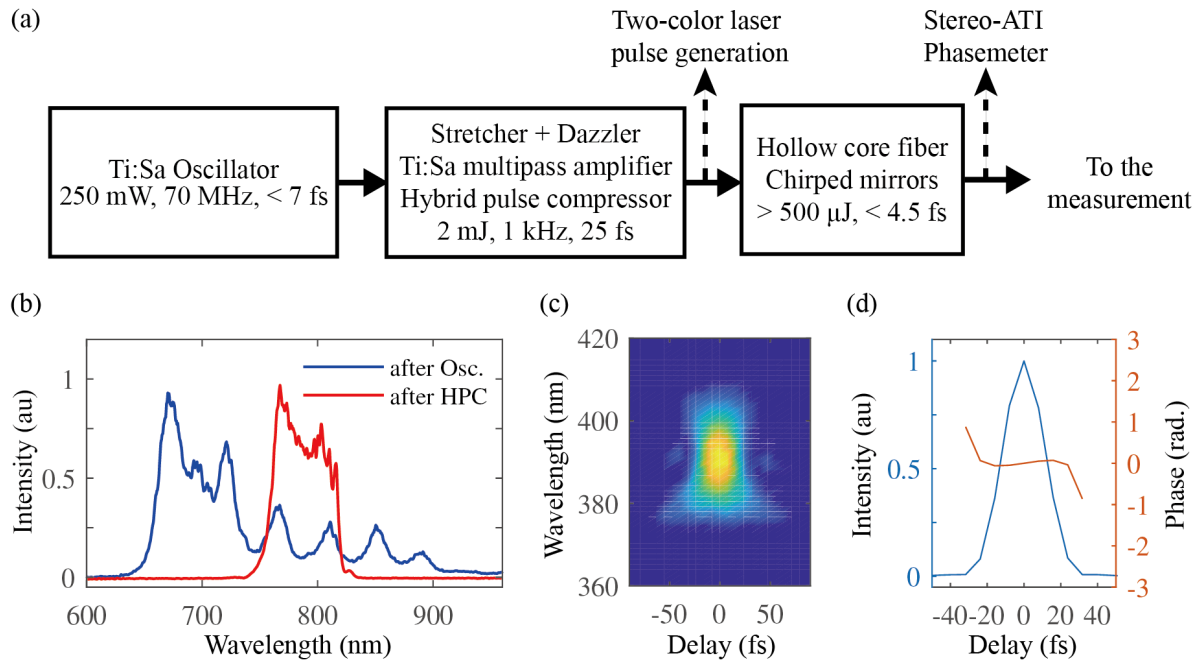

Figure 3.8: (a) Overview of the laser system. (b) Spectra of the laser pulses after the Ti:Sapphire oscillator (blue) and after the hybrid pulse compressor (red). (c) Retrieved FROG trace (c) and phase (d) of the compressed pulse after the HPC.

The generation and characterization of intense, ultrashort laser pulses are routine experimental techniques which require a variety of complex optical and electronic equipment.

In this work, we employed near-infrared (NIR) laser fields with the pulse durations ranging from 30 fs down to 4.5 fs.

The key components of the laser system are outlined in Fig. 3.8(a). The seed pulses are generated by an ultra-broadband Ti:Sapphire oscillator (Rainbow: Femtolasers GmbH). The pulse energy is 3.5 nJ at repetition rate of 70 MHz. The oscillator spectrum extends from 620 nm to 1000 nm as shown with blue line in Fig. 3.8(b), corresponding to a pulse duration shorter than 7 fs. The seed pulse is stretched to a pulse duration of approximately 10 ps by a glass stretcher (SF-57). Before entering the amplifier, the stretched pulse passes an Acousto-Optic Programmable Dispersive Filter (AOPDF, Fastlite DAZZLER) for dispersion control. The pulse energy reaches 2 mJ after 10 amplification passes through the Ti:Sapphire amplifier (Femtopower Compact-Pro, Femtolasers GmbH). The Ti:Sapphire crystal is pumped by green light (532 nm) at a repetition rate of 1 kHz (DM30, Photonics Industries). The compression of the amplified pulse to its Fourier limit is achieved by hybrid pulse compressor (HPC) which consists of a double-prism pulse compressor and a set of 16 high dispersive mirrors (HDMs). The laser pulse energy at this stage exceeds 1.4 mJ with a spectral bandwidth of approximately 60 nm centered at a wavelength of 790 nm as shown with red line in Fig. 3.8(b). The pulse duration is 26 fs as characterized by frequency-resolved optical gating (FROG, Swamp Optics). The traces and the results of the pulse- and phase retrieval are shown in Fig. 3.8(c) and (d), respectively.

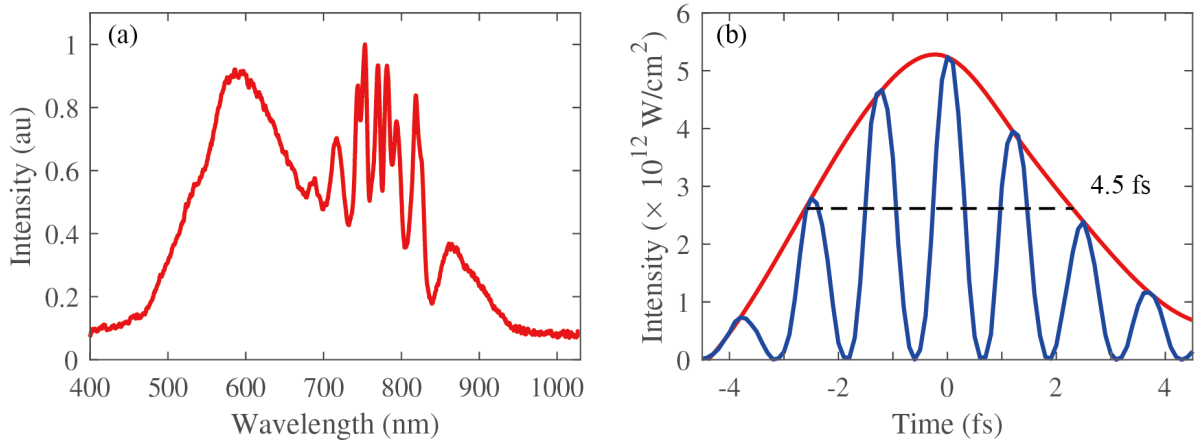

Figure 3.9: (a) Laser spectrum after the HCF. (b) Intensity profile after the chirp mirrors obtained by attosecond streaking spectroscopy. Adapted from [130].

The laser beam after the hybrid pulse compressor was either delivered into a collinear two-color setup described in section 3.5, or focused into a hollow core fiber (HCF) for spectral broadening. The inner diameter of the HCF is 275 μm with a length of 1 m. The HCF is mounted in a tube filled with Ne gas at a pressure $p \approx 3$ bar. The tube is equipped with Brewster entrance and exit windows (thickness 1 mm) to reduce reflection losses. A beam stabilization system (Aligna, TEM) ensures a constant focus position of

the beam on the fibre entrance. The focused laser pulse is broadened via optical Kerr effect [131]. The laser spectrum behind the HCF extends over a full octave from slightly below 500 nm up to 1000 nm as shown in Fig. 3.9(a). The spectrum extends more to the blue side with respect to the central wavelength (720 nm) because the focused laser pulse experiences self-steepening in the fibre [132]. Broadband negatively chirped mirrors provide an efficient compression of pulses with a spectrum exceeding one actave [133]. In the beamline, the positive dispersion was compensated with 6 pairs of chirped mirrors. Fine tuning of the laser pulse duration was achieved with a set of motorized glass wedges. The NIR laser pulses could be compressed to 4.5 fs as characterized by an attosecond streaking measurement as shown in Fig. 3.9(b). A portion of the beam (20%) was split into the Stero-ATI phasemeter setup to record the carrier-envelope phase of the few cycle laser pulse [84].

3.5 Control of photonemission from nanoparticles with two-color laser fields

3.5.1 Generation of linearly polarized two-color laser pulses

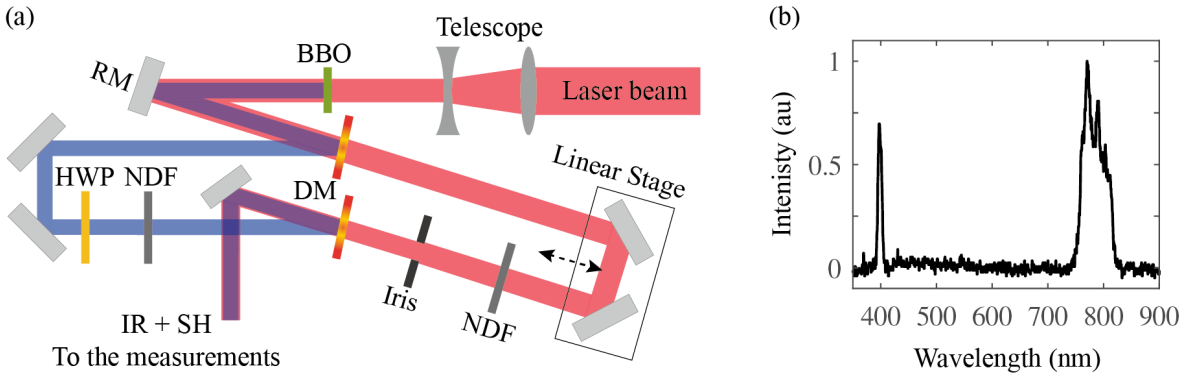

Figure 3.10: (a) Schematic diagram of collinear linearly polarized two-color pulse generation. BBO: Beta-Barium Borate, HWP: half-wave plate, NDF: neutral density filter, DM: dichroic mirror. (b) A typical spectrum of the two-color laser beam.

The schematic diagram of the collinear two-color setup is shown in Fig. 3.10(a). The infrared (IR) laser pulses of 30 fs duration centered at 780 nm at 1 kHz repetition rate with an energy up to 1.3 mJ were obtained from an amplified Ti:Sapphire laser system (details in section 3.4). The linearly polarized IR beam was sent into a telescope (2:1) before entering a Beta-Barium Borate (BBO) crystal, where a second harmonic (SH) pulse was generated with polarization orthogonal to the fundamental. The phase matching angle of the BBO crystal is 29.2 °, which ensures the highest second harmonic conversion efficiency

for 780 nm wavelength pulses. The two-color beams were split by a dichroic mirror and guided into two arms of the Mach-Zehnder interferometer. The polarization of the SH pulse was rotated by 90 ° via a half-wave plate and became parallel to that of the IR pulse. An iris was introduced into the IR arm of the interferometer to regulate the spatial intensity profile. The intensities of the IR and SH components were controlled by neutral density filters in both arms. The field waveform of the output beam was tailored by a computer-controlled high resolution linear translation stage (SLC-1720, SmarAct) in the IR arm of the interferometer. Figure 3.10(b) shows a typical spectrum of the two-color laser beam measured with a spectrometer (CCS200, Thorlabs). The central wavelength of IR beam is 780 nm. The SH peaks at 390 nm, and the full width at half maximum (FWHM) is around 8 nm.

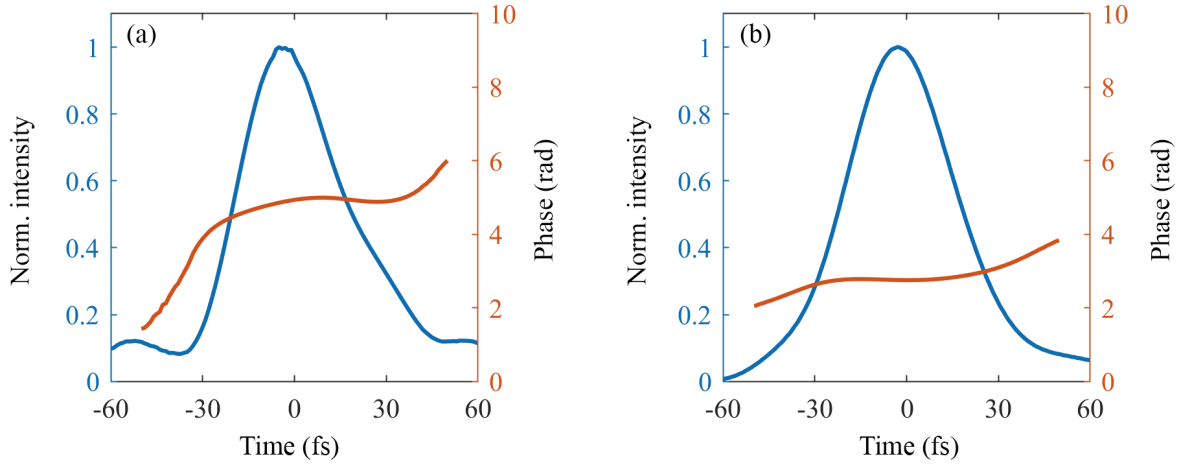

Figure 3.11: The retrieved time dependent intensity and phase for IR (a) and SH (b) laser pulses.

The temporal field shapes of the two-color laser pulses were measured by taking TG-FROG traces for each component independently. The retrieved time dependent intensity and phase are shown in Fig. 3.11. The measured pulse durations (FWHM) of the two spectral components were $\tau_{\mathrm{IR}} \approx 40.0$ fs and $\tau_{\mathrm{SH}} \approx 41.4$ fs, respectively.

The stability of the collinear two-color setup was monitored by sending a frequency stabilized He-Ne laser into the Mach-Zehnder interferometer. The interferometric fringes are shown in Fig. 3.12(a). Change of the relative distances between the two arms of the interferometer is caused by both rapid mechanical vibrations and long-term thermal drifts (see red line in Fig. 3.12(b)). An active stabilization algorithm (proportional–integral–derivative, PID) was implemented by feeding the phase shift signal back to the linear translation stage. The thermal drifts were effectively compensated which ensured a phase stability better than 20 mrad as shown in 3.12(b).

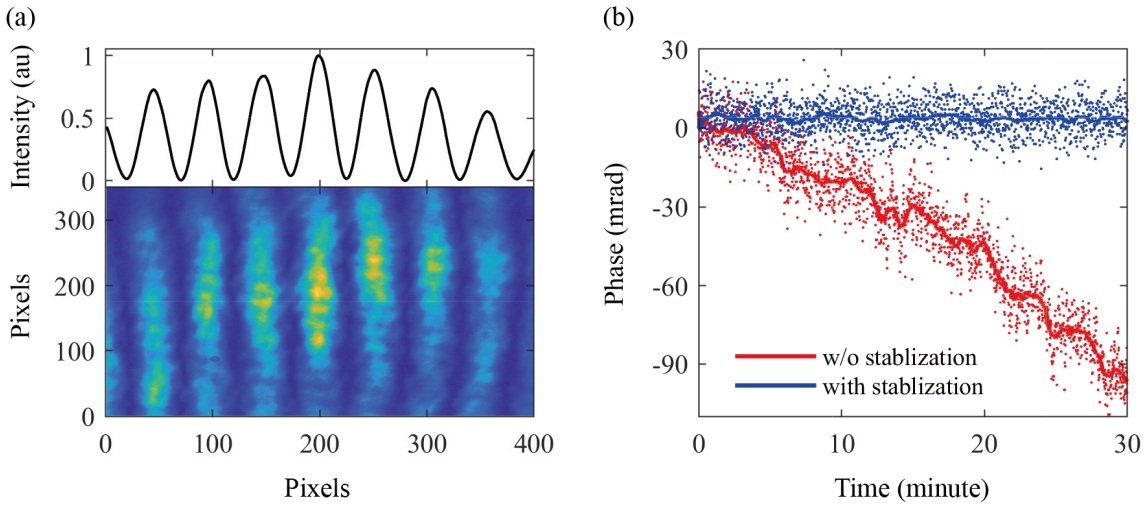

Figure 3.12: (a) The interferometric fringe pattern generated by a frequency stabilized He-Ne laser. The upper panel shows the integrated signal along the vertical direction. (b) The phases retrieved from the interferometric fringes without (red) and with (blue) actively stabilization. The root-mean-square (rms) with actively stabilization is around 6.8 mrad.

3.5.2 Phase resolved photoemission from nanoparticles

The experimental setup for phase resolved photonemission from nanospheres with two-color laser fields is shown in Fig. 3.13(a). The nanoparticles are delivered into the vacuum chamber with a home made nanoparticle source as described in section 3.1. The resulting two-color laser pulses were focused with a 50 cm focal length mirror and intersected the nanoparticle beam in the center of the ion optics of a VMI spectrometer (see details in section 3.3). The electron emission was projected on a MCP/phosphor screen assembly and the resulting image was recorded via single-shot image acquisition (see details in section 3.3).

In the study of phase resolved photoemission from nanoparticles (see Chapter 5), a critical tuning parameter was the intensity ratio between the IR and SH beams. In order to keep the intensity ratios constant all over the laser focus, one has to set the spatial beam profiles of the IR and SH pulses similar. This was achieved by manipulating the beam waist via the iris in the IR arm of the interferometer. The spatial beam profiles of the IR and SH pulses in the focus are shown in Fig. 3.13(b) and (c), respectively. The images were recorded by a CMOS camera (Blackfly, FLIR). The $1/e^2$ diameter of the beam profiles were both approximately 93.0 μm.

In order to collect distinct photoelectron projections at different two-color laser waveforms, the acquisition time was set depending on the count rate from the nanoparticle events but at least 60 seconds per step. The count rate was related to the density of the nanoparticles and the peak laser intensity in the interaction volume. The step size

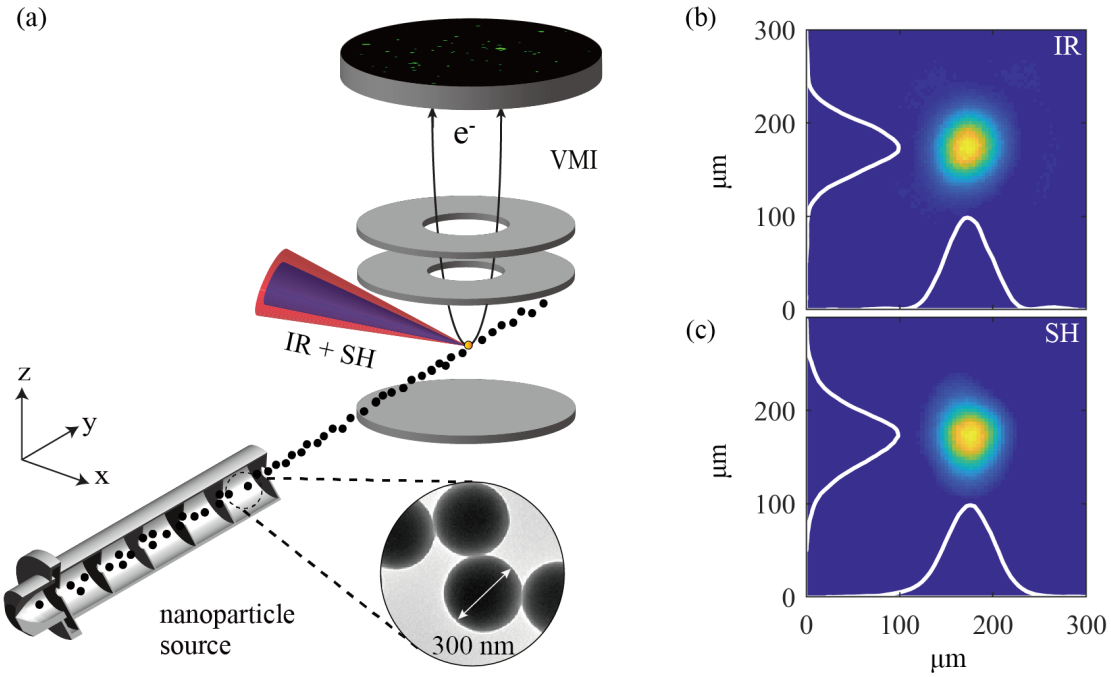

Figure 3.13: (a) Schematic of the experimental setup for phase resolved photoemission from nanospheres with two-color laser pulses. (b) Spatial beam profiles for IR (b) and SH (c) laser pulses in the focus.

of the motorized stage was 10 nm. The total travelling distance of the stage was 600 nm which covered 3 full cycles of the SH laser pulses. A typical successful measurement took approximately 1 hour.

Due to relatively low nanoparticle density only a portion of the recorded single-shot frames contain emitted electrons from aerosolized nanoparticles (approximately 15%). The frames containing photoelectrons from nanoparticles yield larger number of electron events than the frames that contain emitted electrons from background gas only. Figure 3.14(a) shows the histogram of the electrons per shot measured for solution (ethanol) with and without SiO_2 nanoparticles. The typical number of detected electrons from the background gas is less than 20. We selected the frames containing more than 30 electrons as the nanoparticle frames. Figure 3.14(b) shows the corresponding phase-averaged momentum distributions of the photoelectrons from the background gas and from the SiO_2 nanoparticles. The momentum maps were obtained by selecting single-shot frames for backgound gas and nanoparticles, respectively. The two-color pulses were linearly polarized along the y-axis, and propagated along the x-axis from negative to positive direction. The momentum maps from background gas and nanoparticles (as indicated in Fig. 3.14(b)) are both symmetric with respect to the laser polarization direction. The momentum distribution from nanoparticles were asymmetric with respect to the laser propagation direction due

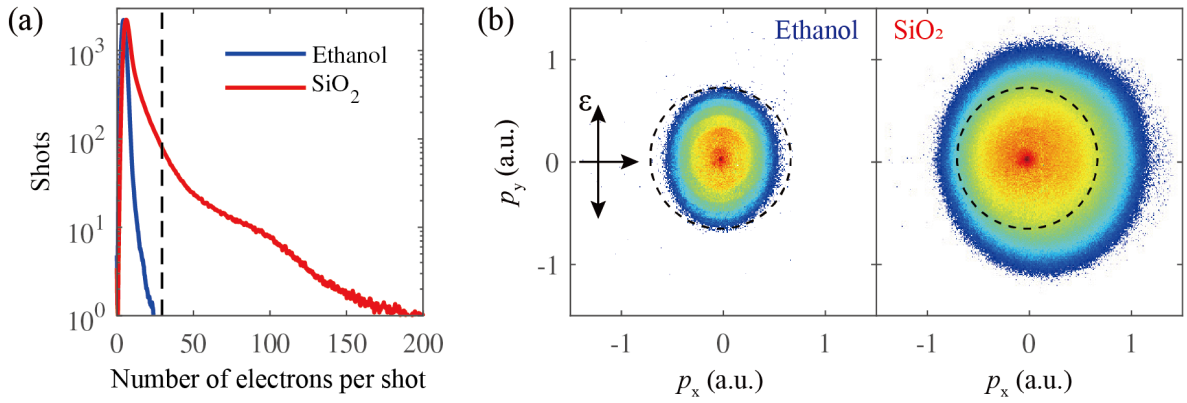

Figure 3.14: (a) The histogram of the number of electrons per shot measured for solution (ethanol) with and without SiO_2 nanoparticles. (b) The respective phase-averaged momentum distributions of the photoelectrons from the background gas and from the SiO_2 nanoparticles. The dashed line indicates the cutoff moentum for background gas.

to the field propagation effect where the laser fields were enhanced at the backside of the nanoparticle (with diameter of $d = 300\,\text{nm}$) [48]. Please notice that the frames identified as nanoparticle frames also contain emitted electrons from the backgound gas. Fortunately, the photoelectrons from the backgound gas only contributed to low momenta signals, the high momenta signals ($p_\text{r} > 0.7$ a.u.) were dominated by photoelectrons from the SiO_2 nanoparticles.

3.5.3 Angular dependent momentum cutoff

Typically, the signal-to-noise ratio near the cutoff of photoemission projections recorded by the VMI is limited [48, 66, 68]. Here we introduce a novel method to extract the angular and phase-resolved electron energy cutoffs from photoemission projections. Figure 3.15(a) shows a typical projected momentum map from M^{3}C simulation with 300 nm SiO_2 nanospheres. The incident two-color pulses were polarized along the y-axis with a fixed relative phase $\phi_\text{rel} = 0$. The peak intensities of the two-color pulses ($\omega/2\omega$) were both set to $3 \times 10^{12}\,\text{W/cm}^2$. More electrons are emitted to positive p_y as compared to negative p_y due to the asymmetric shape of the driving field. In addition, the electrons are preferentially emitted towards the backside of the nanosphere (p_x) because of the field propagation-induced directional photoemission [48]. The projected momentum map will flip along the laser propagation direction if the relative phase between ω and 2ω changes by π. It is intuitive to visualize the angular and phase dependence by calculating a radial asymmetry map for different electron emission angles. The maps are obtained by angular integration within an angular interval of $\Delta\theta = 1°$ (indicated with red and blue shades in Fig. 3.15(a)) according to the center of the map. The signal is integrated in radial segments and the

relative difference is calculated as:

$$A_\theta(p_\mathrm{r}, \varphi_\mathrm{rel}) = \frac{S_\theta\left(p_\mathrm{r}, \varphi_\mathrm{rel}\right) - S_{-\theta}\left(p_\mathrm{r}, \varphi_\mathrm{rel}\right)}{S_\theta\left(p_\mathrm{r}, \varphi_\mathrm{rel}\right) + S_{-\theta}\left(p_\mathrm{r}, \varphi_\mathrm{rel}\right)}. \tag{3.1}$$

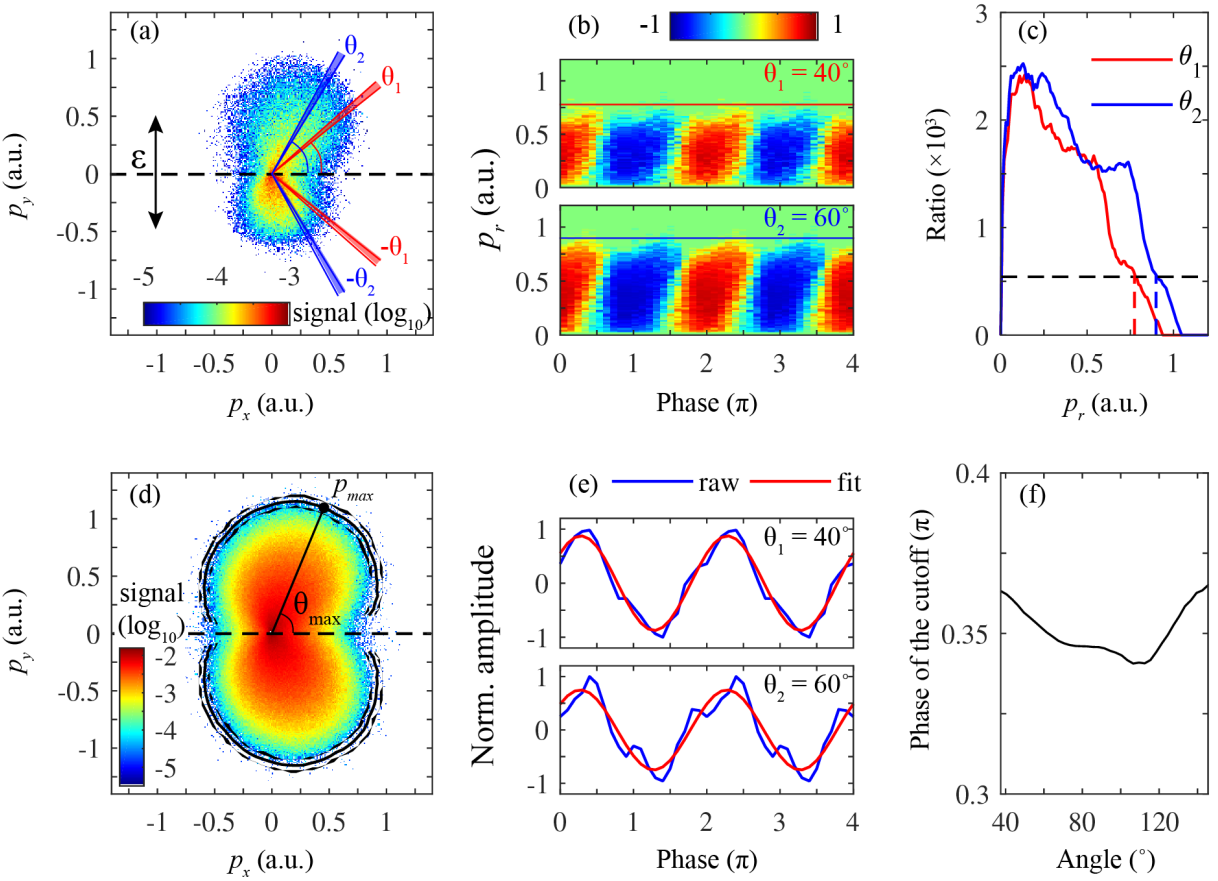

Figure 3.15: A typical projected momentum map from M^{3}C calculation. The two-color pulses are polarized along the y-axis. The IR and SH intensities are both set to 3×10^{12} W/cm^2. The angular and phase-resolved electron cutoffs are obtained accordingly from (a) to (f). See the details in the text.

The two panels in Fig. 3.15(b) show the typical radial asymmetry maps with $\theta_1 = 40°$ and $\theta_2 = 60°$, respectively. Fast Fourier transformation (FFT) is performed at each momentum. Figure 3.15(c) shows the amplitude ratio between the main frequency (relative phase periodicity) and the noise. The cutoffs for all angles are obtained by selecting a threshold appropriately (c.f. dashed line in Fig. 3.15(b)). The superposed momentum maps of all relative phases and the angular cutoffs are shown in Fig. 3.15(d) together with the angular cutoffs. The cutoffs are extracted reasonably for each angle. The maximum

momentum $p_{\text{cutoff}}^{\max}$ (critical cutoff) and the corresponding angle $\theta_{\max}$ (critical angle) can be obtained accurately. It should be noted that the angular resolved cutoffs are found to be sensitive to the threshold. In practice, one could decrease the threshold until the signal decays to the noise level.

Furthermore, the modulation S_θ of the yield at the cutoff positions can be assumed to be dominated by a harmonic dependence on the relative phase ϕ_{rel}. Therefore S_θ can be expressed as:

$$S_\theta(p_{\text{cutoff}}, \phi_{\text{rel}}) = A_\theta(p_{\text{cutoff}})cos(\phi_{\theta,\text{rel}} + \Delta\phi_{\theta,\text{rel}}) + C_\theta, \tag{3.2}$$

where $A_\theta(p_{\text{cutoff}})$ is the modulation amplitude, $\Delta\phi_{\theta,\text{rel}}$ is the phase offset to $\phi_{\theta,\text{rel}}$, and C_θ is the constant offset. The fitting results corresponding to the angles θ_1 and θ_2 are shown in Fig. 3.15(e). The angular resolved relative phase shift of the electron cutoffs are shown in Fig. 3.15(f). The relative phase dependent analysis requires a sufficient signal in the cutoff area. This could be mitigated by integrating the signals in a certain range (e.g. $[p_\theta \pm 0.05\, a.u.]$).

3.6 Attosecond streaking metrology with isolated nanoparticles

3.6.1 Generation of isolated attosecond pulses

The attosecond setup (in the group of Prof. F. Calegari and Prof. M. Nisoli, Politecnico di Milano) is especially designed to achieve sufficiently high photon flux to perform time-resolved spectroscopy of low-density targets such as isolated nanoparticles. The setup is driven by near-infrared (NIR), sub-4 fs, 2.5 mJ pulses obtained by hollow-core fiber compression of 25 fs, 6 mJ, 780 nm pulses from a commercial Ti:sapphire laser system (Femtopower V Pro CEP, Spectra-Physics). To achieve maximum coupling efficiency, the hollow-core fiber compressor is operated in pressure-gradient configuration. The residual single-shot carrier-envelope phase (CEP) fluctuation of the driving pulses is $\sim$ 200 mrad (rms) [134]. A schematic of the attosecond setup is shown in Fig. 3.16(a). A portion of the NIR beam (70 %) is focused by a 1 m radius-of-curvature spherical mirror into a static gas cell filled with a noble gas to produce extreme ultraviolet (XUV) radiation by high-order harmonic generation. A continuous emission spectrum corresponding to isolated attosecond pulses is achieved with the polarization gating technique [135]. A pair of fused silica wedges is used to properly adjust dispersion and CEP of the NIR driving pulses. The fundamental radiation and the energy region of the spectrum below 16 eV are filtered out by a 100 nm thick aluminium filter. The remaining portion of the NIR beam (30 %) is properly delayed with attosecond resolution by using a piezo-stage and then collinearly recombined with the XUV beam by using a drilled mirror with a 3 mm diameter central hole in an interferometric configuration. The interferometer is actively stabilized using a frequency stabilized He-Ne laser.

An additional pair of fused silica wedges is used to properly adjust dispersion and CEP

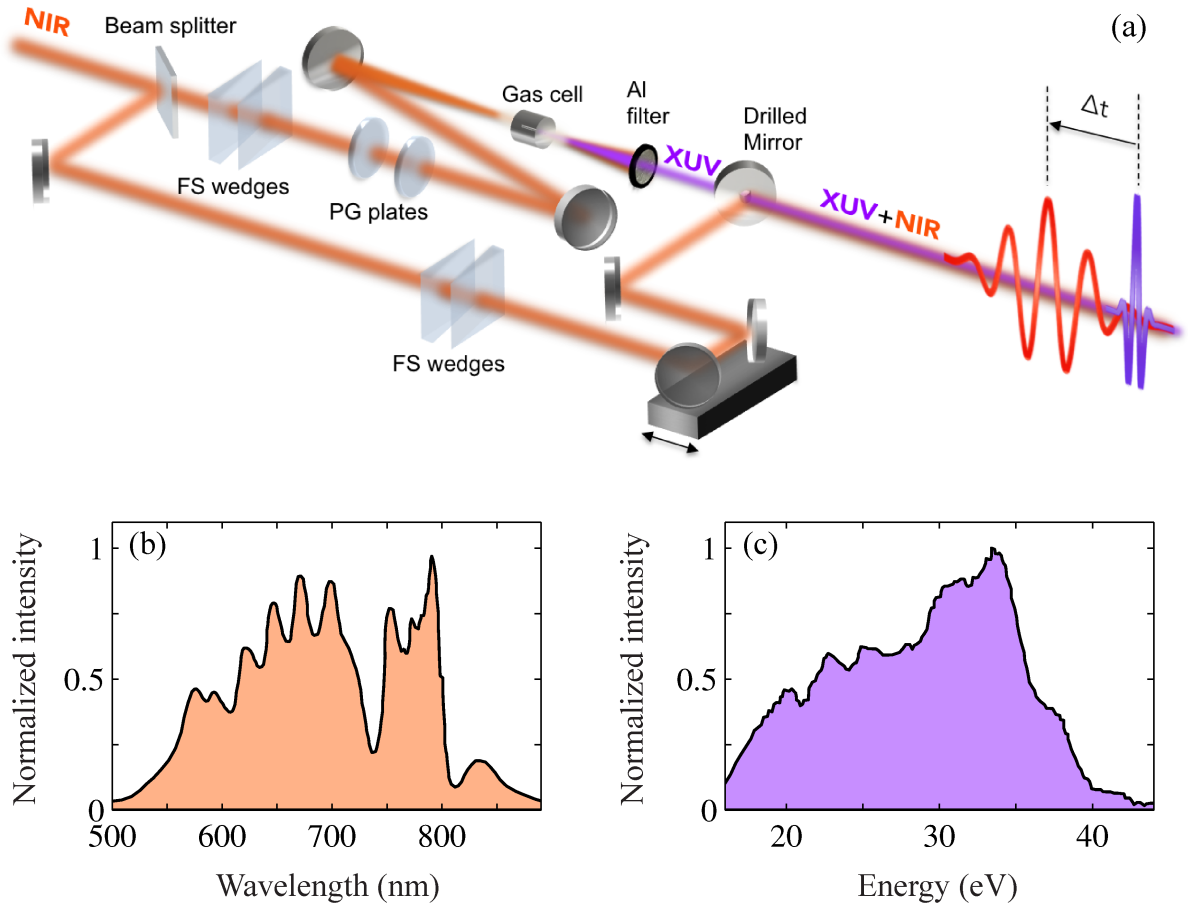

Figure 3.16: (a) Attosecond interferometer used for streaking measurements. Polarization gating (PG) optics were used to properly manipulate the polarization of the driving pulse. Fused silica (FS) wedges in both arms permitted to adjust the dispersion and the CEP of the NIR pulses. Typical near-infrared (NIR) and XUV spectra are shown in (b) and (c), respectively.

of the NIR probe pulses. A gold-coated toroidal mirror ($f = 90\,\text{cm}$) is used to focus both the XUV and NIR pulses into a beam of nanoparticles and the resulting electron photoemission is detected with a single-shot VMI spectrometer (details in section 3.3.3) [123, 129, 136]. The toroidal mirror is operated in Rowland configuration with unity magnification and provides an almost aberration-free image of the XUV source, with a negligible temporal smearing of the attosecond pulses. The angle of incidence is 86 °. The spectral characterization of the XUV radiation is simultaneously achieved by using a high-resolution flat-field soft x-ray spectrometer consisting of a second gold-coated toroidal mirror, followed by a grating, a microchannel plate (MCP), a phosphor screen, and a charge-coupled device (CCD) camera [137]. The angle of incidence of the toroidal mirror is

86 ° and two gratings (Hitachi 001-0639 and 001-0640) are used to cover the energy range 12-100 eV. As can be seen from Fig. 3.17, completely tunable XUV emission covering the energy region between 16 eV and 45 eV can be achieved by using different generation gases (xenon, krypton or argon). The XUV photon flux has been measured on target by using a National Institute of Standard and Technology (NIST) calibrated open photo-diode. The current from the photodiode, proportional to the number of incidence photons, is read by a Keithley amperemeter. When generating XUV pulses in xenon, the energy in the case of continuous spectra is ~ 4 nJ, measured after a 100 nm thick aluminum filter used to block the fundamental radiation. Such an energy corresponds to $\sim 8 \times 10^8$ photons/pulse (or $\sim 8 \times 10^{11}$ photons/sec for a repetition rate of 1 kHz of the laser system).

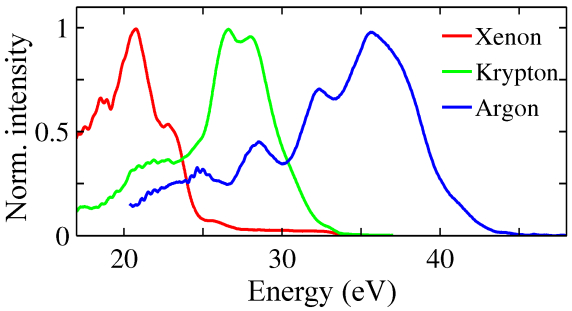

Figure 3.17: Continuous XUV spectra generated in xenon (red curve), krypton (green curve) and argon (blue curve). The spectra have been acquired by using a high-resolution flat-field soft x-ray spectrometer. Full tunability between 16 eV and 45 eV is achieved. Adapted from [114].

To temporally characterize the XUV and NIR pulses, the attosecond beamline is also equipped with a time-of-flight (TOF) spectrometer to perform attosecond streaking in a gas target. For reconstruction of the laser fields the Frequency-Resolved-Optical-Gating for Complete-Reconstruction-of-Attosecond-Bursts (FROG-CRAB) technique is used [118]. Measured and reconstructed streaking traces are presented in Fig. 3.18(a) and Fig. 3.18(b), respectively. The retrieved temporal intensity profile and phase of the XUV pulses are shown in Fig. 3.18(c). A pulse duration of 250 as is typically achieved using this scheme.

3.6.2 Experimental setup for attosecond streaking on nanoparticles

The setup for single-shot attosecond VMI with nanoparticles is schematically shown in Fig. 3.19. The delay-controlled XUV and NIR pulses propagated collinearly in positive direction along the x-axis, and were polarized along the y-axis. The nanoparticle stream was injected into the interaction region by an aerodynamic lens along the y-axis. The homogeneous static electric fields between the electrodes accelerated photoelectrons towards the MCP/phosphor screen detector. The supply voltages of the detector were gated by a

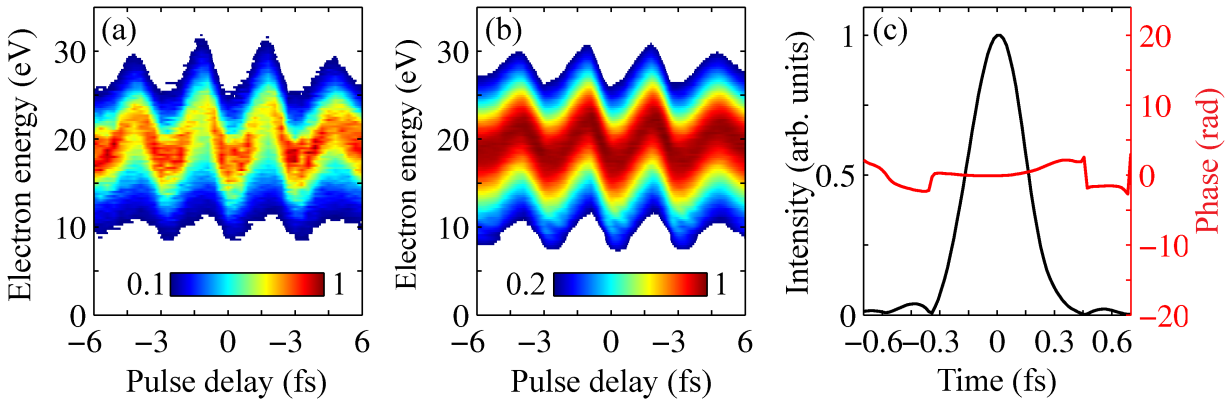

Figure 3.18: Attosecond pulse characterization. (a) Attosecond streaking spectrogram measured in argon and (b) retrieved FROG-CRAB trace. (c) Reconstructed temporal intensity profile of the XUV pulse. The retrieved pulse duration was 250 ± 20 as Full-Width-at-Half-Maximum (FWHM) with a residual parabolic phase indicating the presence of small second-order dispersion. The second-order dispersion value was determined in-situ in the main experiments from residual gas data.

fast high-voltage switch with a gate width of 300 ns to reduce background contributions. The velocity-map images on the phosphor screen were recorded by a CMOS camera which was operated at the laser repetition rate (1 kHz) with a resolution of 800 × 600 pixels, and the exposure time was 0.1 ms. For each image the camera software (Marathon Pro, GS Vitec) applied a flat-field correction, and up to 1024 pixels with a brightness above a defined threshold were recorded (see section 3.3.3 for details). The camera and the fast high voltage switch were both synchronized to the laser with suitably delayed TTL-trigger signals.

3.6.3 Single-shot data discrimination

The single-shot data discrimination is related to recent coincidence experiments, where the attosecond streaking from two different gases could be simultaneously measured and distinguished in the data analysis [20]. Without such approaches, either the emission bands have to be spectrally well separated (see e.g. [58, 138]), or measurements have to be taken consecutively, which is, however, difficult due to typically limited long-term interferometer stability. The latter would pose a severe problem for measurements on dilute targets, where acquisition times are long (typically in the range of 45-60 min at 1 kHz for one streaking measurement on nanoparticles).

Due to the magnification setting of the imaging lens, a single electron hit on the MCP/phosphor assembly can illuminate several pixels on the CMOS chip. For sufficiently low density of hits on the detector per laser shot, a centroiding algorithm can be used to uncover the number of electrons recorded in single-shot images (more details in section

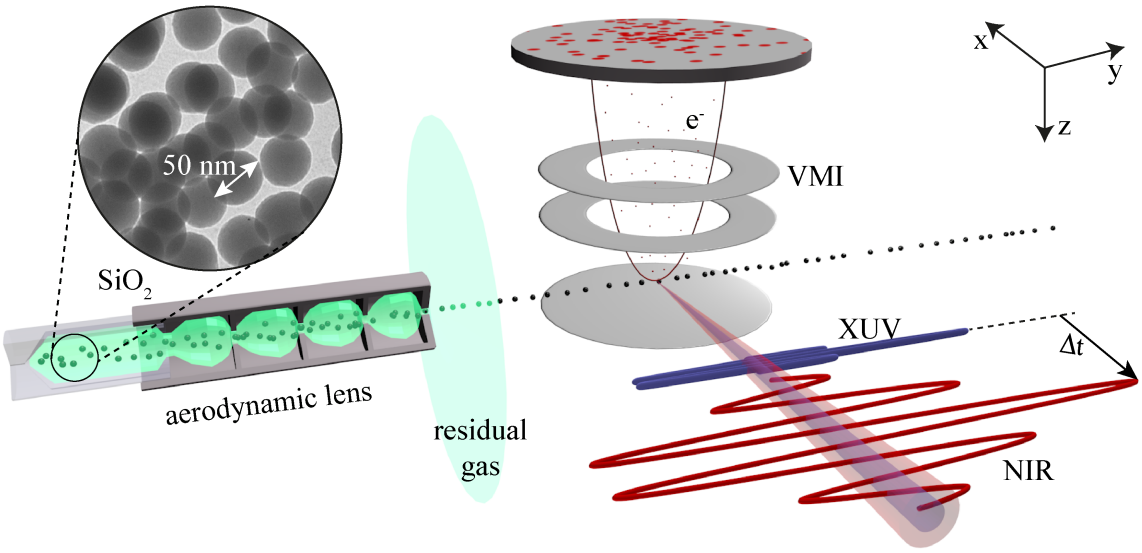

Figure 3.19: Schematic of the experimental setup for attosecond streaking experiments on nanoparticles. A beam of isolated nanoparticles is illuminated with few-cycle NIR and XUV pulses along the y-axis. The inset shows the transmission electron micrograph of the SiO_2 nanoparticles with a diameter of 50 nm. The XUV and NIR pulses propagate in positive direction along the x-axis, and are polarized along the y-axis. The electron emission is projected with a static electric field onto the MCP/phosphor screen assembly of the VMI spectrometer and each shot is detected with a fast CMOS-camera outside of the vacuum chamber (not shown). Taken from [42].

3.3.3). Examples for post-processed single-shot images of the 2D electron momenta (x and y components), as obtained from the residual gas only and for SiO_2 nanoparticles, are shown in Fig. 3.20(a) and (b), respectively. The laser pulses propagated along the p_x axis, and were polarized along the p_y axis. The number of electrons emitted per laser shot from nanoparticles (Fig. 3.20(b)) was typically much larger than from the residual gas (Fig. 3.20(a)). For the residual gas frames, single ionization by the XUV is expected to dominate, and the detected electrons therefore originate predominantly from different gas atoms or molecules present in the interaction region. For nanoparticles hit by the XUV, typically more electrons are emitted and show an asymmetry along the laser propagation direction, as depicted in Fig. 3.20(b). The asymmetry manifests as more electrons appearing on the left side of the image, corresponding to the incident side along the laser propagation axis. This effect is known as shadowing [25, 139, 140], and originates from the asymmetric absorption of the attosecond XUV light in the nanoparticle.

Figure 3.20(c) shows the histogram of detected electrons per shot for nanoparticles (red line), compared to just residual gas (blue line). Both measurements were performed under identical conditions (laser intensity and experimental chamber pressure $< 2 \times 10^{-7}$ mbar),

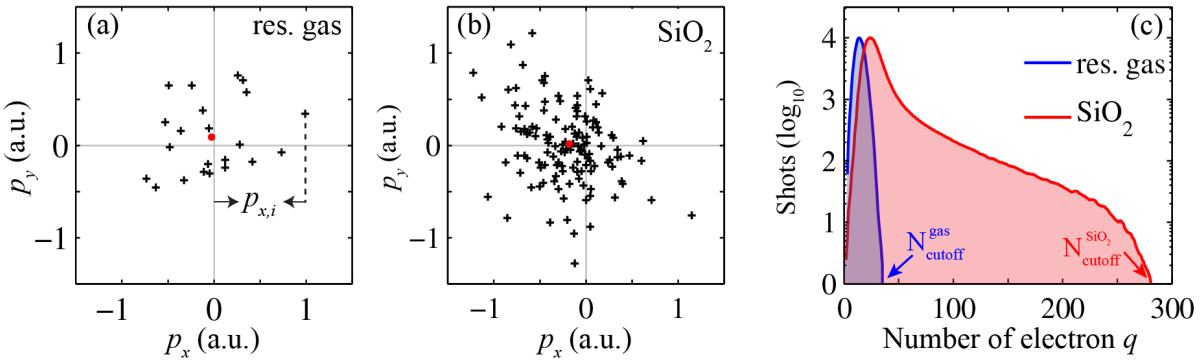

Figure 3.20: Post-processed single-shot momentum images (projected along p_z) of the electron emission for (a) residual gas and (b) SiO_2 nanoparticles obtained in the XUV-NIR streaking experiments. The red dots show averages of the momentum distributions. The asymmetry in the photoelectron momentum distribution along the laser propagation direction (p_x) originates from preferential absorption of XUV light on the front side of the nanoparticle (shadowing). (c) Histogram of the number of hits per frame measured with only ethanol in the evaporator (residual gas, blue line) and SiO_2 nanoparticles dispersed in ethanol (red line).

by using the evaporator with just ethanol and with a nanoparticle-ethanol dispersion. Without nanoparticles, the number of electrons per shot has a sharp upper cutoff $N^{Gas}_{cutoff} = 40$. For the nanoparticle dispersion, the maximum number of electrons per shot goes up to $N^{SiO_2}_{cutoff} = 270$ and 15% of the shots recorded more than 50 electrons, which clearly arise from emission from SiO_2 particles.

3.7 CEP controlled photoemission from nanoparticles

3.7.1 Stereo time-of-flight setup and data acquisition

As described in section 3.3, the VMI technique offers us the probability to detect both kinetic energy and angular distributions of the charged particles. But the kinetic energy detection range is below 1.2 KeV [141], and restricts the applications in high energy photoemission measurements. A stereo time-of-flight (STOF) which consists of two symmetric TOF spectrometers can be employed to extend the measurements to much larger kinetic energy detection range (> 2 keV).

Figure 3.21 outlines the STOF setup [130]. Briefly, a linearly polarized few-cycle laser pulse illuminates on a nanoparticle stream in the middle of the two spectrometers. The spectrometers stand facing each other, and collect the photoemitted electrons along the polarization direction (z-axis). The birth time of the photoelectrons was defined as the detection time of the scattered lights. The arrival time of a single electron event was

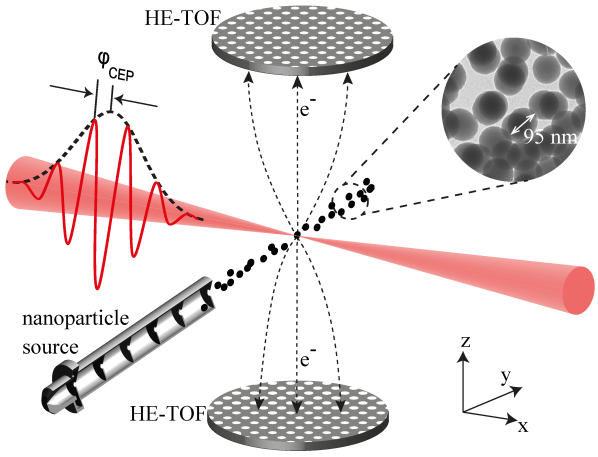

Figure 3.21: Schematic of the stereo time-of-flight setup. A linearly polarized few-cycle laser pulse illuminates on a nanoparticle stream in the middle of two symmetrical time-of-flight spectrometers. The spectrometers stand facing each other, and collect the photoemitted electrons along the polarization direction (z-axis). The inset shows the transmission electron microscopy (TEM) image of SiO_2 nanoparticles with a diameter of 95 nm.

obtained by the peak detection algorithm using a gate open and close threshold. In combination with the length of the drift tube (50 cm), the time resolution of the digitizer and the approximated 300 ps trigger jitter of the delay generator, the energy resolution is 2 % at 1 keV. The inset of Fig. 3.21 shows the transmission electron microscopy (TEM) image of SiO_2 nanoparticles with a diameter of 95 nm. The delivery of the nanoparticle stream via the aerodynamic lens system is described in detail in section 3.2. For reference scans, neon gas could be injected into the laser focus through a gas nozzle. The background pressure was 2×10^{-8} mbar, and with the nanoparticle source on was 2×10^{-7} mbar. The STOF spectrometer was provided by Prof. Meiwes-Broer, Universität Rostock.

3.7.2 Data analysis and pulse characterization

The time-of-flight spectra are recorded for both channels in each laser shot, the momentum spectra can be obtained by converting the flight times into initial momentum. The rebinning for the exact phase retrieval yields the phase dependent spectra. Figure 3.22(a) shows the momentum spectra of photoelectrons measured on Ne gas with two different CEPs. The laser intensity is 2.6×10^{14} W/cm^2 calculated from the cutoff energy. The direct electrons are driven by the laser field up to energies of 2 U_p, which dominate the low energy regime (left), here U_p is the ponderomotive energy. The higher energy electrons are ionized and driven back towards the parent ion by the external laser field, and gain more energy – up to 10 U_p – from the external field after rescattering [142]. The scattered electrons exhibit a strong CEP dependence due to the fact that the recollision of electrons

with the core is highly dependent on the shape of the electric field of the few-cycle pulses [106].

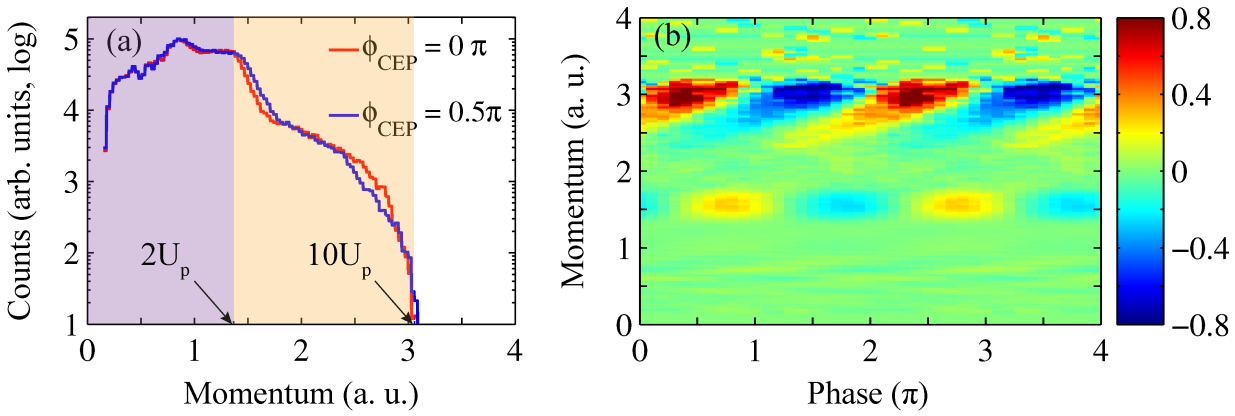

Figure 3.22: (a) Momentum spectra of photoelectrons measured on Ne gas. The laser intensity is $2.6 \times 10^{14}\,\mathrm{W/cm^2}$. (b) The asymmetry map calculated from the phase tagged spectra.

The CEP dependent asymmetrical photoemission with respect to the laser propagation axis can be intuitively visualized by calculating the relative difference between the momentum spectra from the symmetrical time-of-flight channels. The phase retrieval asymmetry map is calculated by:

$$A(p_z, \varphi_{cep}) = \frac{S_1\left(p_z, \varphi_{cep}\right) - S_2\left(p_z, \varphi_{cep}\right)}{S_1\left(p_z, \varphi_{cep}\right) + S_2\left(p_z, \varphi_{cep}\right)}, \tag{3.3}$$

where S_1 and S_2 are the CEP rebinned momentum spectra obtained by the two time-of-flight channels. Figure 3.22 shows the asymmetry map calculated from the phase tagged spectra measured on Ne gas. The absolute CEP was determined from a comparison with TDSE simulation. The asymmetry pattern exhibits a strong CEP dependence, and shifts to higher CEPs with increasing momentum of the rescattered electrons.

The cutoff energy of the photoelectrons was obtained from the CEP averaged TOF spectrum. Figure 3.23 shows a typical TOF spectrum for a 95 nm SiO_2 nanoparticle measurement. The laser intensity is $1.5 \times 10^{14}\,\mathrm{W/cm^2}$ which characterized by a reference scan in Ne gas. The small peak close to zero delay time is produced by photons, and exhibits a long exponential tail. Two methods were used to obtain the cutoff energies. In the first one the cutoff is defined at the position in the TOF spectrum where the signal reaches the noise level (indicated by (1) in the inset of Fig. 3.23). Due to the low signal-to-noise ratio in the cutoff region, especially the overlaps between the high-energy electron events and the light peak at high laser intensities, the exact cutoff energy cannot be assigned unambiguously with this method. The time-of-flight spectrum shows a nearly linear decay

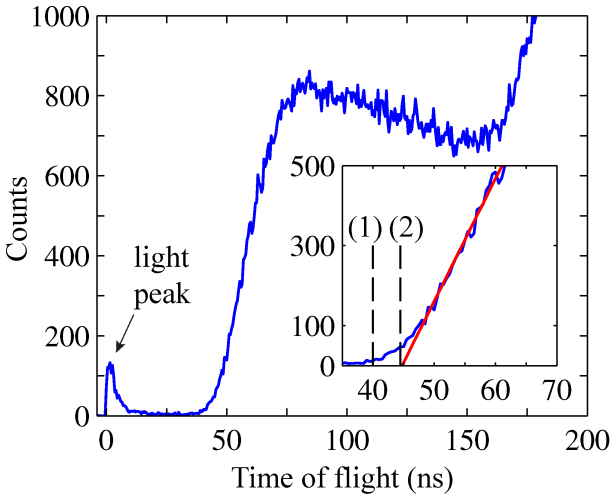

Figure 3.23: Time-of-flight spectrum of a SiO_2 measurement at an intensity of $1.5 \times 10^{14}\,W/cm^2$. The inset illustrates the two methods for determining the cutoff. Adapted from [130].

in the higher energy range (shorter flight time). This feature permits a cutoff by fitting the spectrum linearly, as shown by (2) in the inset of Fig. 3.23. The final cutoff energy was obtained by averaging the results of both methods. The trigger jitter and digitizer resolution were taking into account as the systematic error.

Chapter 4

Attosecond chronoscopy of electron scattering in dielectric nanoparticles [1]

4.1 Introduction

For electron energies in the tens-of-electronvolt range, collisions typically occur in the sub-femtosecond range. We have access to this timescale via attosecond streaking as described theoretically and experimentally in section 2.5 and section 3.6, respectively. Briefly, photoemission inside a solid is initiated by an extreme ultraviolet (XUV) pulse, and the momentum change of released electrons due to a second near-infrared (NIR) pulse is measured as a function of XUV/NIR pulse delay. To date, this metrology has been successfully applied to metals or adlayer-covered metals [18–23, 25–27], where the NIR streaking field takes effect only on the surface of the material. The physics for dielectrics, however, is fundamentally different as the released electrons are streaked by the NIR field also inside the solid. Most importantly, until now accumulative charging induced by the XUV pulse has prevented the application of attosecond streaking to dielectrics. We solve this problem by using a continuous stream of nanoscopic targets. By merging the attosecond streaking metrology and nanoparticle aerosol generation technology, the proof-of-concept study on attosecond chronoscopy of electron scattering in 50 nm SiO_2 nanoparticles will be reported in this chapter. The relative attosecond streaking delay measurements are permitted by recording the attosecond photoemission from residual gas (time reference) and nanoparticles simultaneously. The theoretical work based on M^3C model shows that streaking delays are a measure for inelastic scattering of electrons in dielectric materials.

4.2 Count rate estimation

For the typically employed low nanoparticle densities on average less than one nanoparticle is present in the central, high intensity region of the laser focus. Therefore, even when

[1] The results in this Chapter were published in [42, 114].

using the nanoparticle dispersion, the frames contain signal from residual injection gas and possibly one or few nanoparticles. In order to quantify the effects of the nanoparticle density, nanoparticle beam parameters and the focal laser intensity profile on the single-shot electron number distribution, we introduce a simplified hit statistics model that is based on the schematic setup shown in Fig. 4.1(a). The number density of SiO_2 nanoparticles in the beam is modeled by a Gaussian distribution

$$n(\mathbf{r}) = n_0 \exp(-2(x^2 + z^2)/\omega_{\mathrm{np}}^2) \tag{4.1}$$

where $n_0 = 2 \times 10^6\,\mathrm{cm}^{-3}$ is the density in the center of the nanoparticle beam and $\omega_{\mathrm{np}} = 500\,\mu\mathrm{m}$ characterizes the beam width [66]. The XUV fluence (number of photons per unit area) in the focus region is described by a Gaussian beam as

$$F(\mathbf{r}) = \frac{2N_{\mathrm{phot}}}{\pi\omega_{\mathrm{xuv}}(x)^2} \exp(-2(y^2 + z^2)/\omega_{\mathrm{xuv}}(x)^2) \tag{4.2}$$

with $\omega_{\mathrm{xuv}}(x) = w_0\sqrt{1 + (x/x_R)^2}$ the beam waist at position x on the optical axis, $\omega_0 = 10\,\mu\mathrm{m}$ the beam waist at focus, and $x_R = 8\,\mathrm{mm}$ the Rayleigh length. The total number of photons in a single laser shot was $N_{\mathrm{phot}} = 2 \times 10^8$. We now assume that every photon falling into the geometrical cross section $\sigma_{\mathrm{geo}} = \pi R^2$ of a nanoparticle with radius $R = 25\,\mathrm{nm}$ is absorbed and generates a photoelectron. This assumption is well justified considering the corresponding attenuation length for the XUV radiation. Considering that each photoelectron is detected with probability η, we can introduce a reference fluence

$$F_{\mathrm{single}} = \frac{1}{\eta\sigma_{\mathrm{geo}}} \tag{4.3}$$

that specifies the fluence needed to generate on average one detected electron per nanoparticle. As a result, the absolute fluence F can conveniently be expressed as a relative fluence $f = F/F_{\mathrm{single}}$ that specifies the on average expected measurable electron number per nanoparticle.

In the next step, a simplified rate equation model is employed to describe the probability p_q for measuring q electrons at a given relative fluence. Departing from the initial condition $p_q = \delta_{q,0}$ for vanishing fluence, the corresponding probability distribution $p_q(f)$ follows from integrating the coupled rate equations

$$\frac{dp_0}{df} = -p_0 \qquad \text{and} \tag{4.4}$$

$$\frac{dp_q}{df} = [p_{q-1} - p_q] \qquad \text{for } q > 0, \tag{4.5}$$

as illustrated in Fig. 4.1(c). Integrating over a sufficiently large control volume V that can be chosen to contain an integer number $N_V = \int n(\mathbf{r})$ of nanoparticles yields the probability distribution $P_q = \int p_q(f(\mathbf{r}))d^3r$ for measuring a specific electron number q from a nanoparticle. Note that the distribution P_q so far reflects only the result for a

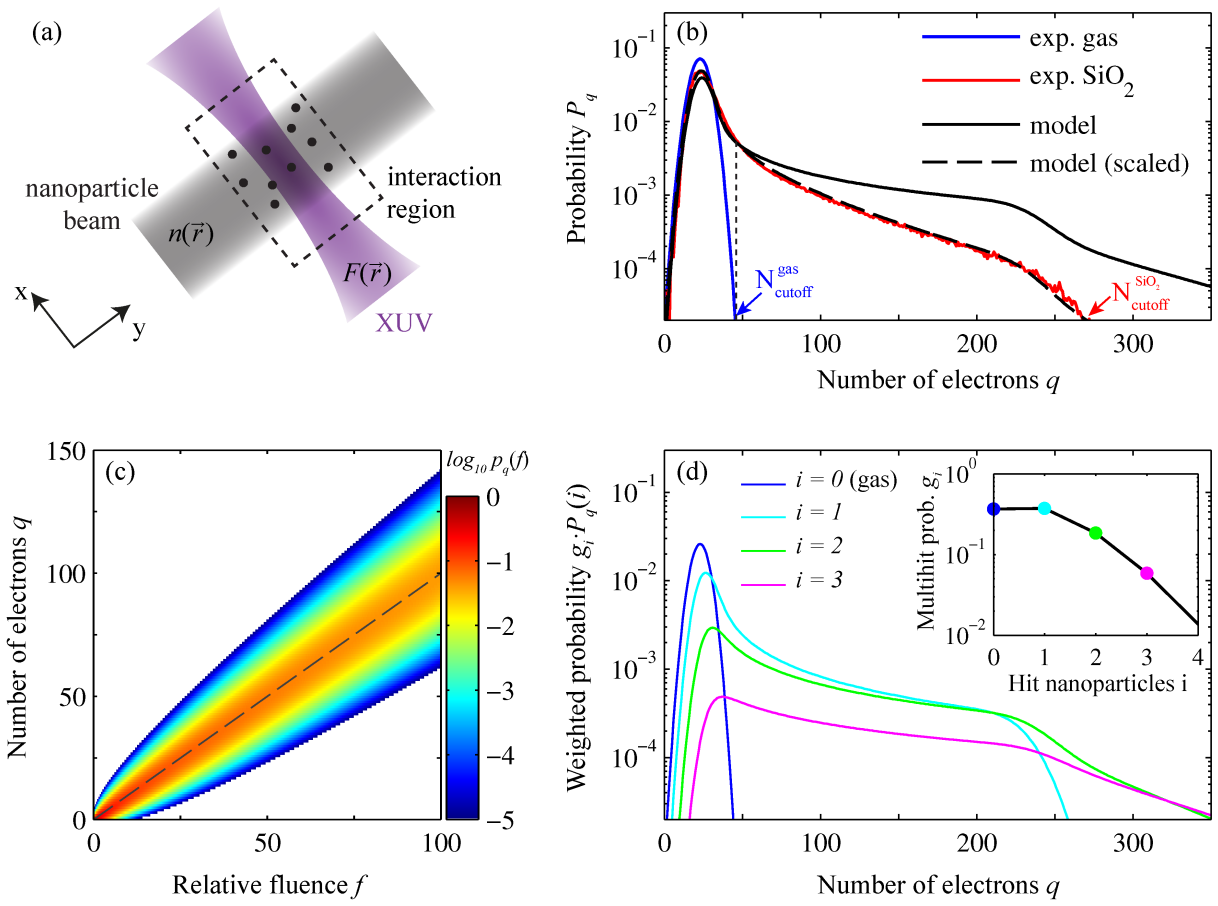

Figure 4.1: (a) Schematic representation of the XUV and nanoparticle interaction region and the control volume V (dashed rectangle) including N_V nanoparticles. (b) Probabilities to detect q electrons measured from gas (blue) and nanoparticle-gas mixture (red), and calculated from the hit statistics model (solid black). Here the photoelectron detection probability was $\eta = 8.5\,\%$. The dashed curve reflects the calculation result scaled with an exponential damping function $\exp(q/q_{\mathrm{sat}})$, with parameter $q_{\mathrm{sat}} = 100$. (c) Single-particle propability distribution $p_q(f)$ in dependence of relative fluence. (d) Weighted multihit probability distributions $g_i P_q^{(i)}$ for hitting $i = 0 \ldots 3$ nanoparticles. Note that the blue curve ($i = 0$) reflects the gas result. The inset shows the respective multihit probabilities g_i. Taken from [114].

single nanoparticle and is normalized automatically to $\sum_{q=0}^{\infty} P_q = 1$. The probability to hit a selected specific nanoparticle in the control volume is $P_{\mathrm{hit}} = \sum_{q=1}^{\infty} P_q$.

Based on this individual hit probability and using a known number of nanoparticles N_V in the control volume we can introduce the multihit probability to simultaneously hit

i nanoparticles as

$$g_i = \binom{N_V}{i} (P_{\mathrm{hit}})^i (1 - P_{\mathrm{hit}})^{N_v - i}. \tag{4.6}$$

The resulting multihit probabilities for the given parameters and for $i = 0 \ldots 3$ are displayed in the inset of Fig. 4.1(d). Note that for the case of $i = 0$ only residual gas signal is considered. Starting from the corresponding electron number distribution for residual gas $P_q^{(0)}$, which can be taken from the experiment, the electron number distribution for a given number of simultaneously hit particles i follows as

$$P_q^{(i)} = \sum_k \sum_l P_k^{(i-1)} P_l \delta_{q,k+l} \quad \text{for } i > 0. \tag{4.7}$$

The finally measurable electron number distribution results from the weighted sum of the individual multihit distributions via $P_q^{\mathrm{tot}} = \sum g_i P_q^{(i)}$. Figure 4.1(d) shows the relevant terms $g_i P_q^{(i)}$ $(i = 1 \ldots 3)$ from this summation and the final result is compared to the experiment in Fig. 4.1(b).

The simulated electron number distribution shows similar features as the experimental data, i.e. the pronounced residual gas peak and a plateau like feature up to high electron numbers. However, the slope of the distribution in the plateau region is steeper in the experiment. Scaling the calculated results with an exponential damping function (dashed curve in Fig. 4.1(d)) can reproduce the experimental data. While the origin of such scaling effects in the experiment is unclear, we like to point out that the model has neglected contributions due to shot to shot fluctuations of the XUV pulse energy, quenched electron emission resulting from Coulomb blockade effects or saturation in the electron detection.

In order to select the frames that contain photoemitted electrons from SiO_2 nanoparticles, we quantified the asymmetry in the electron emission (details in section 3.6). The single frame distributions as a function of $\langle p_x \rangle$ and the number of electrons per frame are presented in Fig. 4.2(a) for a measurement with nanoparticles injected in the interaction region. The black solid line indicates the weighted average of $\langle p_x \rangle$ of the frames with different numbers of electrons. The frames below the blue line (36 electrons) contain less electrons symmetrically distributed, and are assigned to residual-gas-only frames. This can be verified by an independent residual-gas-only measurement with similar laser conditions, as shown in Fig. 4.2(b). The residual-gas-only frames contain less than 30 electrons and the average momentum distribution is symmetric with respect to the laser propagation direction.

Due to the limited number of electrons in each frame, the average projected momentum, $\langle p_x \rangle$ of the residual-gas-only frames shows a relatively wide distribution. A significant number of frames above the red line (70 electrons) contain larger amount of electrons and an asymmetric distribution due to the photoemission from nanoparticles. The frames with hit numbers in between the blue and red lines barely contain electrons from nanoparticles and are disregarded. The discussed features of the nanoparticle frames, i.e. the combination of the number of electrons and an asymmetric distribution, provide an efficient discrimination method for the post-selection of residual-gas-only and nanoparticle frames. The shot-averaged images following this approach are shown in Figs. 4.2(c,d). The residual gas

momentum distribution is symmetric with respect to the laser propagation direction (Fig. 4.2(d)), while the nanoparticle emission clearly has an asymmetric distribution due to the XUV shadowing, see Fig. 4.2(c).

4.3 Nanoparticle streaking spectrograms

By measuring momentum images for different pulse delays of the NIR with respect to the XUV pulse, streaking spectrograms can be obtained. In the measurements on 50 nm SiO_2 particles, the pulse delay step size was set to 150 as, and 40000 laser shots were recorded at each delay step. The spectrograms depicted in Fig. 4.3 were derived from angular integration of the projected momentum distributions over an angular range of $\pm 25^\circ$ around the laser polarization direction (see Fig. 4.2(c) and (d)). We note here that the VMI images were not inverted and the spectrogram was directly obtained from converting the projected radial momenta to energies. This needs to be taken into account when comparing the data to theoretical simulations. Figure 4.3 shows streaking spectrograms for (a) residual gas and (b) nanoparticles, obtained from the discriminated single-shot data. Both spectrograms look very similar and exhibit the characteristic oscillations with respect to the pulse delays. Two contour lines for a selected asymptotic energy (25 eV) are shown as solid cyan lines.

To determine relative streaking delays between the nanoparticle and residual-gas data, we fit contour lines in the streaking spectrograms. Furthermore, each contour line was filtered to remove high frequency noise (circles in Figs. 4.4(a,b)) by employing a low-pass filter. The filtered contour lines were then fit with a few-cycle waveform of the following form:

$$E_{\mathrm{fit}}(\Delta t) = E + A\cos(\omega\Delta t - \omega\delta t)\exp(-\frac{1}{2}\frac{(\Delta t - t_0)^2}{\tau^2}), \tag{4.8}$$

where E is the asymptotic energy of the considered contour line, A is the streaking amplitude, ω is the carrier angular frequency, δt is the streaking delay, t_0 is the center of the Gaussian envelope, and τ is the pulse width. The solid lines in Figs. 4.4(a,b) show the fitting results corresponding to the filtered contour lines in Figs. 4.3(a,b), respectively. Both curves provide a very good representation of the data and reveal a relative time shift between the curves from the residual gas and SiO_2 nanoparticle. Meanwhile, an effective electric field amplitude of the streaking NIR laser pulse can be reconstructed from the fitted curve for the residual gas. The maximum electric field is $E_{\mathrm{y}} = 2.6 \times 10^9\,\mathrm{V\,m^{-1}}$, corresponding to an instantaneous intensity of $9.0 \times 10^{11}\,\mathrm{W\,cm^{-2}}$.

The energy-dependent temporal streaking delays $\delta \mathrm{t}_{\mathrm{gas}}$ for the residual gas and $\delta \mathrm{t}_{\mathrm{SiO_2}}$ for SiO_2 nanoparticles are shown with blue and red dots in Fig. 4.4(c). Both of the curves exhibit a characteristic tilt originating from the chirp of the XUV pulses, which can be fully taken into account in theoretical simulations.

In the single-shot attosecond streaking experiments, the simultaneous measurement of the residual gas and nanoparticles within the same experiment offers retrieving the energy-dependent relative streaking delay $\delta t_{\mathrm{rel}} = \delta t_{\mathrm{SiO_2}} - \delta t_{\mathrm{gas}}$, which reveals a photoemission time shift between the gas reference and nanoparticles.

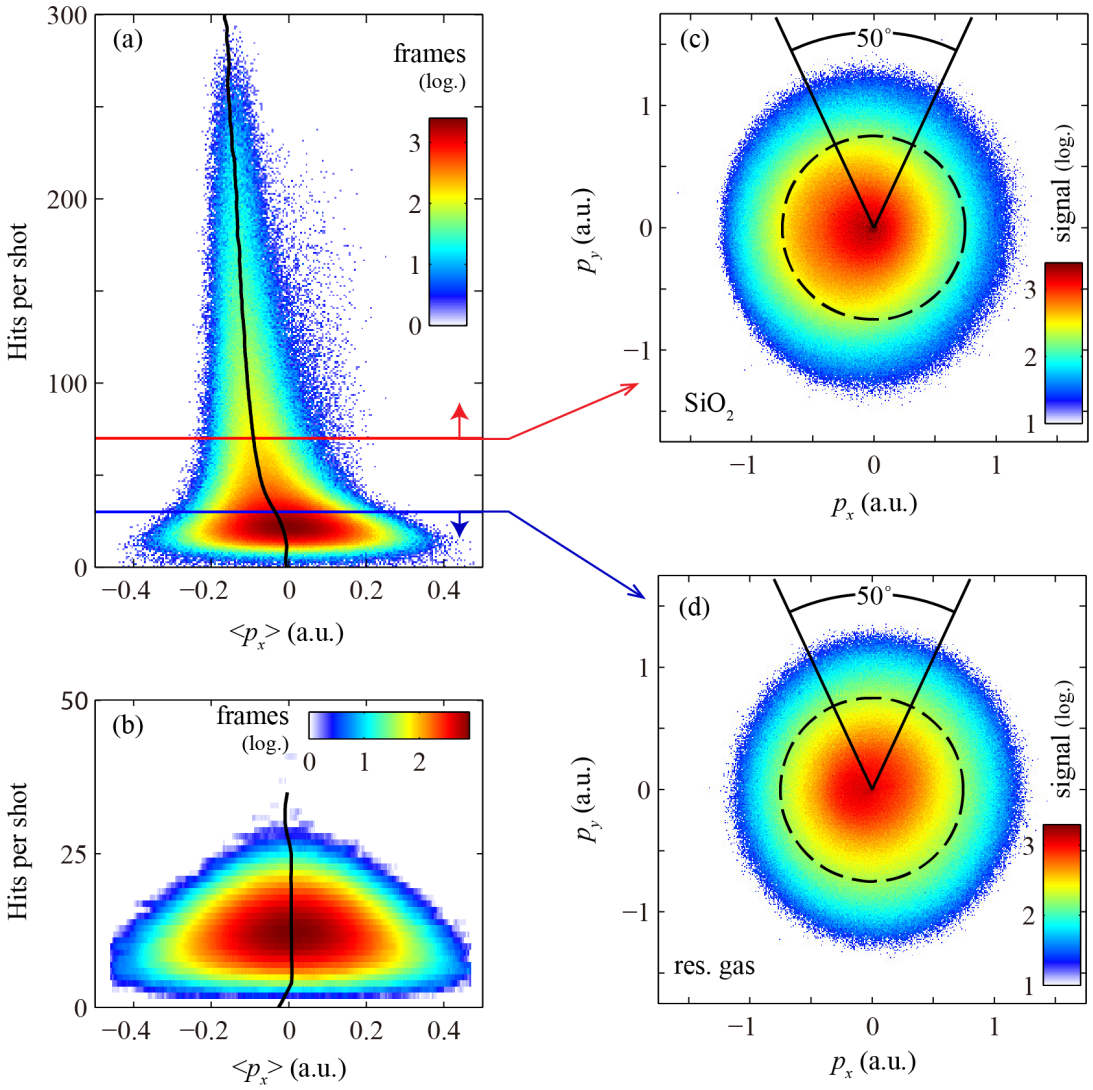

Figure 4.2: Single frame distributions as a function of $\langle p_x \rangle$ (average projected momentum on the x-axis) and the number of electrons per frame for measurements with (a) SiO_2 nanoparticles and (b) without nanoparticles, corresponding to just residual gas. The color scale corresponds to the number of frames on a logarithmic scale. The black solid line indicates the weighted average of $\langle p_x \rangle$. The blue and red solid lines denote regions for nanoparticle and residual-gas-only frames. (c), (d) Images obtained by superposition of nanoparticle frames (above the red line in (a)) and residual-gas-only frames (below the blue line in (a)). The black dashed line indicates the cutoff momentum of background contribution. The black lines mark the integration range used for retrieving streaking traces. Taken from [114].

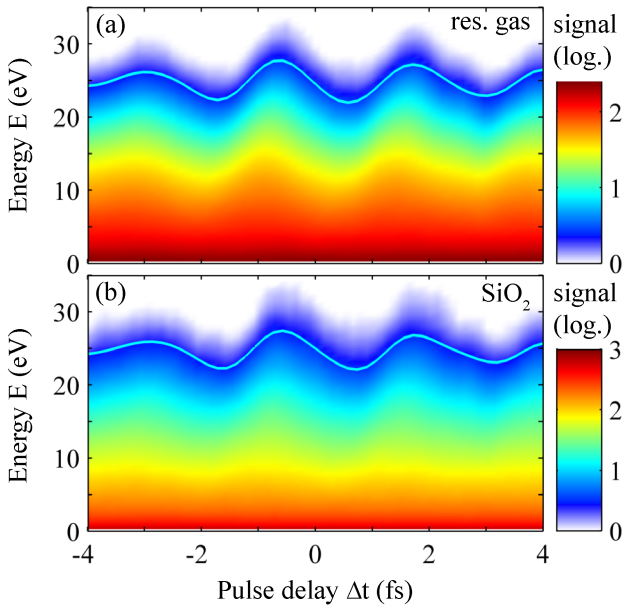

Figure 4.3: Typical streaking spectrograms of electrons emitted from residual gas (a) and nanoparticles (b) obtained from angular integration of projected momentum maps over $\pm 25°$ around the laser polarization direction. The solid curves indicate the filtered contour line following constant signal intensity for an asymptotic energy of 25 eV. Taken from [114].

In the data discrimination, we accounted for the fact that the recorded events in nanoparticle frames also contain contributions from the residual gas. In order to calculate the time delay of the photoelectrons from the nanoparticles, it is crucial to uncover the ratio between these two contributions. For this purpose, we compared the averaged single-frame spectra from Figs. 4.2(d,c), which correspond to the residual gas and nanoparticle frames, respectively. Figure 4.4(c) shows the resulting spectrum from residual gas (blue line) and the spectrum obtained from the nanoparticle frames (red line). The black line shows the nanoparticle single frame spectrum after subtracting the gas contribution, reflecting the pure nanoparticle signal. The nanoparticle spectrum has a higher intensity and higher spectral cutoff than the residual gas data. The ratio between the nanoparticle and residual gas signal as function of energy is shown in Fig. 4.5(b). The contribution of photoelectrons from the SiO_2 nanoparticles increases above 20 eV, and dominates the signal beyond the cutoff energy of the residual gas. Limited by a too strong overlap between the residual gas and nanoparticle signals below 20 eV and the signal-to-noise ratio of the streaking spectra near the cutoff energies (see Fig. 4.3), the relative streaking delay between SiO_2 and the reference gas can be extracted in the window between 20 and 30 eV. We note that this particular energy window was accessible with the XUV pulses generated in Kr as described in section 3.6.

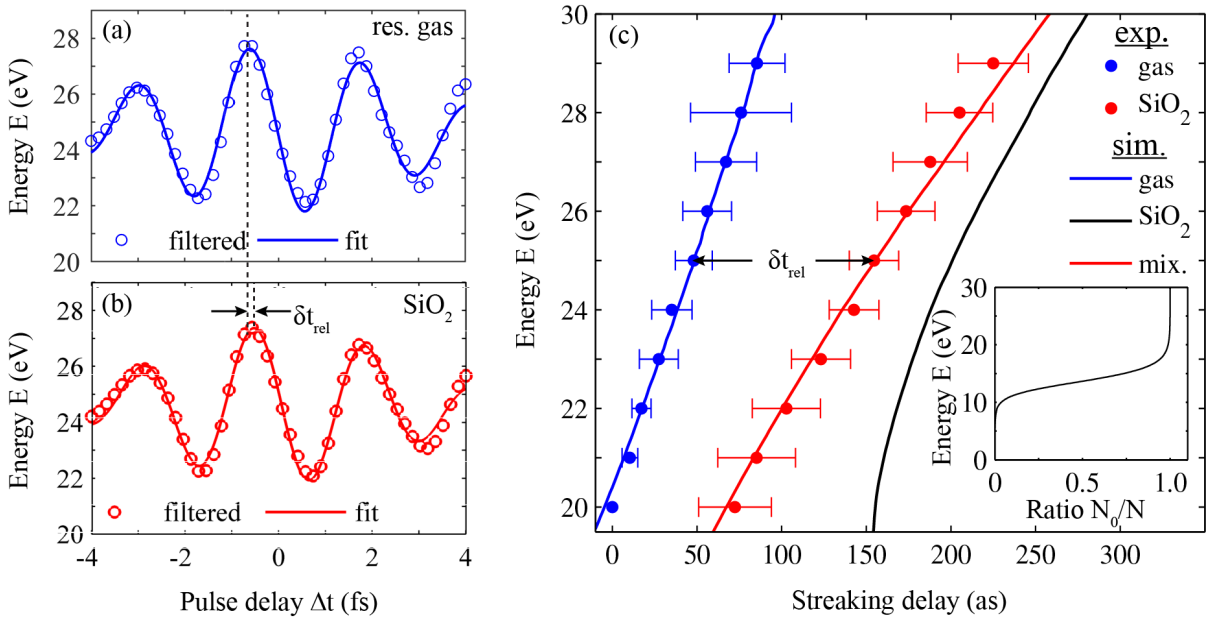

Figure 4.4: (a, b) The high frequency-filtered contour lines (circles) were fitted with few-cycle waveforms (solid lines). (c) Energy-dependent streaking delays measured for residual gas (blue) and SiO_2 nanoparticles (red). The data represents an average over three scans performed under similar conditions (the error bars indicate the deviation of the individual data sets). Solid lines show corresponding simulation results for gas (blue), nanoparticles (black) and their mixture (red) using an XUV chirp of $-7 \times 10^{-3}\,\mathrm{fs}^2$. The inset shows the relative contribution of electrons without inelastic collisions in the M^{3}C simulations. Taken from [114].

4.4 Photoemission delays from nanoparticles

To unravel the physics resulting in the delayed photoemission from the dielectric nanoparticles, semi-classical trajectory simulations based on the M^{3}C model were employed (details in section 2.4). In these simulations, the propagation of the XUV and NIR pulses was evaluated using a spectral decomposition of the incident fields and calculating the spatial modes for the individual spectral components using the Mie-solutions for a sphere including dispersion. Photoelectron trajectories were launched in the sphere via Monte-Carlo sampling of the local instantaneous spectral photoionization rate (calculated from the local XUV near-field) and integrated in the NIR near-field using classical equations of motion. For trajectories inside the sphere, elastic electron-atom and inelastic electron-electron collisions were included as instantaneous, isotropic scattering events using energy-dependent mean-free paths and sampled with Monte-Carlo methods. As ionization due to the XUV field was weak in the investigated scenario, charge interaction effects could be neglected.

From M^{3}C simulations for the experimental parameters, we calculated streaking spec-

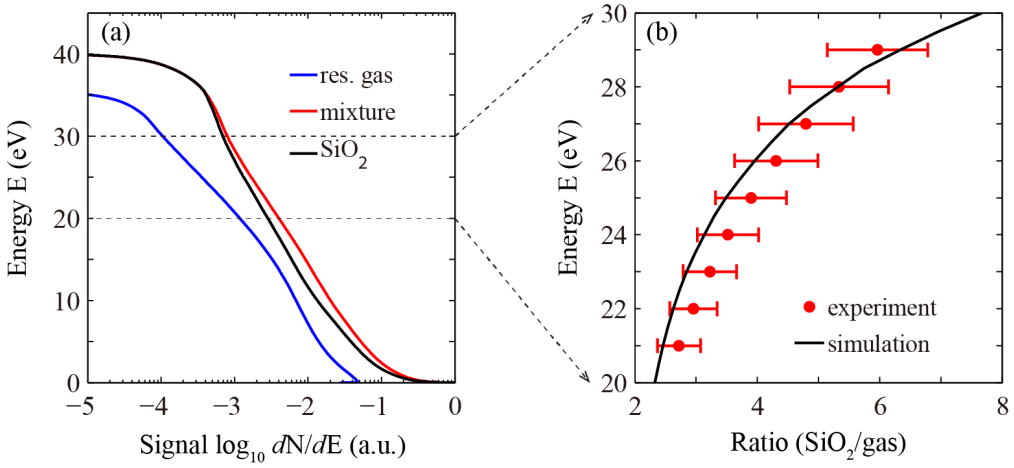

Figure 4.5: (a) Typical single-frame energy spectra of emitted electrons from residual gas (blue), from a mixture of SiO_2 and residual gas (red), and SiO_2 excluding residual gas (black). (b) Measured energy-dependent ratio of nanoparticle signal relative to residual gas (red) and result obtained from combining simulated gas and nanoparticle spectrograms (black). The error bars indicate the deviation of three independent measurements. Taken from [114].

trograms and extracted energy-dependent streaking delays using the same projections and analysis as for the experimental data. The excellent agreement of simulations and experiment (compare curves and dots in Fig. 4.4(c)) motivated a systematic analysis of the contributions to the streaking delays. We found that in our scenario the streaking delay for the SiO_2 nanoparticles

$$\delta t_{\mathrm{SiO_2}} = \delta t_{\mathrm{offset}} + \delta t_{\mathrm{chirp}} + \delta t_{\mathrm{fields}} + \delta t_{\mathrm{coll}} \tag{4.9}$$

includes the following four contributions. First, a delay induced by the (experimentally unknown) absolute offset of the XUV/NIR delay axis as well as the CEP of the NIR pulse ($\delta t_{\mathrm{offset}}$). Second, an energy-dependent delay generated by the chirp of the attosecond pulse ($\delta t_{\mathrm{chirp}}$). Third, a delay induced by the retardation and spatial inhomogeneity of the local near-fields ($\delta t_{\mathrm{fields}}$, details below) and fourth, a delay induced by the electron collisions inside the medium (δt_{coll}).

The first two contributions also define the delay of the reference measurement

$$\delta t_{\mathrm{gas}} = \delta t_{\mathrm{offset}} + \delta t_{\mathrm{chirp}}. \tag{4.10}$$

As the nanoparticle and reference measurements are performed simultaneously for the same laser parameters, $\delta t_{\mathrm{offset}}$ and $\delta t_{\mathrm{chirp}}$ are equal for nanoparticle and gas reference (assuming a similar effect of the XUV chirp on the gas and nanoparticle streaking) and thus canceled out in the relative streaking delay. The relative streaking delay

$$\delta t_{\mathrm{rel}} = \delta t_{\mathrm{SiO_2}} - \delta t_{\mathrm{gas}} = \delta t_{\mathrm{fields}} + \delta t_{\mathrm{coll}} \tag{4.11}$$

is fully determined by the field- and collision-induced contributions. The field contributions are relevant for nanoscopic targets such as the nanoparticles discussed here, but do not play a role in the photoemission from atoms. Note that additional contributions due to Wigner delays [143] and Coulomb-laser coupling [144–146] are assumed to be comparable for nanoparticles and gas as we evaluate similar electron energies and the long-range interactions are Coulombic in both cases. These contributions thus cancel in the relative delay. The remaining short-range effects are assumed negligible away from resonances [147].

In the following we present a detailed analysis of the collision induced and the near-field induced streaking delays. Furthermore, we discuss the XUV chirp effect for gas and nanoparticles.

4.4.1 Near-field induced streaking delay

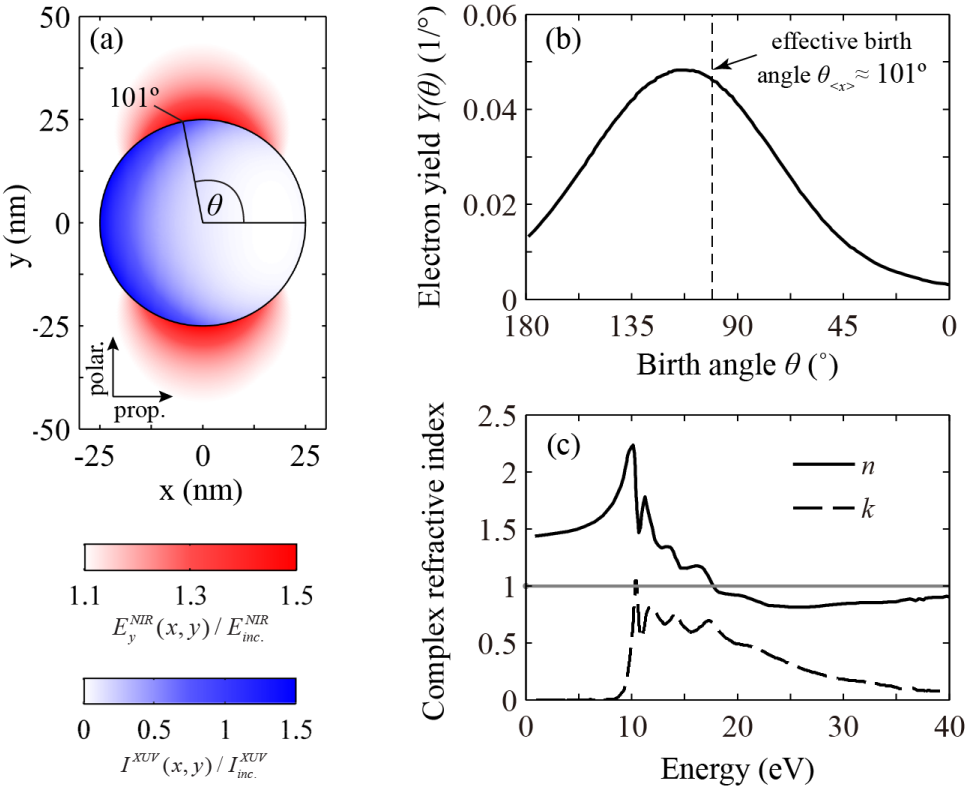

Figure 4.6: (a) Near-field enhancement of the XUV (blue) and NIR (red) on a cut through the propagation-polarization plane of a 50 nm SiO_2 sphere. (b) Distribution of emitted electrons, $Y(\theta)$, as a function of birth angle θ. The vertical dashed line indicates an effective birth angle $\theta_{\langle x\rangle} = \mathrm{acos}(\langle\cos\theta\rangle)$. Adapted from [114]. (c) Energy dependent complex refractive index for SiO_2, adapted from [119].

In order to extract information on the electron scattering within the material the field-

induced contribution to the relative streaking delay must be either negligible or known. In the following we describe how this contribution can be estimated for 50 nm silica spheres. We split the field-induced delay

$$\delta t_{\text{field}} = \delta t_{\text{retard.}} + \delta t_{\text{inhom.}} \tag{4.12}$$

into the parts corresponding to retardation of the XUV and NIR fields ($\delta t_{\text{retard.}}$) and the part reflecting the effect of the spatial inhomogeneities of the NIR field ($\delta t_{\text{inhom.}}$), i.e. its decay with increasing distance from the nanosphere.

The retardation effect can be estimated by comparing the evolution of the local near-fields at the sphere surface with respective vacuum solutions. Figure 4.6(a) shows the relative spatial intensity and field enhancement profiles of the XUV field (inside region, blue) and the NIR field (outside region, red), respectively, for a 50 nm SiO_2 sphere. The specific regions are selected for the following reasons. The XUV field enters the dynamics only via photoionization inside of the sphere. The NIR streaking field is nearly constant inside and has the relevant spatial variations outside. For nanospheres that are small in comparison to the wavelength of the NIR field, the peak enhancement appears at the particle poles (compare [48]), leading to the strongest streaking of electrons from these regions. For the XUV field, there is nearly no intensity enhancement as the real part of the complex permittivity of SiO_2 around 30 eV is close to unity, see Fig. 4.6(c). However, the non-negligible imaginary part leads to strong absorption of the XUV field on the front side of the nanosphere, which results in lower field intensities at the back side. This field shadowing is seen in the asymmetric electron emission that is used for tagging nanoparticle shots in the experiment. The birth angle distribution for a typical simulation (such as that seen in Fig. 4.6(b)) clearly reflects a significant shift of the peak signal toward the front side of ca. 10° with respect to the particle pole.

The XUV field enters the dynamics only via photoionization, which is determined by the pulse envelope. Therefore, we evaluate the group delay

$$t_{\text{group,XUV}} = t^{\text{SiO}_2}_{\text{group,XUV}} - t^{\text{vac}}_{\text{group,XUV}}, \tag{4.13}$$

defined via the center of mass of the field envelope (blue curve in Fig. 4.7(a)), where a negative/positive delay indicates advanced/retarded arrival of the near-field with respect to the vacuum case. For the NIR field, where the full waveform enters the dynamics, we estimate the retardation effect via the phase delay

$$t_{\text{phase,NIR}} = t^{\text{SiO}_2}_{\text{phase,NIR}} - t^{\text{vac}}_{\text{phase,NIR}} \tag{4.14}$$

(red curve in Fig. 4.7(a)). The overall retardation induced streaking delay then reads

$$\delta t_{\text{retard.}} = t_{\text{group,XUV}} - t_{\text{phase,NIR}}, \tag{4.15}$$

where the XUV/NIR parts contribute with positive/negative sign as the incident NIR-field needs to be delayed/advanced to compensate for the respective retardation effect. We found that the retardation induced delay (black curve in Fig. 4.7(b)) is smaller than 40 as over

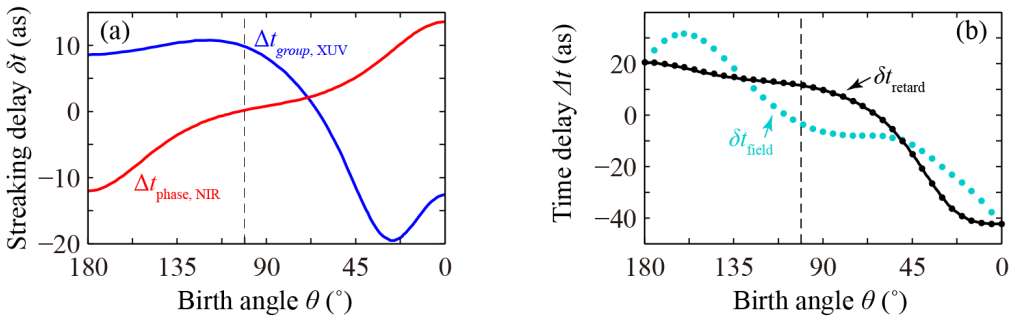

Figure 4.7: (a) Angle-dependent NIR phase- and XUV group-delay with respect to the vacuum solutions calculated at the sphere surface in the propagation-polarization-plane. (b) Streaking-delay due to field retardation of XUV and NIR fields calculated from the group and phase delays in (a) (black curve). Symbols show streaking delays evaluated from a simplified trajectory model including only field retardation (black), and including both field retardation and NIR field inhomogeneity (cyan). Adapted from [114].

the whole surface of the sphere. However, due to the shadowing of the XUV radiation, the dominant part of the detected photoelectrons is emitted from the front side of the sphere (see Fig. 4.2(c)). In particular, at the effective birth angle $\theta_{\langle x \rangle} \approx 101°$ (see dashed vertical line in Fig. 4.6(b) and Fig. 4.7), the retardation induced delay is particularly small ($<$ 15 as).

4.4.2 Effect of the chirp on the streaking delay

For the XUV pulses in the M^{3}C simulations we assume an incident pulse with Gaussian spectral intensity distribution to approximate the experimentally measured spectrum (compare blue and black curves in Fig. 4.8(a)). The combined spectral and temporal evolution of the XUV intensity is characterized by the Wigner distribution. Figure 4.8(b-c) show the resulting Wigner distributions $W(r, t, \omega)$ for a 250 as XUV pulse with two different chirp parameters (as indicated) at the upper pole of an SiO_2 sphere. While for an unchirped pulse all frequency components arrive nearly simultaneously (Fig. 4.8(b)) a negative chirp leads to an arrival delay of the XUV pulse that increases with photon energy (Fig. 4.8(c)). We quantify this spectral delay $t_{\mathrm{XUV}}(E_{\mathrm{ph}})$ by the corresponding temporal center of mass of the Wigner distribution, see Fig. 4.8(b-c). The relative arrival delay $t_{\mathrm{rel,\,XUV}}(E_{\mathrm{ph}}) = t_{\mathrm{SiO2,XUV}}(E_{\mathrm{ph}}) - t_{\mathrm{vac,XUV}}(E_{\mathrm{ph}})$ between nanoparticle and vacuum fields (see Fig. 4.8(d)) shows dispersion induced spectral variations by just a few attoseconds around the average XUV group delay. Most importantly, the relative arrival delay is nearly independent of the XUV chirp (compare solid and dashed curves in Fig. 4.8(d)), supporting the above claim that the chirp effect also cancels in the relative streaking delay analysis.

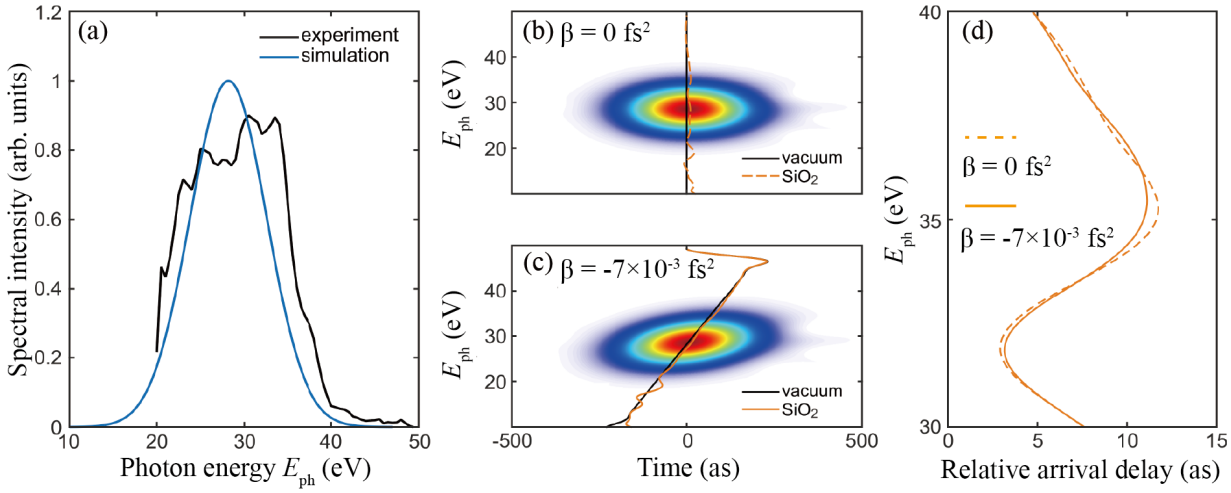

Figure 4.8: (a) XUV spectrum measured in the experiment (black) and Gaussian spectrum used in the simulations (blue). (b - c) Wigner distributions at the surface of a 50 nm SiO_2 sphere at the upper pole (90°) as a function of time and photon energy for two different chirp parameters β (as indicated). The lines reflect the spectral arrival delays for vacuum and SiO_2 . (d) Relative spectral arrival delays resulting from the data in (b) and (c).

4.4.3 Size dependence of the angle-averaged streaking delay

For a systematic comparison of the different field-induced contributions to the streaking delay, we calculated angle-averaged streaking delays in dependence of the nanosphere diameter, see Fig. 4.9(b). The mean birth angles for the investigated sphere diameters, obtained from M^3C simulations, are shown in Fig. 4.9(a). The oscillation of the field retardation induced streaking delay as function of sphere diameter (black curve and dots in Fig. 4.9(b)) is attributed to the successive excitation of higher order modes of the NIR near-field. The offset of the streaking delay of around 10 as in the limit of small spheres is a pure dispersion induced feature of the XUV near field and not a propagation effect. The additional effect of the NIR inhomogeneity (compare green to black dots in Fig. 4.9(b)) is negligible for large spheres but strongly modifies the field induced streaking delay for small spheres. In particular, for $d = 50$ nm the inhomogeneity effect cancels the retardation effect $\overline{\delta t} < 2.5$ as such that field-induced delays are negligible ($\delta t_{\text{fields}} \ll \delta t_{\text{coll}}$), making the relative streaking delay to a direct measure of the collisional delay ($\delta t_{\text{rel}} \approx \delta t_{\text{coll}}$).

4.4.4 Influence of elastic and inelastic collisions on the streaking delay

Since the contribution δt_{fields}, characterizing the retardation and inhomogeneity effects of the NIR and XUV near fields, is negligible, the main contribution to the relative streaking delay results from the interplay of elastic and inelastic collisions inside the spheres and

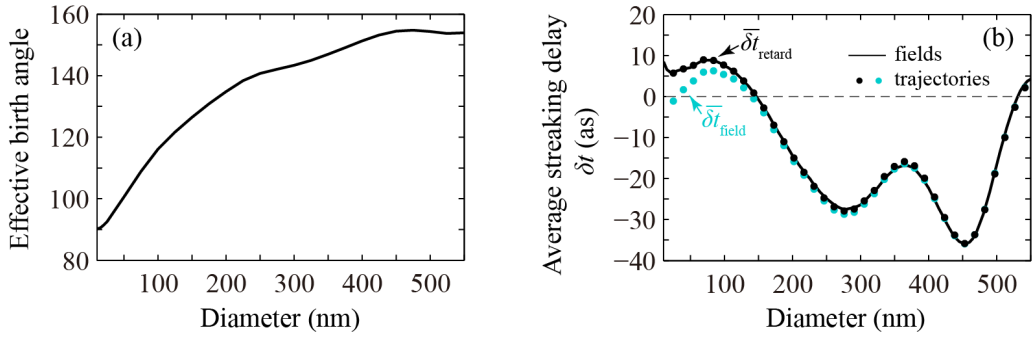

Figure 4.9: (a) Evolution of the effective birth angle with the nanoparticle diameter. (b) Size-dependence of the angle-averaged streaking delay $\overline{\delta t} = \frac{\int Y(\theta)\delta t(\theta)\mathrm{d}\theta}{\int S(\theta)\mathrm{d}\theta}$ (weighted with the birth angle distribution) calculated from the near-fields (curve) and from the simplified trajectories model (dots) as in Fig. 4.7(b). Adapted from [114].

is in the range $\delta t_{\text{coll}} \approx 150$ as for our experimental parameters. Below we show why this delay is mainly dependent on the inelastic scattering time for dielectric materials.

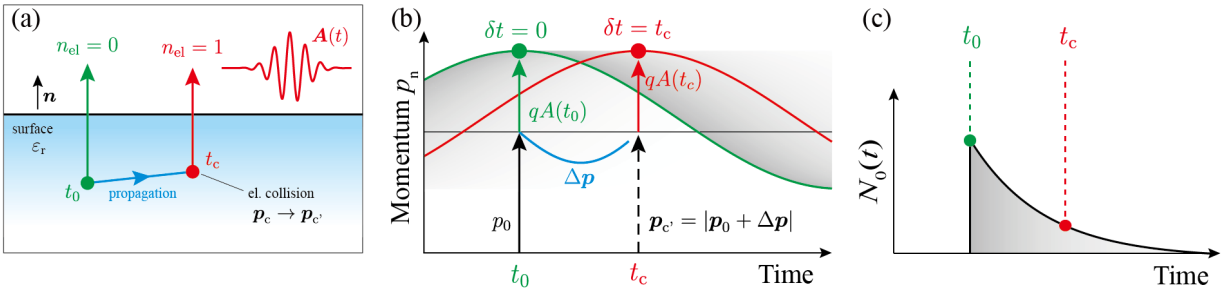

Figure 4.10: Impact of elastic and inelastic scattering on the streaking delays. (a) The photoemission of electrons generated at time t_0 with initial momentum p_0 without collisions (green) and with an elastic collision (red) at time t_{c} after propagation inside the material (blue arrow). $\mathbf{A}(t)$ is the vector potential of the probe laser field. (b) The streaking traces result from directly emitted electrons (green curve) and elastically scattered electrons (red curve). (c) Population of electrons without inelastic collisions leading to time-shifted contributions to the final streaking spectrogram. Taken from [42].

In the relevant energy range, interband excitations constitute the dominant inelastic scattering channel and result in an energy loss comparable to the bandgap energy for ($\approx$ 9 eV for SiO_2), removing the inelastically scattered electrons from the spectral region of interest, that is, the high-energy part of the streaking trace. Therefore, we focus on electrons without inelastic collisions, which determine the high-energy signals. For clarity, we discuss the effect for a fully transparent material (unit permittivity). Figure 4.10

illustrates the photoemission of electrons generated at time t_0 with initial momentum p_0 from the transparent material without collisions (green) and following an elastic collision (red) at time t_c after propagation inside the material (blue arrow). The direct electrons escape along the surface normal (green arrow) and have a final momentum $\mathbf{p}_f = \mathbf{p}_0 + q\mathbf{A}(t_0)$, where q is the electron charge, $\mathbf{A}(t)$ is the vector potential of the probe laser field. The streaking trace that results from these directly emitted electrons (green curve in Fig. 4.10(b)) characterizes the streaking field vector potential, and is thus equivalent to gas-only traces.

In contrast, electrons that leave after elastic, isotropic scattering at time t_c (red symbol in Fig. 4.10(a)) are essentially indistinguishable from direct electrons generated at time t_c. The electron momentum gain during propagation inside the medium between the birth at time t_0 and the elastic collision at time t_c nearly vanishes after averaging over an ensemble of electrons. This occurs because electrons born with point-symmetric (we assume an isotropic distribution in Fig. 4.11 for clarity) initial momentum distribution with momentum vectors $\boldsymbol{p}_0$ (black arrows in Fig. 4.11(a)) gain a fixed momentum $\Delta\boldsymbol{p}$ defined by the vector potential difference $\Delta\boldsymbol{p} = q\left[\mathbf{A}\left(t_0\right) - \mathbf{A}\left(t_c\right)\right]$ (blue arrows in Fig. 4.11(a)). Assuming isotropic elastic scattering at time t_c, only the modulus of the incident momentum $|\boldsymbol{p}_0 + \Delta\boldsymbol{p}|$ determines the momentum after the collision. Transformation into the initial momentum frame (Fig. 4.11(b)) leads to a point-symmetric (or isotropic) distribution of gained momenta. Under this assumption that is well justified for the considered laser parameters, the average momentum for an ensemble of electrons is $\langle|\boldsymbol{p}_0 + \Delta\boldsymbol{p}|\rangle \approx |\boldsymbol{p}_0|$. Therefore, besides a broadening of the momentum distribution (Fig. 4.11(c)), the isotropic scattering event effectively acts as a new birth of the electron with final elastic scattering time t_c has an average final momentum $\langle\mathbf{p}_f\rangle \approx \mathbf{p}_0 + q\mathbf{A}(t_c)$, yielding a streaking trace shifted by t_c (red curve in Fig. 4.10(b)). The final spectrogram is an average of shifted streaking traces, each weighted with the corresponding emission current. As the emission current reflects the population decay resulting from interband excitations, the streaking delay is very sensitive to the inelastic scattering time (Fig. 4.10(c)).

Each elastic collision induces a shift of the streaking spectrogram, while inelastic collisions result in a decay of the population of electrons contributing to the relevant electron energy range. The effect of these two processes on a typical, calculated streaking trace is demonstrated in Fig. 4.12(a-d) via selective streaking spectrograms, calculated for electrons escaping without inelastic collisions and for different numbers of elastic collisions. With increasing numbers of elastic collisions, the streaking delay (averaged in the energy range between 25 and 30 eV and shown as vertical, solid black lines in Fig. 4.12(a-d)) increases linearly with the number of collisions (Fig. 4.12(f)) while the signal strength decreases exponentially (Fig. 4.12(e)) due to the population loss resulting from inelastic collisions. Note that the streaking delay extracted from the sum spectrogram is 135 as (red arrow in Fig. 4.12(f)) and thus slightly smaller than the expected value of 162 as sampled at the $1/e$ decay time (black arrow). This difference (~ 25 as) is attributed to the intercycle averaging of the streaking traces and the resulting blurring of the streaking features in the accumulated spectrogram.

M^{3}C simulations with varying scattering parameters reveal the quantitative effects of

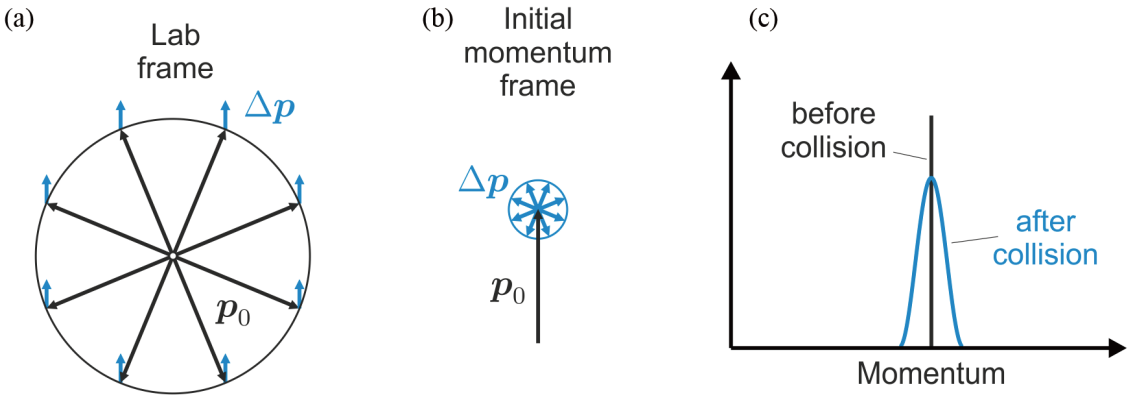

Figure 4.11: (a, b) Isotropic initial momenta $\boldsymbol{p}_0$ (black arrows) and laser-field-aligned momentum gain $\Delta\boldsymbol{p}_0$ (blue arrows) in (a) the lab frame and (b) the initial momentum frame. (c) Schematic representation of the momentum distribution before (black peak) and after (blue curve) an elastic collision.

elastic and inelastic scattering on the relative streaking delays (Fig. 4.13(a)), namely a weak dependence on the elastic scattering time, and a strong dependence on the inelastic scattering time. The impact of the material's permittivity at the streaking field wavelength is shown in Fig. 4.13(b). Irrespective of the permittivity, represented by the field attenuation factor $\alpha = 1/\varepsilon_\mathrm{r}$, the streaking delay increases with inelastic scattering time. However, in both the transparent ($\alpha \to 1$) and the metal ($\alpha \to 0$) limits, the delays remain strongly influenced by the elastic scattering time. With increasing elastic scattering time, delays decrease toward the transparent limit but increase toward the metallic limit. These opposing trends reflect the effect of the internal field attenuation and, most importantly, almost vanish for $\alpha \approx 0.3$. The identification of this cancellation is one of the major results of our analysis as it enables the direct retrieval of inelastic scattering times for a range of dielectric materials. The streaking delay's high sensitivity to the inelastic collision time justifies its extraction from the full M^{3}C simulations, which match the experimental data in Fig. 4.5(b) using a scaled Lotz cross-section. We find $\tau_\mathrm{inel} \sim 370$ as at 25 eV in SiO_2 .

Figure 4.14 shows comparison of the resulting electron IMFP in SiO_2 obtained here between 20 and 30 eV with results found in the literature [15, 148–150]. Note that best agreement is found with the work reported in ref. [148], where the authors state that their data in the range of 10–40 eV are unreliable and serve only as a trend. With IMFPs obtained via the demonstrated approach the predictive capability of theoretical models for scattering in dielectrics can now be thoroughly tested.

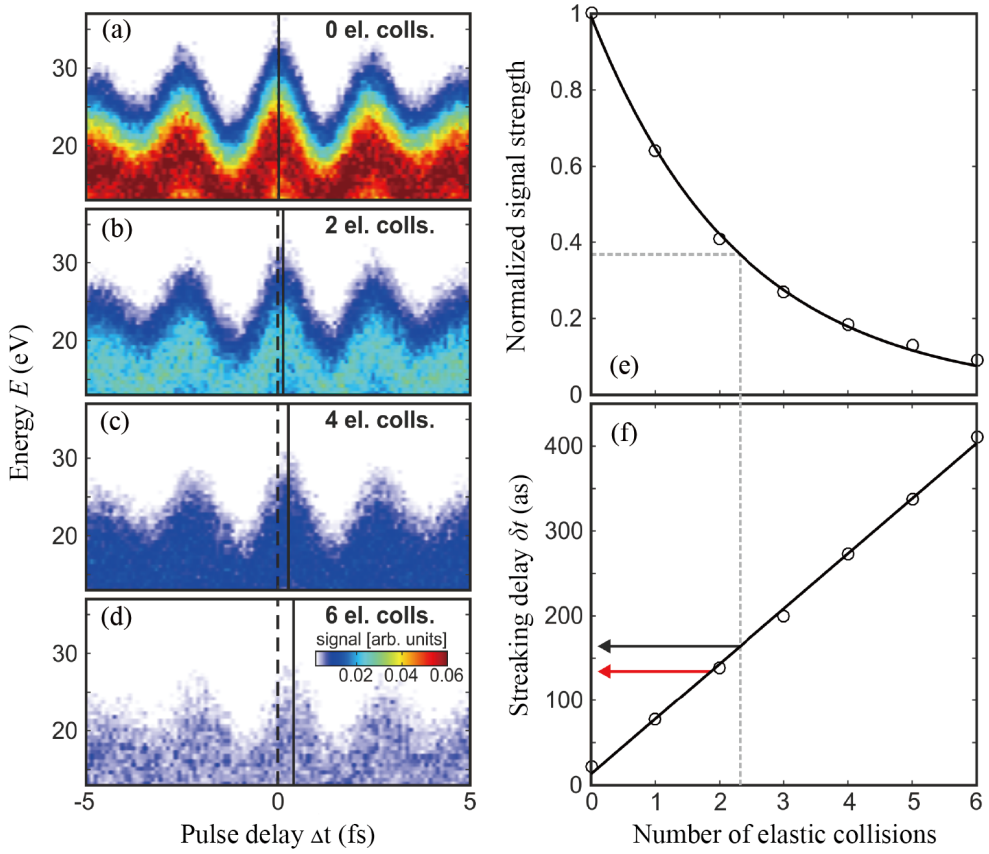

Figure 4.12: (a-d) Simulated selective streaking traces for electrons without inelastic collisions and with different numbers of elastic collisions (as indicated) assuming unchirped XUV (250 as, 28 eV) and NIR (5 fs, 720 nm) pulses. The solid black lines indicate the extracted streaking delays. (e) Decay of the signal intensity (black circles, determined as the sum over each individual streaking trace) due to inelastic collisions as function of elastic collisions. The vertical dashed line indicates the number of elastic collisions (~ 2.3) for which the signal has decayed to a fraction $1/e$. (f) Streaking delays extracted from collision-resolved spectrograms vs. number of elastic collisions (black circles). For the average number of elastic collisions from (e) the streaking delay is 162 as (black arrow). The red arrow shows the streaking delay of 135 as extracted from the full spectrum (including all numbers of elastic collisions; not shown). Solid black lines in (e) and (f) are guides to the eye.

4.5 Conclusions

We have shown that attosecond streaking metrology is a powerful tool for real-time photoemission measurements on isolated nanotargets, and can reveal new insight into e.g. electron scattering. In cases, where solids suffer from accumulative charging, nanoparticle beams

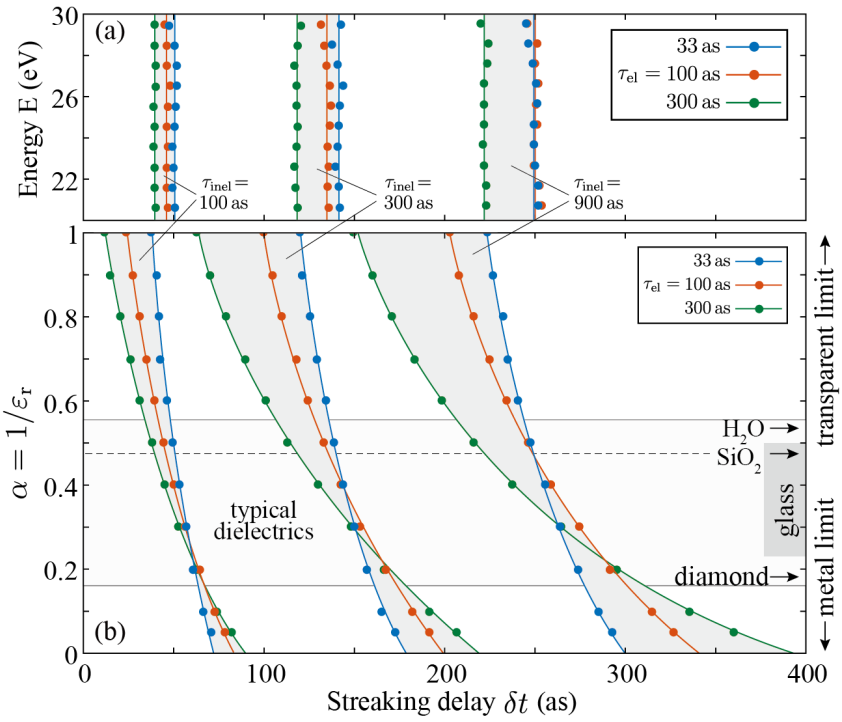

Figure 4.13: (a) Streaking delays for 50 nm SiO_2 nanoparticles calculated from M^3C for varying elastic and inelastic scattering times (as indicated). (b) The streaking delays as a function of the solids' permittivity at 720 nm, expressed by the field attenuation factor $\alpha = 1/\varepsilon_r$. Adapted from [42].

provide a solution as a refreshable target. Most importantly, the collective and/or nonlinear dynamics in nanoparticles, such as e.g. localized plasmons [23–25, 151] and plasma waves [152], rapid inner and outer ionization [153], and electron density fluctuations created by e.g. shock waves [154] are interesting phenomena that await their exploration with sub-femtosecond precision. We expect the outlined approaches for the implementation of attosecond streaking in nanoparticles to contribute to further advances in these directions.

Our joint experimental and theoretical work uncovers the physics encoded in attosecond streaking on dielectrics and resolves the characterization problem of inelastic scattering in these materials. Attosecond streaking in dielectrics differs from metals where the NIR streaking field takes effect only on the surface of the material. The presence of the field inside the dielectric determines the importance of elastic and inelastic scattering on the streaking delay. We found that for most dielectric materials the streaking delay is largely independent of the elastic scattering time thus enabling the characterization of inelastic scattering. The accessible energy range depends only on the photon energy of the attosecond pulse, which even currently covers tens of electronvolts to kiloelectronvolts and might be further extended in the future. Our approach permits characterization of inelastic scat-

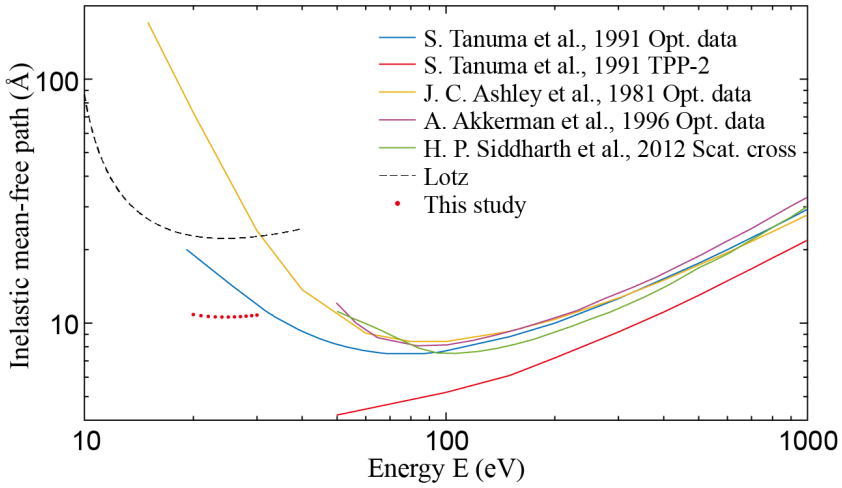

Figure 4.14: Energy-dependent IMFPs obtained in previous work [15, 148–150]. IMFP from quantitative simulations of our experimental data using a scaled Lotz formula for the energy range 20–30 eV (red dots). Adapted from [42].

tering in a wide range of dielectric solids and liquids, including amorphous dielectrics such as water, which could be inserted in the form of droplets or as a thin jet. Direct access to IMFPs in dielectrics for a wide range of energies including the otherwise inaccessible range below 50 eV holds promise for improving our understanding of radiation damage.

Chapter 5

All-optical spatio-temporal control of electron emission from SiO_2 nanospheres with femtosecond two-color laser fields [1]

5.1 Introduction

In case of nanostructured materials explored by ultrafast intense laser pulses, the spatial variation of the strongly localized optical near-field provides an additional control parameter for both electron emission and acceleration [42, 48, 114, 156]. The coherent control of electron emission and acceleration with carrier-envelope phase (CEP)-controlled few-cycle laser pulses has been investigated for isolated nanospheres [48, 66–68], metal nanotips [69, 71], and surface assembled nanostructures [157–159]. Characteristic nanoscale phenomena that contribute to the strong-field photoemission from these materials include (i) the transition from ponderomotive to sub-cycle electron acceleration for field localization below the scale of the electron quiver motion [70], and (ii) field propagation induced directionality of the energetic electron emission as demonstrated for nanospheres with diameters approaching the wavelength of the incident light [48].

In this chapter, we extend the near-field control of the photoemission from nanospheres to the multi-color regime. The realization and exploration of unprecedented all-optical spatio-temporal control of the electron emission direction by tailored nanolocalized fields using phase-controlled two-color laser fields will be presented. It will be demonstrated how tailoring of the temporal waveform of the incident two-color field via its relative phase and intensity ratio translates into modifications of the angular distributions of the yield and maximal electron energy of electrons. To identify the mechanism behind the all-optical control of the electron emission from nanospheres, 3-dimensional semi-classical trajectory simulations based on the Simple-Man's Model [106] will be presented and discussed.

[1] The main results in this Chapter were published in [155].

5.2 Mie parameter dependent field enhancement

The waveform of a combined two-color driving field may be expressed as

$$E(t) = E_\omega(t)\,[\cos(\omega t) + \sqrt{\eta}\cos(2\omega t + \varphi_r)]$$

and depends on the relative phase φ_r, and the intensity ratio $\eta = I_{2\omega}/I_\omega$. The linear response of a nanosphere to laser light can be accurately described by the Mie solution of Maxwell's equations. For a sphere with diameter d subjected to an incident field with wavelength λ, the impact of propagation effects on the near-field distribution can be characterized by the dimensionless Mie parameter $\rho = \pi d/\lambda$ (Fig. 5.1).

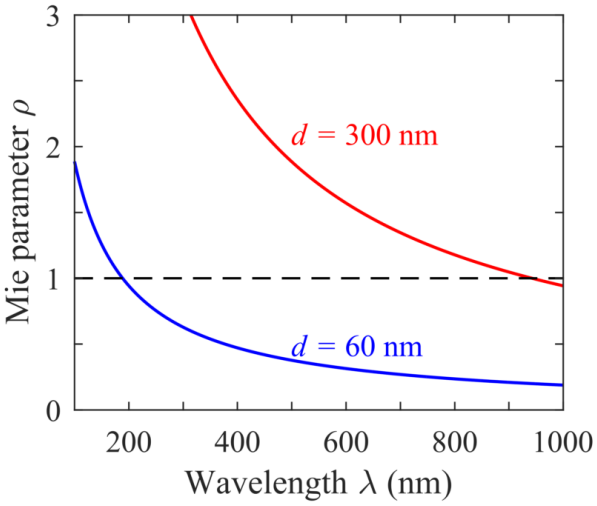

Figure 5.1: Wavelength dependence of the propagation parameter ρ for relevant sphere sizes (as indicated).

For nanoparticles much smaller than the wavelength of the laser field ($\rho \ll 1$), the near-field distribution shows a dipole-like character with maximum field enhancement along the laser polarization direction (Fig. 5.2(a, c)). As the size of a nanoparticle becomes sufficiently large with an associated Mie parameter $\rho > 1$, cf. Fig. 5.2(b, d), excitation of higher order multipole modes results in a shift of the region of maximal field enhancement in the direction of light propagation. Thus, for an appropriately sized nanoparticle illuminated with linearly-polarized two-color laser pulses consisting of the fundamental wave and its second harmonic ($\omega/2\omega$ pulses), the near-field distributions of the ω and 2ω spectral components exhibit different spatial near-field profiles and, most importantly, the points of maximum enhancement (hot spots) are spatially separated. This is illustrated in figure 5.2 for a 300 nm diameter SiO_2 sphere, where the distributions of the near-field enhancement differ significantly for excitation with the fundamental (Fig. 5.2(b)) and the second harmonic (Fig. 5.2(d)) fields at 780 nm and 390 nm, respectively, and evidenced by the angle $\theta_\mathrm{field}^\mathrm{max}$, where maximum enhancement is observed.

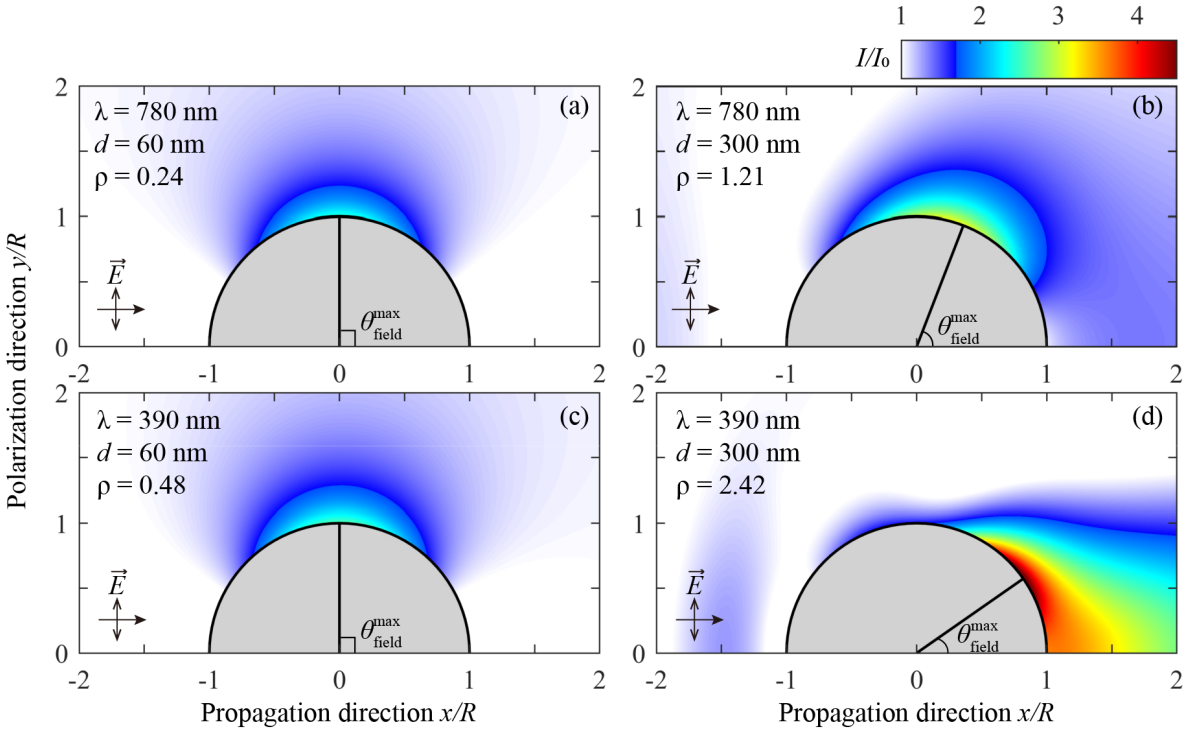

Figure 5.2: Spatial distribution of the intensity enhancement of the near-field at SiO_2 nanoparticles with a diameter of (a, c) 60 nm and (b, d) 300 nm in the propagation-polarization plane as obtained from Mie simulations (wavelengths λ and propagation parameters ρ as indicated). Taken from [155].

The positions and extensions of the hot spots for the ω (red) and 2ω (blue) spectral components of small (d =60 nm) and large (d =300 nm) SiO_2 nanospheres are depicted in Fig. 5.3(a, d). The laser pulses propagate from negetive to positive direction along the x-axis, and are linearly polarized along the y-axis. Only the upper-half spheres are shown here due to the symmetric distribution along the laser propagation direction. For 60 nm nanoparticles (Fig. 5.3(a)), the hot spots overlap and concentrate along the polarization vector of the laser field. The behaviour can be understood by inspection of the field enhancements of the ω and 2ω spectral components (shown in Fig. 5.3(b)), where the ratio between the angle-dependent near-field enhancements $\alpha_{2\omega/\omega}$ is close to 1, irrespective of the emission angle. Here, the intensity of the ω component is $I_\omega = 1.3 \times 10^{13}\,\mathrm{W/cm^2}$, and the intensity ratio is $\eta = I_{2\omega}/I_\omega = 0.5$. For 300 nm nanoparticle (Fig. 5.3(d)), the hot spots for the ω and 2ω spectral components differ substantially at the backside of the sphere ($\theta_{\mathrm{em}} < 90°$). This is due to the field propagation effects with different propagation parameter ρ for the two spectral components as described in section 5.2. The corresponding angular-dependent near-field enhancements exhibit different spatial profile as shown in Fig. 5.3(e). The near-field enhancement ratio $\alpha_{2\omega/\omega}$ is nearly constant at the front side of the

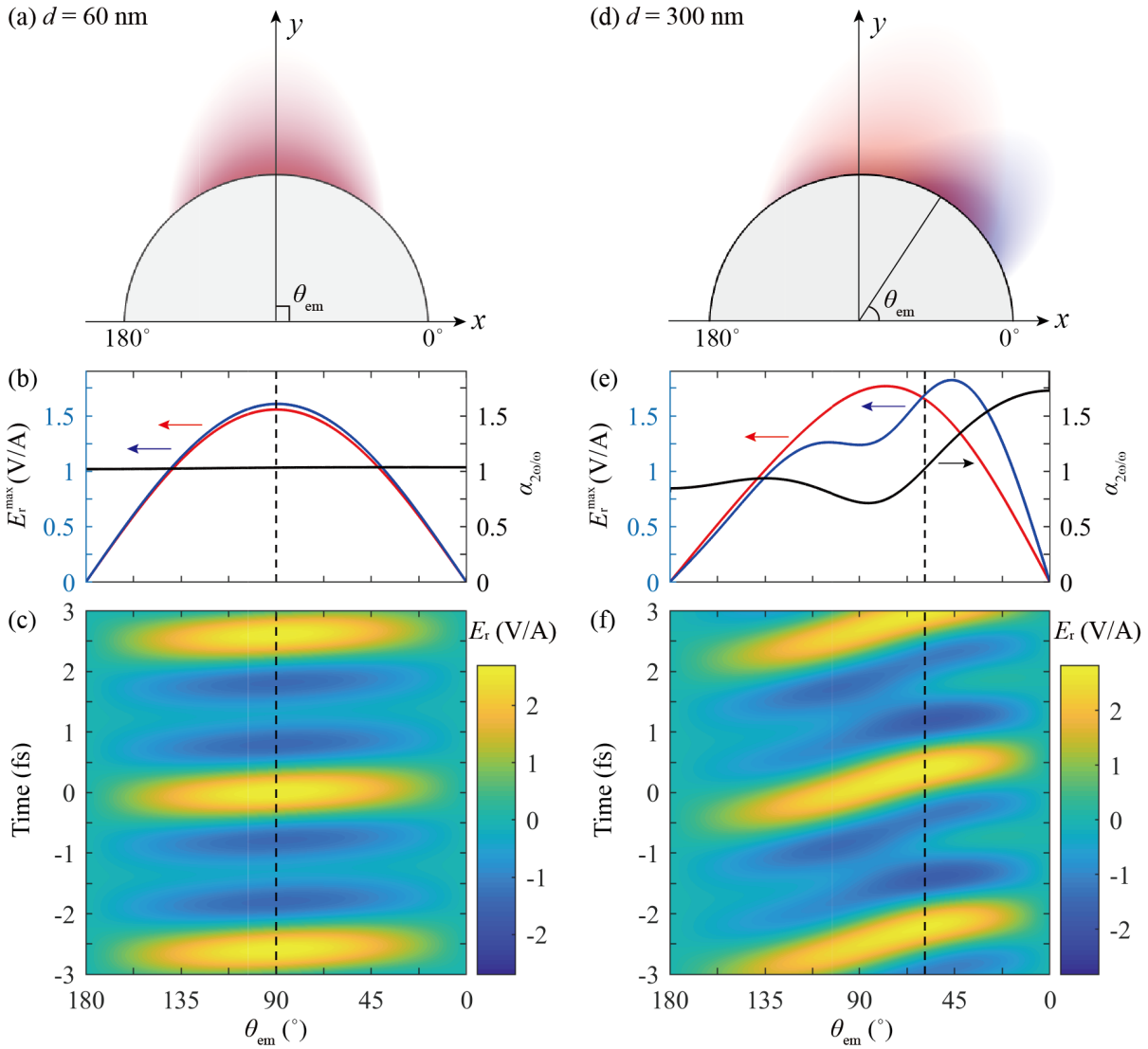

Figure 5.3: Spatial distribution of enhancement profiles for the ω (red) and 2ω (blue) components for (a) $d = 60\,\text{nm}$ and (d) $d = 300\,\text{nm}$ SiO_2 spheres, respectively. Angular dependence of the maximum near-field (radial component) for the ω (red solid line) and 2ω (blue solid line) components for (b) $d = 60\,\text{nm}$ and (e) $d = 300\,\text{nm}$ SiO_2 spheres, respectively. The solid black lines show the relative ratio of the radial fields for the ω and 2ω spectral components. Angular dependence of the near-field (radial component in the $z = 0$ plane) of the evolution of two-color excited (c) 60 nm and (f) 300 nm SiO_2 sphere. The dashed lines indicate the emission angle of maximum near field. The incident laser intensities are $I_\omega = 2I_{2\omega} = 1.3 \times 10^{13}\,\text{W/cm}^2$.

nanoparticle ($\theta_{\mathrm{em}} > 135°$) and varies monotonously at the back side. Fig. 5.3(c, f) show the time evolution of the near-field at the surfaces of the nanoparticles. The maximum of the near-fields shifts from the polar position ($\theta_{\mathrm{em}} = 90°$) to the back side of the sphere ($\theta_{\mathrm{em}} = 59.1°$) by increasing the diameter from 60 nm to 300 nm. Most importantly, the angular-dependent near-fields on the 300 nm nanoparticle are tilted due to the phase shift of the field propagation on the sphere.

5.3 Two-color control measurements

5.3.1 Photoemission control on momentum distribution

The effect of the two-color field on the electron photoemission and acceleration was studied for SiO_2 nanospheres of two different diameters d: 60 nm and 300 nm, where electron emission was recorded as a function of the two-color phase. Figure 5.4(a, d) shows typical phase-averaged momentum distributions for both nanoparticle sizes. Although, at low momenta, the distributions may contain spurious photoemission signal from residual background gas, the high momentum electrons originate predominantly from nanoparticles via ionization and backscattering at the surface [48]. The high-energy signal can thus serve to inspect the directional control of the two-color electron emission. Figures 5.4(b, c) and 5.4(e, f) display typical phase-resolved VMI images after subtraction of the phase averaged spectra and reveal that the electron emission can be effectively switched between the upwards or downwards direction. For 60 nm diameter particles, field propagation effects are small for both spectral components of the two-color field ($\rho_\omega = 0.26, \rho_{2\omega} = 0.52$) such that the electron emission exhibits a directionally undistorted character with respect to the propagation direction, and a phase controlled contribution that is centered around angles of $\pm 90°$. For the larger nanoparticles (300 nm), field propagation (in particular strong for the 2ω-component, cf. Fig. 5.2(d)) results in a substantial distortion of the electron distribution with an emission preference of high energy electrons towards angles significantly smaller than $90°$ (tilted to the backside of the nanosphere) as shown in Fig. 5.4(e, f).

In order to investigate the photoemission control on momentum distribution by the two-color phase more quantitatively in the experiments, we have extracted the phase-dependent and -independent electron yields by fitting the data for each momentum with the function $Y_{\mathrm{amp}}(p_{\mathrm{x}}, p_{\mathrm{y}})\cos(\phi_{\mathrm{r}} + \Delta\phi(p_{\mathrm{x}}, p_{\mathrm{y}})) + Y_{\mathrm{indep}}(p_{\mathrm{x}}, p_{\mathrm{y}})$ where $Y_{\mathrm{amp}}(p_{\mathrm{x}}, p_{\mathrm{y}})$ is the amplitude of the phase-dependent signal, $\Delta\phi(p_{\mathrm{x}}, p_{\mathrm{y}})$ is a phase offset, and $Y_{\mathrm{indep}}(p_{\mathrm{x}}, p_{\mathrm{y}})$ is the phase-independent signal. In figures 5.5, the experimental modulation amplitude of the phase-dependent signal and phase offset are symmetrical along the polarization direction (y-axis) for diameter $d = 60$ nm, but exhibit a pronounced asymmetry tilt to positive p_{x} direction for diameter $d = 300$ nm. Furthermore, we can also observes an increase in $\Delta\phi$ when going from the front to the back side (figures 5.5(e)) caused by the field propagation effect while the Mie parameter $\rho > 1$ [48]. To illustrate the degree of control, the ratios between the phase-dependent and -independent signals $Y_{\mathrm{ratio}}(p_{\mathrm{x}}, p_{\mathrm{y}}) = Y_{\mathrm{amp}}(p_{\mathrm{x}}, p_{\mathrm{y}}) / Y_{\mathrm{indep}}(p_{\mathrm{x}}, p_{\mathrm{y}})$ were

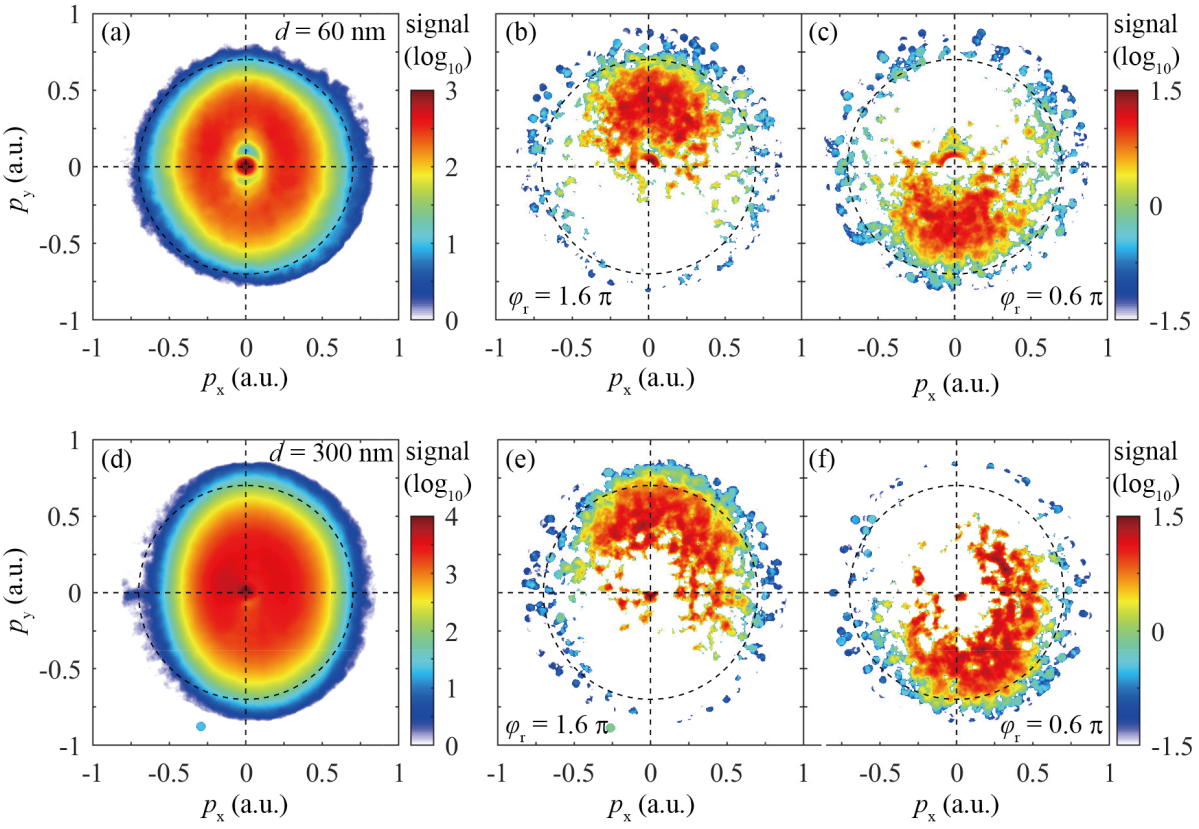

Figure 5.4: Phase averaged projected electron momentum distributions obtained from measurements on SiO_2 nanoparticles of diameter (a) $d = 60\,\mathrm{nm}$, and (d) $d = 300\,\mathrm{nm}$ (Adapted from [155]). The intensities of the spectral components of the two-color laser pulses were $I_\omega = 3 \times 10^{12}\,\mathrm{W/cm^2}$ and $I_{2\omega} = 1.5 \times 10^{11}\,\mathrm{W/cm^2}$. The black dashed circles (0.7 a.u.) are guides to the eye. The phase-resolved VMI images (relative phases as indicated) after subtraction of the phase averaged spectra are shown for (b, c) $d = 60\,\mathrm{nm}$ and (e, f) $d = 300\,\mathrm{nm}$ SiO_2 nanoparticles.

evaluated and are shown in figures 5.5(c,f). We find that the ratio exceeds 0.5 in the near-cutoff regions, indicating a large degree of control with the phase of the two-color laser field.

While similar propagation-induced directional control of the electron emission has already been observed with CEP-controlled few-cycle pulses [48, 76], those studies have been carried out at a single (central) wavelength, such that a change of the CEP allowed only for control of the up versus down emission, while the directionality could only be steered by changing the particle size. In the present study, we focus on an all-optical control of the emission angle, where in addition to having two distinct fields controlled via the two-

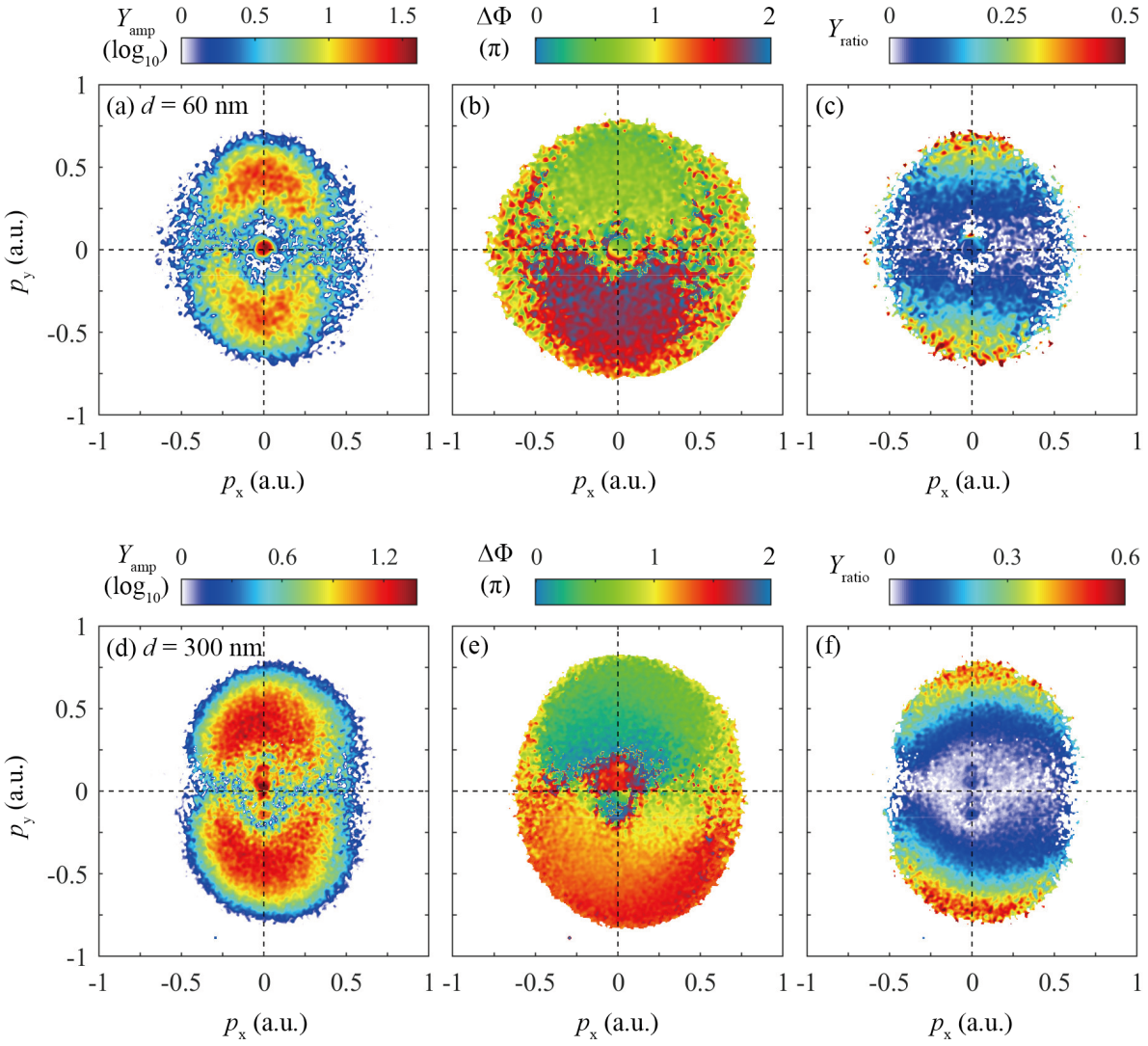

Figure 5.5: (a, d) CEP modulation amplitude $Y_{\mathrm{amp}}(p_\mathrm{x}, p_\mathrm{y})$ and (b, e) phase part $\Delta\phi_{\mathrm{amp}}(p_\mathrm{x}, p_\mathrm{y})$ of diameter $d = 60\,\mathrm{nm}$ and $d = 300\,\mathrm{nm}$, respectively. (c, f) Ratios between phase-dependent and phase-independent signals. The intensities of the spectral components of the two-color laser pulses were $I_\omega = 3 \times 10^{12}\,\mathrm{W/cm^2}$ and $I_{2\omega} = 1.5 \times 10^{11}\,\mathrm{W/cm^2}$.

color phase, the intensity ratio provides an extra parameter to control the relative strength of propagation induced asymmetry in the electron emission in single-sized nanoparticles (shown here for 300 nm). It is noteworthy that our studies are carried out at intensities of several TW/cm^2, which are below the plasma generation threshold. The nanoparticles therefore remain intact during their interaction with the two-color field, such that the dynamics differs strongly from related works on the control of charged particle emission from

clusters and nanoparticles in the plasma regime [154, 160].

5.3.2 Angular and phase-resolved electron cutoff energy map

In order to reveal how tailoring of the temporal waveform of the incident two-color field translates into controlling of the electron emission direction and the maximal electron energy, we have to find the angular-dependent electron cutoff energies at different relative phases of the two-color field. The determination of angular-dependent cutoff energies is the biggest challenge in this study due to the bottleneck of the single-shot data recording (more technical details are in Chapter 3). In this study, an integration time of 60 seconds per relative phase is required to record a decent spectrum. Two typical raw momentum spectra for selected emission angles and relative phase are shown with black lines in Fig. 5.6. The yields of electrons show plateaus in a moderate momentum range (0.1 a.u.< p <0.3 a.u.) and decline into noise level exponentially. This universal feature of all the spectra for different emission angles and relative phases enables us to fit the raw momentum spectra with a Fermi function (c.f. red lines in Fig. 5.6). The cutoff is obtained as the momentum where the corresponding normalized yield drops by two orders of magnitude compared to the yield in the plateau region.

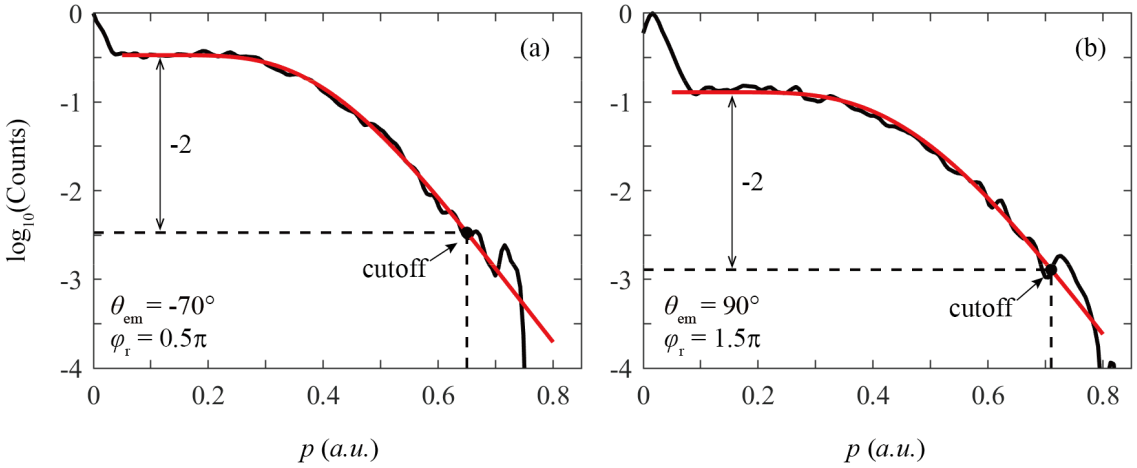

Figure 5.6: Typical raw momentum spectra for selected emission angles and relative phases (black lines), which have been fitted with a Fermi function (red lines) to determine the cutoffs (black dots).

Figure 5.7(a) shows a typical cutoff energy map of photoemitted electrons as function of emission angle and relative ω-2ω phase. The cutoff energies are presented in unit of ponderomotive potential of the ω spectral component. As the map shows a periodic symmetry in relative phase, we applied a 2D fast fourier transform (FFT) analysis to remove the high frequency noises. Only the lowest five Fourier orders of data points (see rectangle

on full FFT data in Fig. 5.7(b)) are used in the filtering process. Comparing to the raw cutoff energy map, the filtered map maintains the angular and phase features as shown in Fig. 5.7(c). Most importantly, the filtered map can easily be characterized regarding the angular and relative phase behaviour.

To fully characterize the angular and relative phase dependent cutoff energy map in Fig. 5.7(c), we introduced three parameters, 1) relative phase dependent optimal emission angles (blue lines), 2) angular dependent phase offsets (black lines) and 3) critical emission angles (white dots). The phase dependent electron cutoff energy E_c for each emission angle θ_{em} is fitted with a function $E_c(\varphi_r) = E_0 + E_{amp}\cos(\varphi_r - \varphi_{offs})$, where E_0 is a constant offset, E_{amp} is the maximum amplitude of the cutoff modulation and φ_{offs} is the relative phase for which the maximal cutoff is realized for a given angle. The emission angle which yields the maximum cutoff energy is called critical emission angle θ_{em}^{crit}.

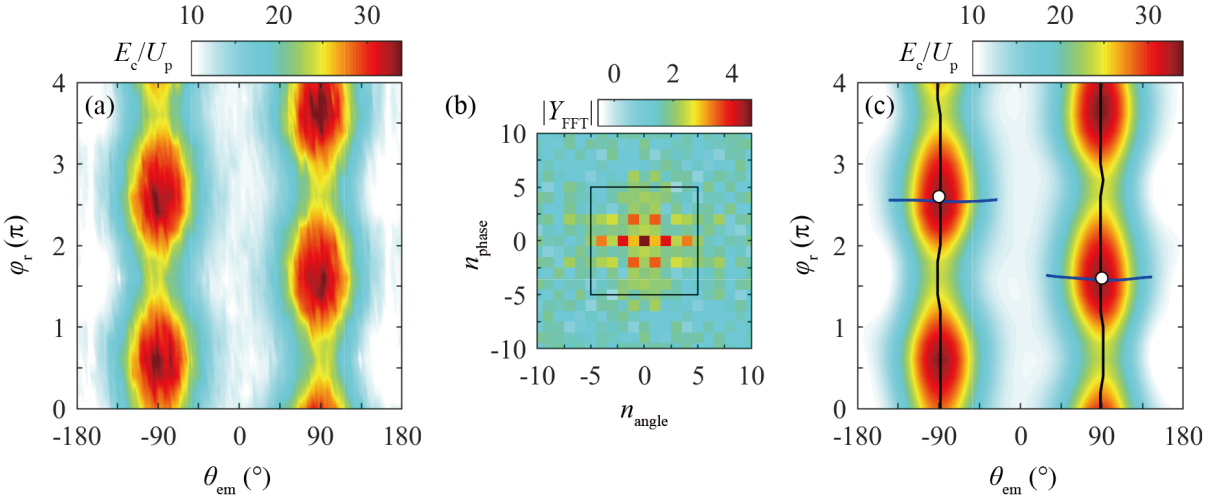

Figure 5.7: (a) Raw angular and phase-resolved electron cutoff energies measured for SiO_2 nanoparticles induced by two-color laser fields. The cutoff energies were obtained by Fermi fitting (see text for details). (c) Angular and phase-resolved electron cutoff energies by employing a discrete 2D-Fourier filtering algorithm to the cutoff energy map. Only the lowest five Fourier orders were used to filter out high frequency noise, as shown in (b). The solid blue lines, black lines and white dots are angular dependent phase offsets $\varphi_{offs}(\theta_{em})$, relative phase dependent optimal emission angles $\theta_{em}^{opt}(\varphi_r)$ of the cutoff energies and critical emission angles θ_{em}^{crit}, respectively.

5.3.3 Photoemission control on kinematic electrons

The filtered angular and relative phase dependent cutoff energy maps of SiO_2 nanospheres are presented in Fig. 5.8(a-c). The diameter of nanoparticles and the intensity ration

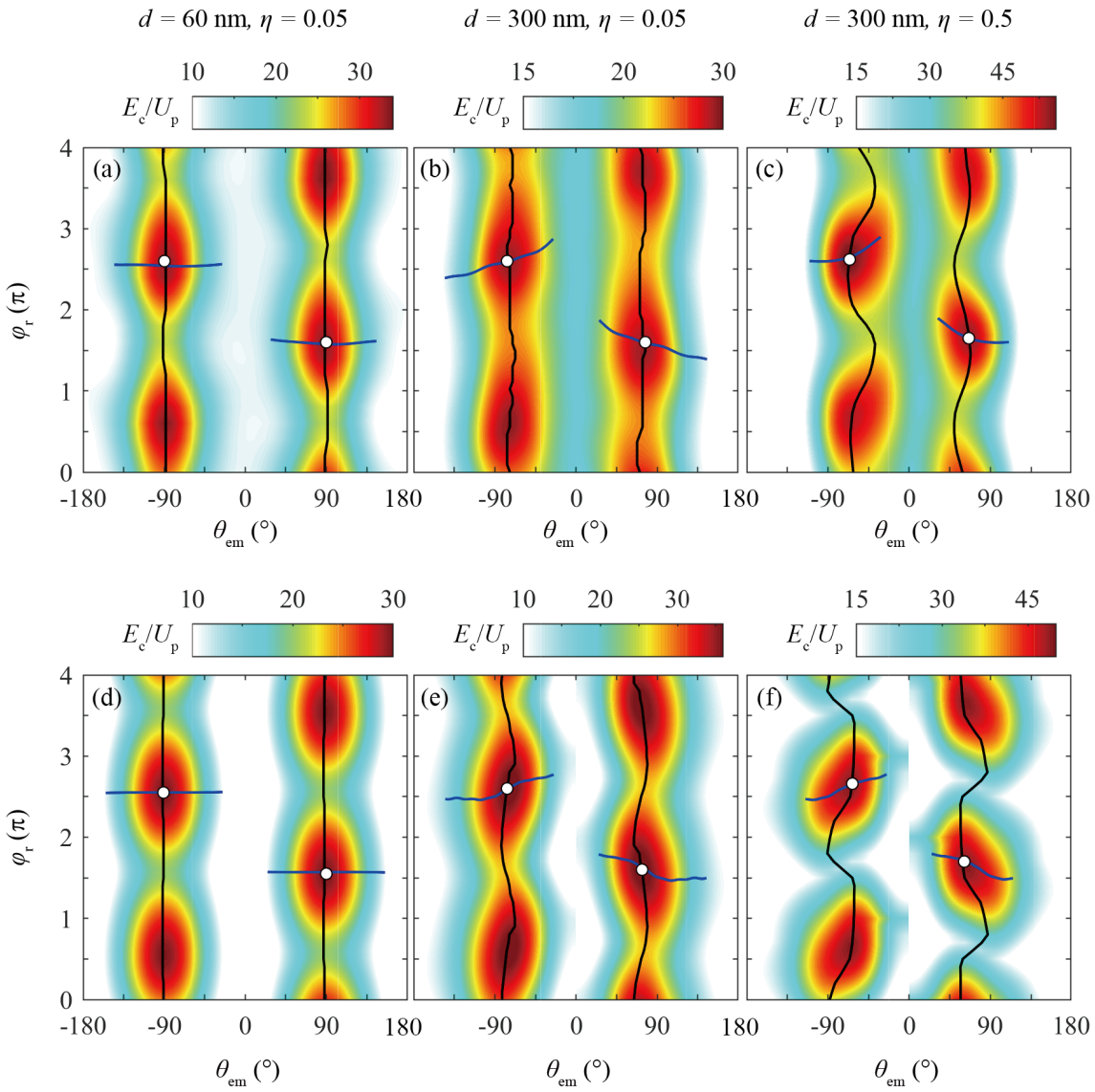

Figure 5.8: Angular and phase-resolved electron cutoff energies measured (a-c), and calculated (d-f) for SiO_2 nanoparticles induced by two-color laser fields. The IR intensity was $I_\omega = 3 \times 10^{12}\,\mathrm{W/cm^2}$. The relative intensities of 2ω fields η and the nanoparticle diameters d are indicated accordingly. Energies are normalized to the ponderomotive potential of the incident IR field. The solid blue lines are angular dependent phase offsets $\varphi_{\mathrm{offs}}(\theta_{\mathrm{em}})$. Black lines show the relative phase dependent optimal emission angles $\theta_{\mathrm{em}}^{\mathrm{opt}}(\varphi_{\mathrm{r}})$ of the cutoff energies and white dots indicate the critical emission angles $\theta_{\mathrm{em}}^{\mathrm{crit}}$. Taken from [155].

between the two spectral components are indicated accordingly. For the small (60 nm) nanoparticles (Fig. 5.8(a)), the critical emission angle is close to $\pm 90\,^\circ$, reflecting maximum

enhancement at the particle poles in the absence of propagation effects for both ω and 2ω components (see Fig. 5.2 (a) and (c)). As a result, the relative phase has negligible effect on the directionality and only modulates the cutoff energies, with opposite sign for the upward versus downward emission direction. This type of directional control via the phase corresponds to the up-down switching observed previously with CEP-controlled few-cycle fields [48]. For the larger (300 nm) particles (Fig. 5.8(b-c)), however, the critical emission angle is not only shifted to smaller values (i.e. towards the light propagation direction), as also seen in few-cycle experiments [48], but exhibits a clear structural modification of the angular distributions as a function of the relative ω-2ω phase φ_r. When the intensity ratio $I_\omega/I_{2\omega}$ is relatively small ($\eta = 0.05$), the optimal angle shows little variation around the critical emission angle $\theta_{em}^{crit} = 75°$ (Fig. 5.8(b)). For a significantly larger intensity ratio ($\eta = 0.5$), the optimal angles are shifted to considerably smaller values and lie around 63 degrees, see Fig. 5.8(c). The optimal angles show a rapid variation (directional switching) of around 25 to 30 ° as function of the relative phase, see black curve in Fig. 5.9. This switching demonstrates the feasibility of using two-color laser fields for the control of the emission direction of the most energetic electrons from nanoparticles. This observation goes beyond the recently shown two-color control of the cutoff in the electron emission from metallic nanotips [30, 31, 161].

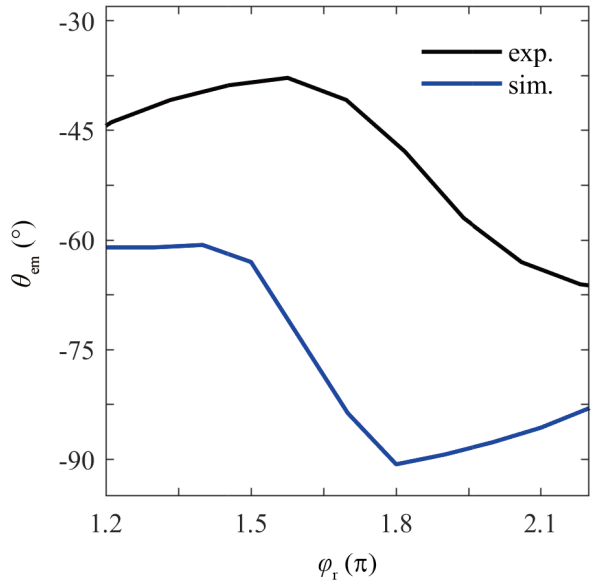

Figure 5.9: Optimal angles for downward emissions from measurement (black, Fig. 5.8(c)) and calculation (blue, Fig. 5.8(f)), respectively. Adapted from [155].

A quantitative analysis of the influence of the intensity ratio between the ω and 2ω components on the preferential energetic electron emission direction is presented in Fig. 5.10. The critical emission angle θ_{em}^{crit} starts at the angle of the maximum enhancement

of the ω component $\theta_{\omega}^{\max}$, and becomes smaller as the 2ω intensity increases. It shifts by about 10 ° when increasing the intensity from 0.05 to 0.5 I_{ω}. The results are quantitatively reproduced by our SMM simulations (blue line) as discussed in the next section.

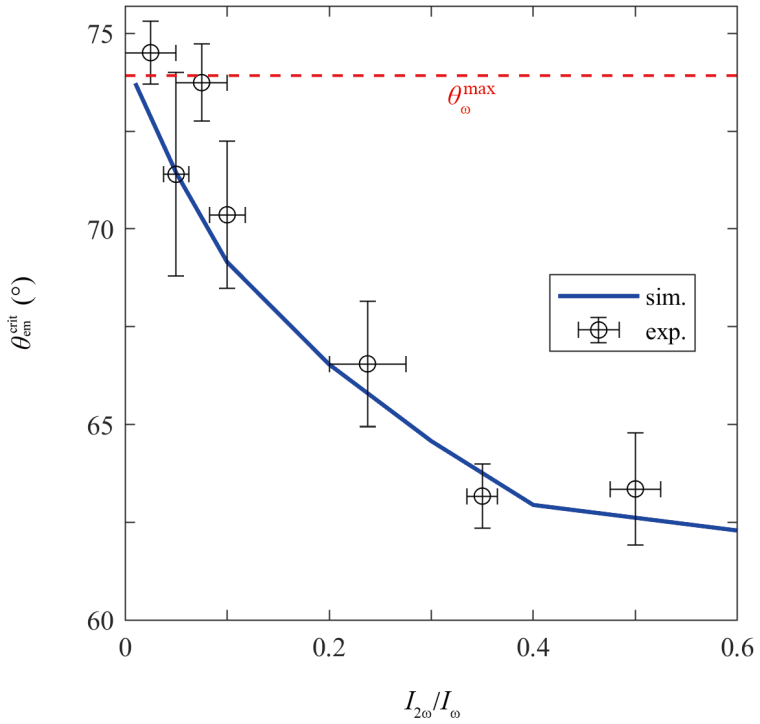

Figure 5.10: Critical emission angles from the measurement (circles) and SMM simulations (solid blue line) with 300 nm SiO_2 nanoparticles. The horizontal error bar indicates the uncertainty of the experimental intensity ratio. The vertical error bars reflect the confidence interval for the fit of the phase dependent electron cutoff energy. The angles of the maximum enhancement of ω and 2ω components are $\theta_{\omega}^{\max} = 74.2°$ (red dashed line) and $\theta_{2\omega}^{\max} = 36°$, respectively. Taken from [155].

5.4 3D semi-classical trajectory simulation

To identify the mechanism behind the observed all-optical control of emission directionality of the most energetic electrons from nanospheres, we performed 3-dimensional (3D) semi-classical trajectory simulations based on the Simple-Man's Model (SMM) (see Chapter 2 for details). Briefly, classical electron trajectories are generated at the nanosphere surface and propagated in the two-color near-field. The temporal and spatial evolution of the latter is described by the Mie solution. For trajectories returning to the surface, elastic specular reflection is assumed. The energy acquired by the electron can be expressed in terms of the

ponderomotive potential U_p. The trajectories are placed at the classical tunnel exit with zero velocity, and weighted by Ammosov-Delone-Krainov (ADK) atomic tunnel ionization rates [99].

As is known from previous work [66, 69, 70, 75], the near-field enhancement and multi-particle charge interaction of the liberated electrons and residual ions contribute to the electron acceleration process and can result in an increase of the electron emission cut-off to several tens of U_p [48, 66]. As the laser intensity in this study, however, was below $1 \times 10^{13}\,\mathrm{W/cm^2}$, where multi-electron effects are negligible [42], the SMM can provide an adequate description of the electron acceleration dynamics.

The control of the photoemission of the most energetic electrons for small and large diameter SiO_2 nanoparticles, cf. Figs. 5.8(a-c), is well reproduced by the SMM simulations using the experimental parameters, see Figs. 5.8(d-f). Most importantly, the simplified model qualitatively reproduces the relative phase-dependent directional switching (cf. blue curve in Fig. 5.9). The remaining offset in absolute angles between experimental results and the simulations (black vs. blue line in Fig. 5.9) can be caused by the simplified description of elastic collisions in the model (i.e. specular scattering), and could arise from an inhomogeneous VMI detector response, as already outlined in ref. [48] for CEP-dependent measurements. Nevertheless, the main feature of the directional switching is clearly captured by the model.

5.5 Selective activation of 2ω field

In principle, the presence of the 2ω field component can affect both the magnitude and spatial distribution of the ionization rate as well as the trajectory dynamics of the released electrons. The relative contributions of the effects of the 2ω field on the ionization rate and the trajectory propagation can be revealed by performing a selective activation in the SMM simulations.

In Fig. 5.11(a) we show the predicted angular and phase-resolved electron cutoff energies with the 2ω field included in the trajectory propagation but neglected in the ionization rate (here just driven by the ω field) and Fig. 5.11(b) for the 2ω field included in the ionization process, but propagation just driven by the ω field. Note that the impact on the tunnel exit is assumed to be negligible due to the relatively weak 2ω field. We closely compared the phase offsets from the calculations for both cases to the full simulation in Fig. 5.12. The phase offset from the full simulation (blue line) is well reproduced when including the 2ω component only in the propagation but not in the ionization (see blue circles). The green solid lines show the phase evolution of the maximum radial vector potential ($\varphi_{\mathrm{pot.}}$) of the full two-color field on the nanosphere surface. The phase offsets obtained in simulations with the 2ω component being included only in the propagation qualitatively follow $\varphi_{\mathrm{pot.}}$.

The angular dependent phase offsets in Fig. 5.12 exhibit a tilt with emission angle. This arises from the change of the relative phase of the two-color field on the nanosphere surface due to field propagation [48]. The relative phase changes only weakly as function

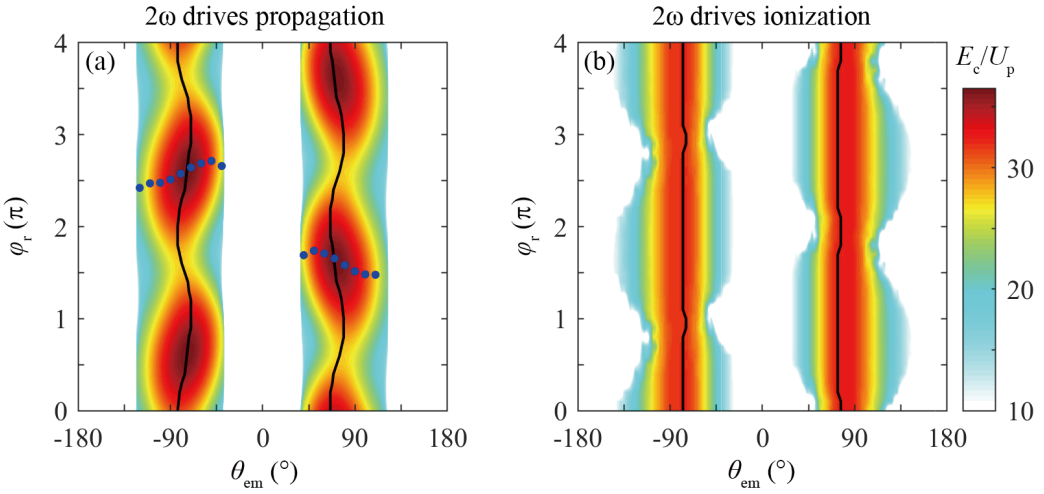

Figure 5.11: Angular and phase-resolved electron cutoff energies in two-color laser fields predicted by SMM for 300 nm SiO_2 nanoparticles. The laser parameters are the same as in Fig. 5.8(e). The 2ω fields are selectively activated in the calculations as indicated in (a) and (b). The blue circles in (a) show the fitted angular dependent phase offsets $\varphi_{\text{offs}}(\theta_{\text{em}})$. The black lines are the phase dependent optimal emission angles. Taken from [155].

of angle on both front side ($\theta_{\text{em}} > 100\,°$) and back side ($\theta_{\text{em}} < 60\,°$) of the nanosphere. In between, in the most relevant 'hot' area with strong field enhancement (cf. Fig. 5.2(b)), the phase change has a roughly linear slope and is in good agreement with the evolution of $\varphi_{\text{pot.}}$. Most importantly, the directional switching (see black lines in Fig. 5.11(a)) can unambiguously be attributed to the two-color effect on the trajectories.

5.6 Conclusions

In conclusion, all-optical control of the directional emission of the most energetic electrons from nanospheres with intense two-color femtosecond laser fields was demonstrated. Field propagation in the nanospheres resulting from excitation by the ω and 2ω components of the two-color laser field determines the emission direction of the high-energy electrons. The control is observed for nanoparticle sizes for which the Mie size parameter ρ is above unity for at least the 2ω field. Trajectory simulations captured both the two-color phase modulation and optimal emission angles for the energetic photoemission at different ω-2ω intensity ratios. A selective activation of the 2ω field in the simulations revealed the pivotal effect of the trajectory modification on the energetic electron emission.

The all-optical control scheme demonstrated for isolated nanospheres is expected to be applicable also in more complex (isolated and surface based) nanosystems. The presented work paves the way towards all-optical control of quantum dynamics in near-fields and

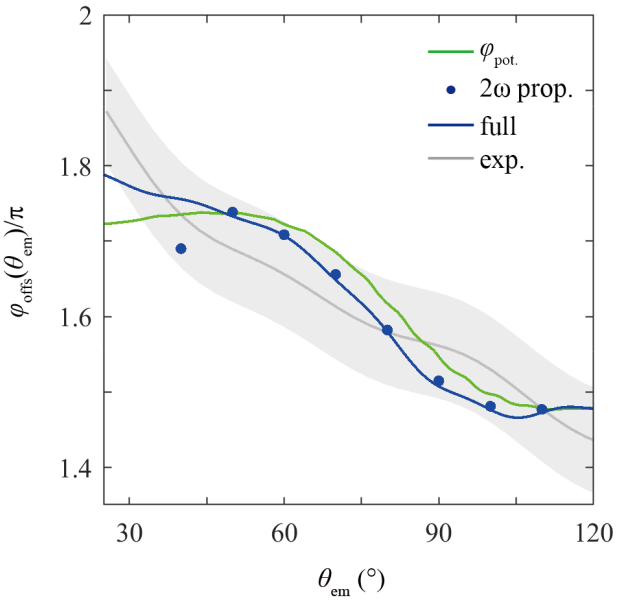

Figure 5.12: Comparison between phase offsets from full SMM calculations (blue line) with the 2ω field included only in the trajectory propagation (blue circles). The green solid line is the phase offset obtained from the maximum radial vector potential. The phase offset obtained from experiment is shown as grey line. The shadow indicates the confidence interval of the fit of phase dependent electron cutoff energies. Adapted from [155].

may find applications in the generation and control of ultrashort electron pulses.

Chapter 6

Sub-cycle metallization of nanoparticles probed via CEP dependent electron acceleration [1]

6.1 Introduction

When illuminating SiO_2 nanoparticles with few-cycle laser pulses with intensities below $10^{14}\,W/cm^2$, cutoff energies up to about 53 U_p were observed [67, 68, 163]. The increase of cutoff energies of emitted electrons as compared to an atomic gas with 10 U_p was explained by linear near-field enhancement, and nonlinear charge interactions. The latter consist of mainly two contributions: (i) a trapping field forming near the surface mediated by residual ions, and assisted backscattering during the recollision phase and (ii) Coulomb explosion of the emitted electron bunch [75].

In this chapter [2], we experimentally observe an increase in the emitted electron cutoff energy and a distinct modification in the CEP-dependence of the sub-cycle acceleration dynamics which occurs at laser peak intensities above the damage threshold. Simulations with an adapted M^3C model with time-dependent permittivity reveal the physical origin and relevant time scale of the phase transition.

6.2 STOF measurements

6.2.1 Experimental approach and samples

The stereo time-of-flight (STOF) spectrometer described in section 3.7 was employed in the measurements of photoemission from nanoparticles with intense few-cycle laser pulses. For each laser intensity scan, over 10^6 laser shots were recorded for a decent signal-to-noise

[1] The main results in this Chapter will be published in [162].

[2] The experimental results were already presented in Süßmann's thesis [130], but I reanalyzed the raw data and did the complete modeling.

ratio. An extra ATI background gas scan right after the nanoparticle scan was carried out for laser intensity calibration.

The 95 nm SiO_2 nanoparticles were prepared by wet chemical synthesis as described in section 3.1. The polydispersity of the particles was smaller than 10% [68].

6.2.2 Intensity dependence of spectral cutoffs

Figure 6.1(a) shows electron energy spectra for 95 nm SiO_2 nanospheres at various intensities. Each spectrum was averaged over the signals from all CEPs and from both time-of-flight detectors. The spectra show a strong signal at low energies which is mostly contributed by ATI from background gas. The signal at high energies shows an exponential-like distribution and is exclusively dominated by rescattered electrons from nanoparticles. The shape of the spectra do not change noticeably for the various intensities. The dashed lines indicate the cutoff values of the spectra which were determined by the procedure described in section 3.7. Figure 6.1(b) shows the cutoff energy as a function of laser peak intensity. The error bars denote the experimental error introduced by trigger jitter and the limited time resolution of the data acquisition system. The energy cutoff increases monotonically with laser intensity. An increase in slope can be observed and illustrated by the cutoff energy E_c divided by the ponderomotive potential U_p, as shown in Fig. 6.1(c). The rescaled cutoff E_c/U_p lies around 53 with the laser intensity below $1.8 \times 10^{14}\,\mathrm{W/cm^2}$ (henceforward referred to as turnover intensity). This is consistent with the observations at lower laser intensities reported by Zherebtsov *et al.* [66, 68] where a variety of effects have been discovered that contribute to the electron acceleration and determine the cutoff of the electron spectrum. These include the modification of elastic electron backscattering by field enhancement [75], nanofocusing [48], as well as local and non-local charge interactions [75, 76]. While increasing the laser intensities, the cutoff increases, and stays at nearly constant value around 100 U_p with laser intensities higher than $3.0 \times 10^{14}\,\mathrm{W/cm^2}$.

6.2.3 CEP dependence at high intensities

Further analysis was carried out on the CEP-dependence of the electron momentum spectra. The CEP-dependence is sensitive to the field-driven process rather than the much slower intensity-envelope driven particle dynamics, which would randomize directional emission and wash out any CEP-dependence. The quantification of CEP-dependence of the electron emission along the polarization axis was described in section 3.7. Figure 6.2 presents the asymmetry maps for various laser intensities of 95 nm SiO_2 nanospheres. The asymmetry maps in the low momentum ranges e.g. below the cutoff momentum of background gas (red dashed lines) are less informative due to the mixed signals. The oscillating pattern in the asymmetry maps above the cutoff momentum of the background gas are only contributed by photoemissions from nanoparticles. The asymmetry parameter shows characteristic momentum-dependent periodic oscillations with CEP in all data sets. Remarkably different behavior is seen for the laser intensities below and above the turnover intensity. For lower intensity (cf. Fig. 6.2(a)), the nearly straight asymmetry features in

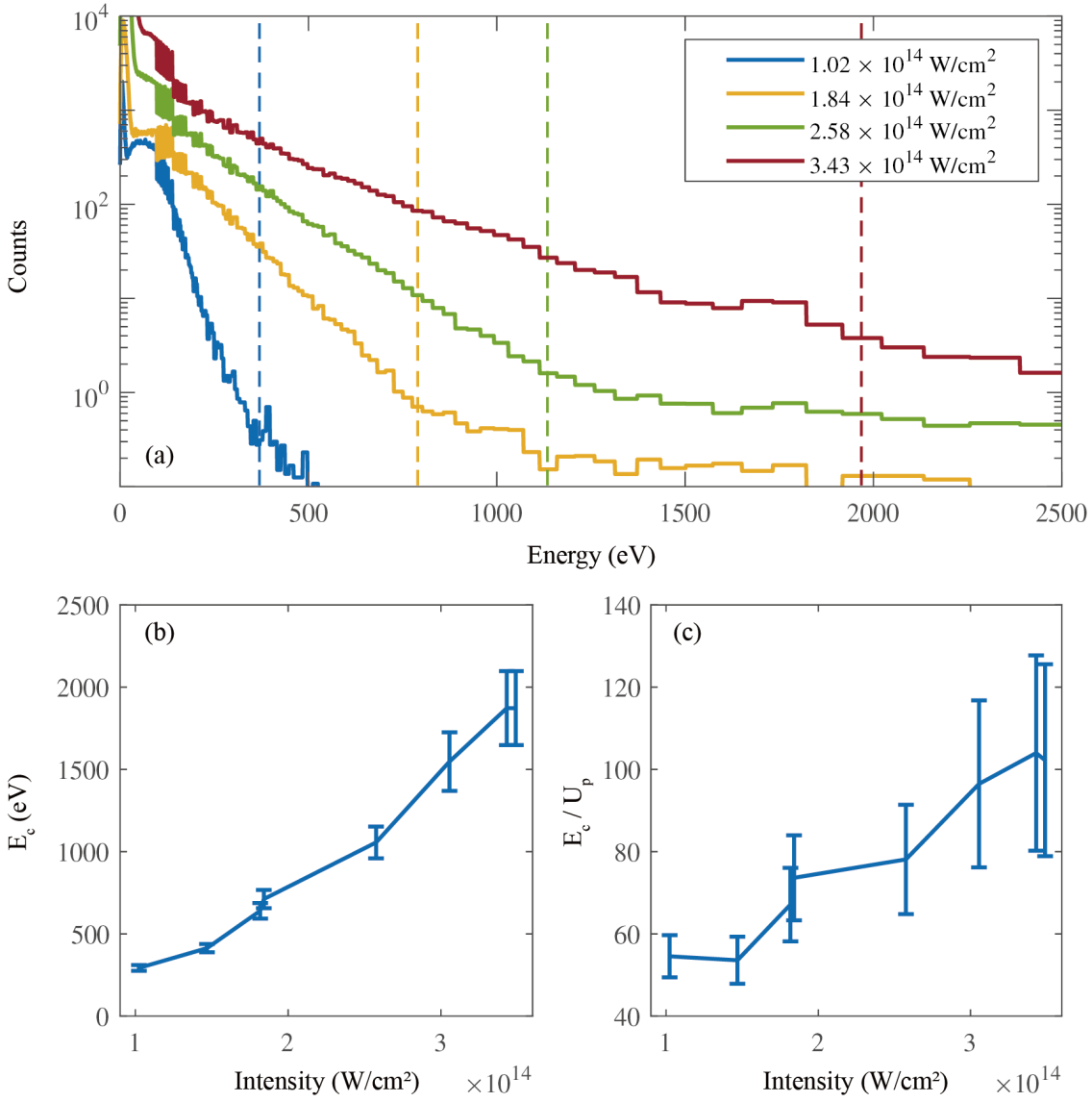

Figure 6.1: a) Photoelectron energy spectra from 95 nm SiO_2 nanospheres for four different intensities. b) Cutoff energies for 95 nm SiO_2 plotted against intensity. c) Rescaled cutoff dependence E_c/U_p as a function of intensity. Adapted from [130].

the cutoff region (black lines) indicate an energy-independent phase behavior, similar to previous studies [66, 68]. In contrast, at higher intensity (cf. Fig. 6.2(c,d)) the asymmetry features are strongly tilted to the left in the cutoff region such that the emission phase decreases with energy. For the laser intensity around $1.8 \times 10^{14}\,\mathrm{W/cm^2}$ (cf. Fig. 6.2(b)),

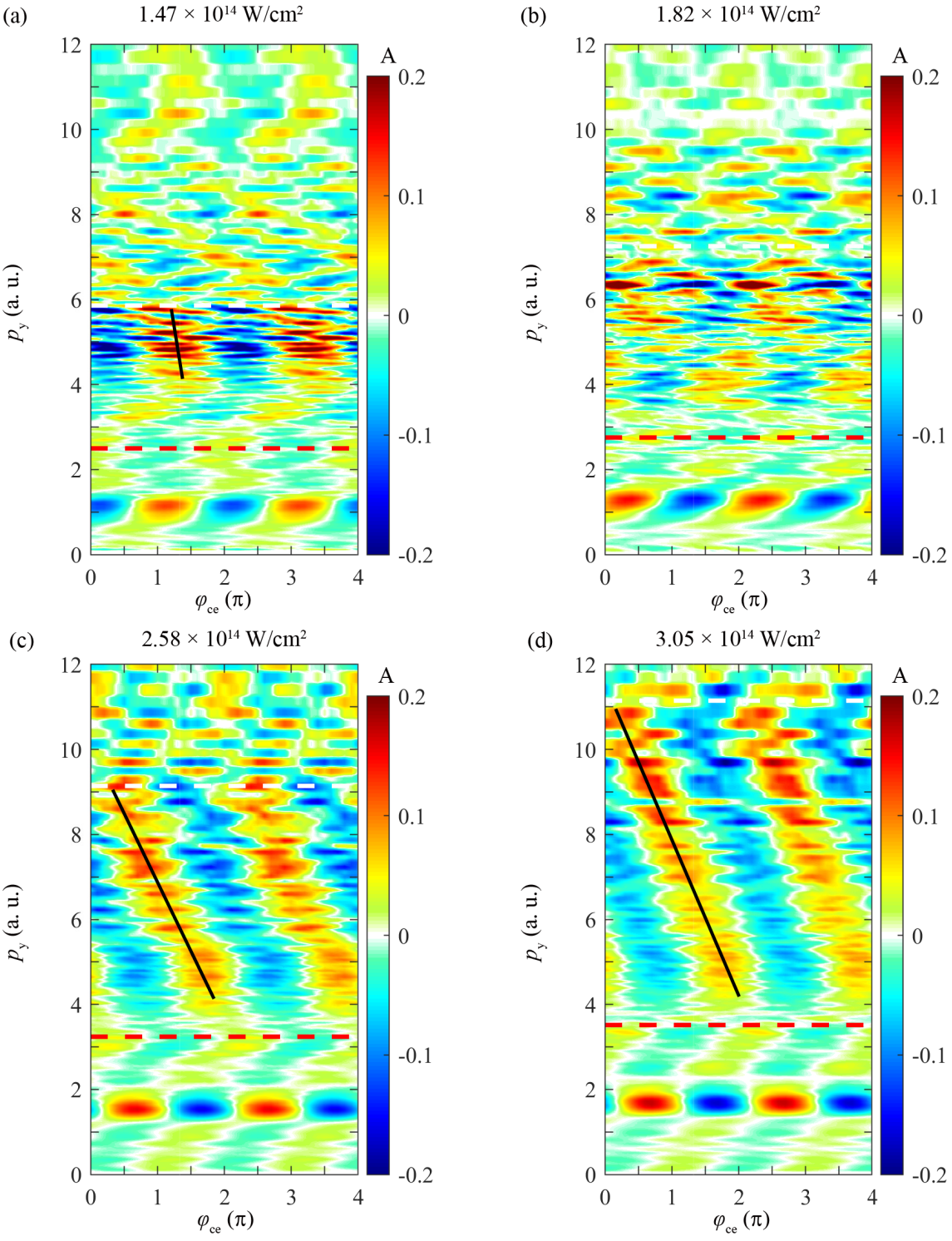

Figure 6.2: CEP asymmetry map (momentum scale) for 95 nm SiO_2 nanospheres for four different intensities as indicated. The cutoff momentum obtained from the time-of-flight spectrum is indicated for the nanoparticles (white dashed line) and for the background gas obtained independently also via a reference scan (red dashed line). The black solid line indicates the trend of phase dependence. Adapted from [130].

one observes a decrease of the effective asymmetry especially in the cutoff region. This is due to the expectation of a high non-linearity where slight changes of the laser intensity around the turnover intensity yield different CEP dependent electron emission.

Note that the effective laser intensity experienced by an individual nanoparticle is not precisely known due to the inherent spatial distribution of the particle beam in the laser focus. Nanoparticles in the wings of the laser focus necessarily experience a lower intensity than those exposed to the center, peak intensity. Consequently, the measured observables, e.g., photoelectron energy and angular distributions, effectively average over the spatial intensity distribution of the laser field [164].

6.3 Theoretical predictions

We employed the M^3C model to reveal the phase dependent electron acceleration process. The cutoff energies obtained from M^3C simulations with laser intensity ranging from $1 \times 10^{14}\,\mathrm{W/cm^2}$ to $4 \times 10^{14}\,\mathrm{W/cm^2}$ are shown in Fig. 6.3(a) (blue dashed line). The cutoffs are defined as the energy where the corresponding electron yield (cf. Fig. 6.3(b,c)) drops by four orders of magnitude compared to the maximum yield near zero kinetic energy. The calculated cutoff decreases linearly while increasing the laser intensity. This is due to a less efficient mean field acceleration mechanism in combination with a strong increase in the trapping potential. With higher laser intensity, the tunnel exits of electrons are much closer to the sphere surface, and the time for leaving the near-field after rescattering is drastically reduced due to the much higher kinetic energy. The calculated cutoffs agree well with the experimental data (black circles in Fig. 6.3(a)) below the turnover intensities. But for intensities close to and above the turnover intensity, the cutoffs show a huge discrepancy compared to the experimental data. The discrepancy inspires us to search for new physical processes, which play considerable roles in the high intensity region but had not been yet included in the M^3C model. As described in section 2.4, the time evolution of near field around the nanosphere is derived by assuming the optical properties of the material to be constant. This is questionable at laser intensity close to and above damage threshold, where the electric fields in the medium can reach several volts per angstrom leading to generation of free charges inside the nanoparticle. A microscopic modelling taking into account all created charges is computationally extremely challenging due to an exponential increase in the number of electrons with laser intensity. We thus used a simple model, where ionization inside the sphere is taken into account via an effective time-dependent permittivity, obtained by a complex Drude dielectric function as detailed in the following.

6.3.1 Optical Kerr-effect

When a dielectric material is exposed to a laser pulse, a polarization is induced depending on the optical properties of the material and the electromagnetic field strength of the laser

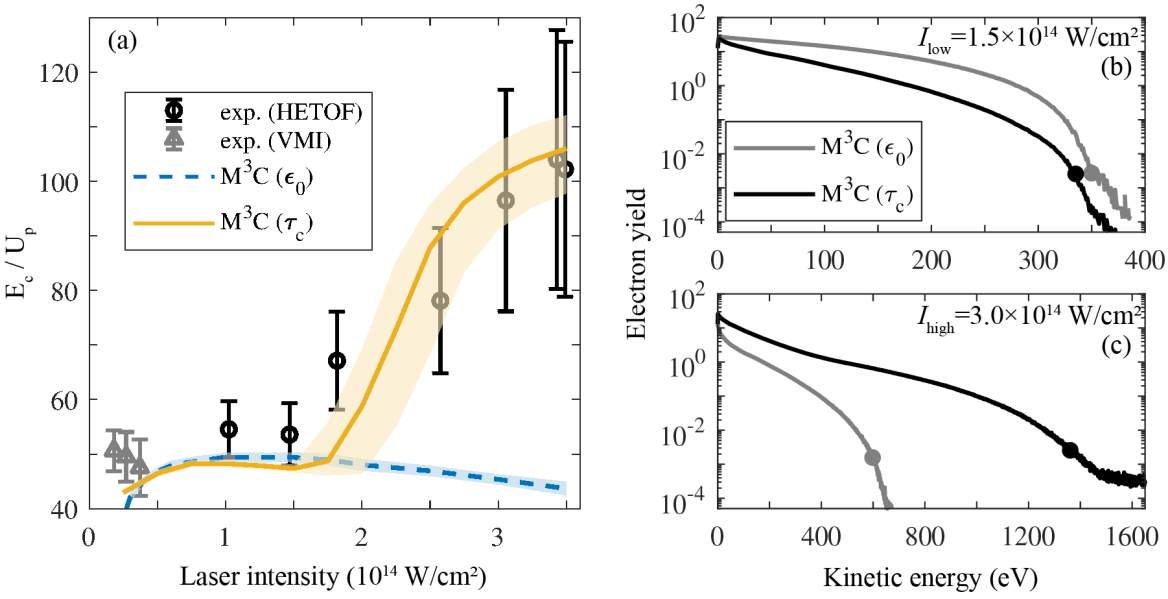

Figure 6.3: (a) Intensity dependence of rescaled cutoff energies of the electron emission from 95 nm diameter SiO_2 nanoparticles. The experimental results are represented as black circles. The error bars are calculated by considering the TOF timing jitter (<300 ps) and the time resolution of the transient recorder (500 ps). The gray triangles are cutoff energies recorded with VMI at much lower laser intensities [68]. The dashed and solid lines indicate the results of the M^{3}C simulations with constant permitivity ε_0 and time dependent permittivity $\varepsilon(t)$ for an electron collision time of 1 fs, respectively. The shaded area represents the calculated cutoff values with electron collision time from 0.5 fs to 1.7 fs. (b,c) The calculated kinetic energy spectra with laser peak intensity of (b) 1.5×10^{14} W/cm^2 and (c) 3×10^{14} W/cm^2, respectively. The focus volume averaging had been taken into account. The gray and black lines represent the calculations with constant permittivity and with time dependent permittivity, respectively. The gray and black dots indicate the corresponding cutoff energies.

field. The intensity dependent refractive index of the material is expressed as [165]:

$$n = n_0 + \frac{3\boldsymbol{\chi}^{(3)}}{8n_0}|\boldsymbol{E}_\omega|^2 = n_0 + n_2 I, \tag{6.1}$$

where $\boldsymbol{\chi}^{(3)}$ is the third order susceptibility, $\boldsymbol{E}_\omega$ is the field amplitude and I is the intensity of the laser field. Beside the linear refractive index n_0, a second-order nonlinear refractive index n_2 known as optical Kerr-effect has to be considered in the case of high intensive laser radiation. The value for the nonlinear refractive index for different dielectrics can be obtained from data bases (e.g. [166]). The values of n_2 are relatively small for most materials, on the order of 10^{-16} cm^2 W^{-1} for typical glasses. Therefore, beam intensities

on the order of 1 GW cm^{-2} can introduce significant variations in refractive index via the Kerr effect. In this study, $n_0 = 1.46$ and $n_2 = 3 \times 10^{-16}\,\mathrm{cm^2\,W^{-1}}$ are employed for SiO_2, respectively.

6.3.2 Plasma-nonlinearity

While the beam intensity is increasing, the presence of free electronic carriers in the dielectric material induced by photo- and avalanche ionization processes is an additional contribution to the refractive index. The complex permeability of the dielectric material connected with electronic carrier density ρ_e can be described by the Drude formalism [165]:

$$\varepsilon(\rho_e) = n^2 - \frac{e^2\rho_e}{m_e^*(\omega^2+\nu_c^2)} + i\frac{e^2\rho_e\nu_c}{m_e^*\omega(\omega^2+\nu_c^2)}, \tag{6.2}$$

where e is the electron charge, $m_e^* = 0.64m_e$ is the effective electron mass, $\omega = 2\pi c/\lambda$ is the frequency of the irradiated central wavelength $\lambda = 720\,\mathrm{nm}$ and ν_c is the electron collision frequency and c is the speed of light in vacuum.

6.3.3 Conducting electron population in SiO_2 nanoparticles

The evolution of the free electron density $\rho_e(t)$ in a dielectric medium exposed to femtosecond laser pulses is written as [61]

$$\frac{\partial\rho_e(t)}{\partial t} = (W_{PI}(I(t)) + W_{AV}(I(t),\rho_e(t))) \cdot \beta - W_{rel}(\rho_e(t),t), \tag{6.3}$$

where $W_{PI}(I(t))$ is the photoionization rate, $W_{AV}(I(t),\rho_e(t))$ is the avalanche ionization and $W_{rel}(\rho_e(t),t)$ is the plasma energy decay term associated with the diffusion and recombination of electrons with a characteristic mean time in materials. $\beta = 1 - \rho_e/\rho_0$ is the scaling term where ρ_0 is the number of valence electrons.

The photoionization rate $W_{PI}(I(t))$ in equation (6.3) is calculated by Keldysh's theory which was shown as [167]

$$W_{PI}(I(t)) = 2\frac{2\omega_0}{9\pi}\left(\frac{\omega_0 m_e^*}{\hbar\sqrt{\Gamma}}\right)^{\frac{3}{2}} Q(\gamma,x) exp\{-\pi\,\langle x+1\rangle \times \frac{K(\sqrt{\Gamma}) - E(\sqrt{\Gamma})}{E(\sqrt{\xi})}\}, \tag{6.4}$$

where the adiabaticity parameter (Keldysh parameter) for solids is $\gamma = \omega_0\sqrt{m_e^* E_g}/e\,|E|$, $E_g = 9\,\mathrm{eV}$ is the band-gap energy of SiO_2 [42, 114, 155], E was the electric field amplitude of the radiation, and $\langle ... \rangle$ denoted the integer part. Further abbreviations were presented as following [62]:

$$\Gamma = \frac{\gamma^2}{\gamma^2+1}, \qquad \xi = \frac{1}{\gamma^2+1}, \qquad x = \frac{2}{\pi}\frac{E_g}{\hbar\omega_0}\frac{1}{\sqrt{\Gamma}}E(\sqrt{\xi}), \tag{6.5}$$

$$Q(\gamma, x) = \sqrt{\frac{\pi}{2K(\sqrt{\xi})}} \sum_{n=0}^{\infty} \exp(-n\pi \frac{K(\sqrt{\Gamma}) - E(\sqrt{\Gamma})}{E(\sqrt{\xi})}) \Phi(\sqrt{\eta(n+2\mu)}), \tag{6.6}$$

$$\eta = \frac{\pi^2}{2K(\sqrt{\xi})E(\sqrt{\xi})}, \qquad \mu = \langle x+1 \rangle - x, \qquad \Phi(z) = \int_0^z \exp(y^2 - z^2) dy, \tag{6.7}$$

here $\Phi(z)$ described the Dawson function, $K(z)$ and $E(z)$ represented the complete elliptic integral of the first and second kind, respectively [168].

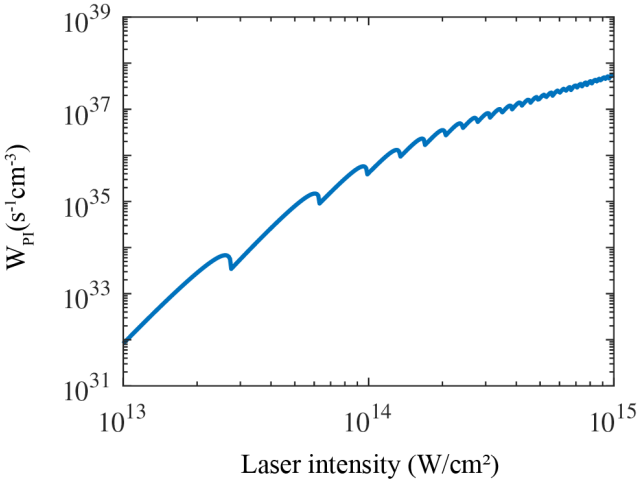

Figure 6.4: Photoionization rates for SiO_2 as a function of laser intensity.

Note that the equation (6.4) has been modified according to [169], where small misprints have been corrected, and an extra factor of 2 due to electron spin degeneracy has been included. Figure 6.4(a) shows the photoionization rates for SiO_2 as a function of laser intensity. The central wavelength of the laser pulse is 720 nm.

The second contribution to ionization is described by the avalanche process. Several avalanche ionization models (*e.g.* Stuart model [170–172], Sparks and Duthler model [173] and Thornber model [174]) had been derived to describe the ionization rate due to the complexity and differences between material categories. One should note that the models above were only developed to reproduce their measurements with special conditions. The parameters involved in the models were mostly defined by empirical values. In our study, we employed the Drude avalanche ionization model which was commonly adopted for calculating the electric field energy absorption and estimating the free electron excitation [168, 175–177]. It could be shown as:

$$W_{\mathrm{AV}}(I(t), \rho_{\mathrm{e}}(t)) = \frac{\sigma}{E_{\mathrm{g}}} \cdot I(t) \cdot \rho_{\mathrm{e}}(t), \tag{6.8}$$

with the absorption cross section

$$\sigma = \frac{e^2}{c\varepsilon_0 n_0 m_e^*} \frac{\tau_c}{1+\omega_0^2\tau_c^2}, \tag{6.9}$$

where $\tau_c = \nu_c^{-1}$ is the mean electron collision time.

In contrast to the process of the increasing free electrons resulting from the photoionization and avalanche ionization, the relaxation process for electrons is modelled by the generation of self-trapped excitons (STEs) which was approximated by:

$$W_{rel}(\rho_e(t), t) = \frac{\rho_e(t)}{\tau_r}, \tag{6.10}$$

where $\tau_r \approx 150\,\text{fs}$ is the relaxation time [64] and consequently this term can be neglected.

The dielectric insulator-to-metal transition occurs when the real part of the permittivity of the nanosphere turns to 0 [178]. Note that the resonance at $\varepsilon = -2$ (Fröhlich condition) is avoided by setting the dielectric constant to $-\infty$ once it turns negative.

6.3.4 M^{3}C with time dependent permittivity

In the simple model we introduced above, the important parameter of mean electron collision time τ_c is crucial to correctly describe the evolution of permittivity. Unfortunately, the precise value of τ_c is unknown, and furthermore, it is dependent on free electron density which builds up during the laser pulse propagation. In this work, we employed $\tau_c = 1\,(+0.7, -0.5)\,\text{fs}$ according to values reported in Refs. [179, 180]. As shown in Fig. 6.3(a), the calculated cutoffs with time-dependent permittivity show reasonable agreement with experimental data at laser intensities both below and above the turnover intensity. A visible discrepancy at intensities around the turnover intensity is due to the high non-linearity in the insulator-to-metal transition, where slight changes in the driving laser pulses yield different outcome. This is also consistent with the asymmetry map presented in Fig. 6.2(b).

Further evidence that the model captures the physical mechanisms responsible for the observed change in the cutoff of accelerated electrons, comes from an inspection of the CEP-dependence of the electron momentum spectra as shown in Fig. 6.5(a,c) for $1.5\times10^{14}\,\text{W/cm}^2$ and $3\times10^{14}\,\text{W/cm}^2$, an intensity below and well above the turnover intensity, respectively. Clear momentum-dependent periodic oscillations with CEP could be observed for both intensities. Similar to the experimental data presented in Fig. 6.2(d), the asymmetry feature is tilted to the left in the cutoff region at high intensity. The simulated asymmetry maps were obtained from simulations for 20 different CEP values. For comparison with the experiment, the asymmetry maps were obtained by angular integration of the electron yields over the experimental collection range ($[-10°, +10°]$). In order to compare the simulation results to the experimental data quantitatively, we fit the measured (Fig. 6.2(a,d)) and calculated (Fig. 6.5(a,c)) asymmetry maps with

$$A_{fit}(p, \varphi_{ce}) = A_0(p)\cos(\varphi_{ce} - \varphi_0(p)), \tag{6.11}$$

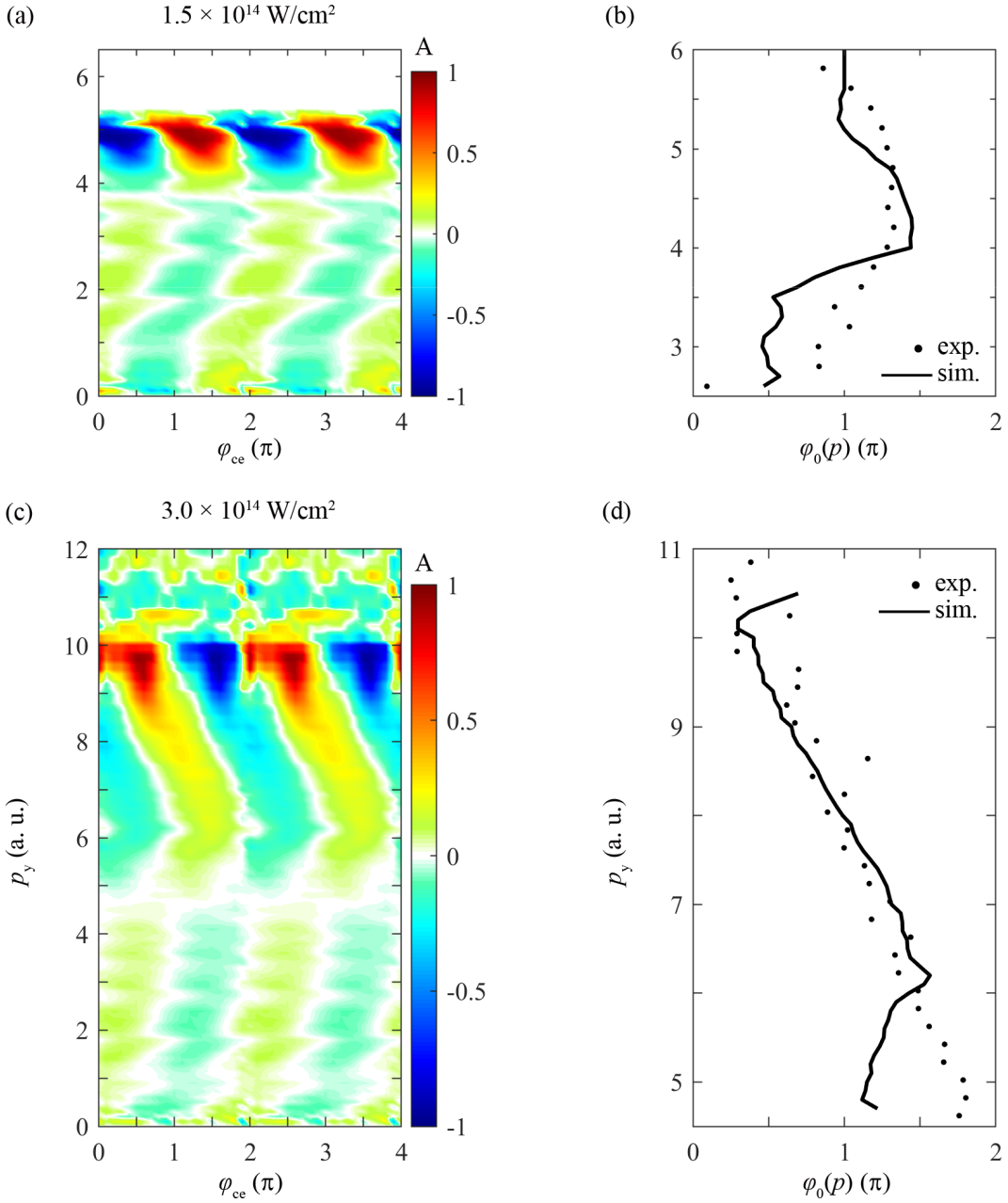

Figure 6.5: (a,c) CEP asymmetry maps (momentum scale) of the electron emission from M^3C simulations with time-dependent permittivity. (b) and (d) compare asymmetry phases from harmonic fits of the measured (dots) and calculated (line) asymmetry maps.

where $\varphi_0(p)$ is the energy dependent asymmetry phase. As shown in Fig. 6.5(b,d), the phase shift behaviours below and above the turnover intensity are well reproduced by our

relatively simple model, supporting that the M^{3}C model including time dependent permittivity captures not only the cutoff energies but also the sub-cycle electron acceleration dynamics, which is imprinted in the asymmetry parameter.

6.3.5 Insulator-to-metal transition

The good agreement of the simulation results with the experimental data motivates a closer analysis of the field-driven dynamics. Figure 6.6(a) shows the time dependent permittivity (real part) of the nanosphere with laser intensity below, at and above the turnover intensity. When laser peak intensity increases, the permittivity of the nanosphere decreases due to the rising electron density. The transient permittivity even decreases to negative value resulting in insulator-to-metal transition when the laser peak intensity is above the turnover intensity.

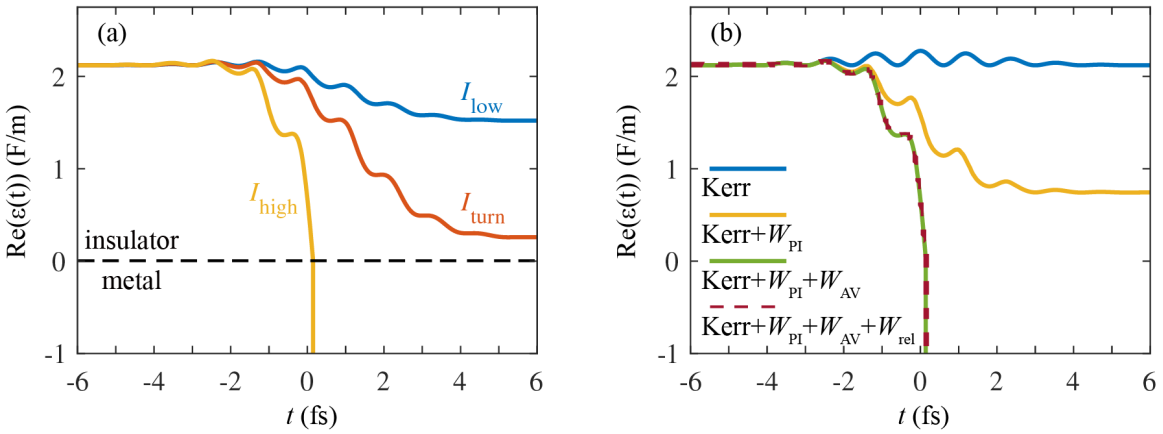

Figure 6.6: (a) Time dependent permittivity with laser intensity of $I_{\text{low}} = 1.5\times10^{14}\,\text{W/cm}^2$, $I_{\text{turn}} = 1.8\times10^{14}\,\text{W/cm}^2$ and $I_{\text{high}} = 3.0\times10^{14}\,\text{W/cm}^2$. (b) Time dependent permittivity by involving different processes as indicated with laser intensity of $3.0\times10^{14}\,\text{W/cm}^2$.

The applicability of the Drude formula as described in section 6.3.2, yields the evolution of permittivity during the pulse propagation in the nanosphere. The evolution of electon density inside the sphere was calculated according to the photoionization rate W_{PI}, avalanche ionization rate W_{AV} and the recombination W_{rel} according to equation (6.3). Figure 6.6(b) shows the permittivity evolutions by involving different contributions at laser intensity of $3.0\times10^{14}\,\text{W/cm}^2$. The calculation with Kerr effect only (blue line) introduces minor change to the permittivity. The photoionization initializes the electrons (orange line), and the avalanche ionization (green line) further assists the insulator-to-metal transition significantly. In contrast, the influence of the relaxation process is nearly negligible (red line).

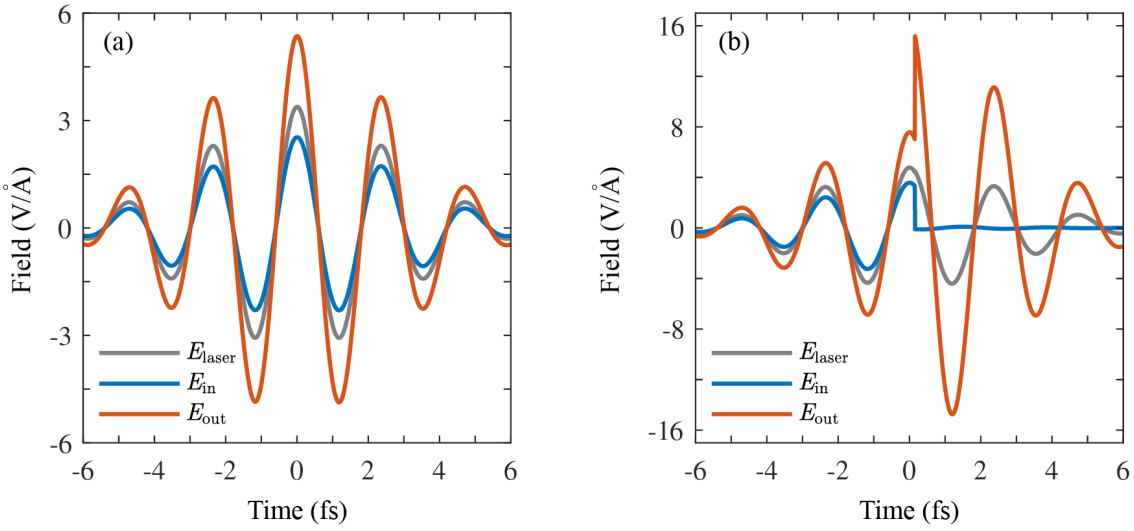

Figure 6.7: Electric field evolutions probed 0.1 nm inside (blue) and outside (red) the pole of the SiO_2 nanoparticle with laser peak intensity of (a) $1.5 \times 10^{14}\,\mathrm{W/cm^2}$ and (b) $3.0 \times 10^{14}\,\mathrm{W/cm^2}$. The grey lines present the driving field as a reference. The data were calculated with laser CEP $\varphi_{\text{ce}} = 0$.

According to the dipole approximation, the effective electric field (neglecting additional fields from free charges) along the laser polarization axis can be expressed as:

$$E_y = \alpha E_{\text{laser}}, \text{with} \begin{cases} \alpha_{|y|\geq R} = & 1 + \dfrac{\varepsilon - 1}{\varepsilon + 2} \dfrac{2R^3}{|y|^3} \\ \alpha_{|y|<R} = & \dfrac{3}{\varepsilon + 2} \end{cases} \tag{6.12}$$

Figure 6.7(a,b) show the electric field evolutions probed 0.1 nm inside (blue line) and outside (red line) the pole of the nanosphere with laser intensity $1.5 \times 10^{14}\,\mathrm{W/cm^2}$ and $3.0 \times 10^{14}\,\mathrm{W/cm^2}$, respectively. Neither significant modification on field enhancement nor phase shift can be observed at laser intensity below the turnover intensity. In contrast, with the laser intensity above the turnover intensity where the insulator-to-metal transition is occurring, the electric field inside the nanosphere is strongly attenuated, while the electric field on the pole of the nanosphere is further enhanced.

Figure 6.8 shows the laser intensity dependence of the maximum field enhancement factor α_{max}. When the peak intensities are below the turnover intensity, the maximum field enhancement remains nearly constant $\alpha_{\text{max}} \approx 1.54$ due to the minor impact of Kerr-effect and relatively low free-electron density (see blue line in Fig. 6.6(a)). Above the turnover intensity, the maximum field enhancement increases rapidly due to increased charge generation, and saturates at $\alpha_{\text{max}} = 3.3$ with peak intensity higher than $3 \times 10^{14}\,\mathrm{W/cm^2}$. The latter can be explained by the insulator-to-metal transition occurring before the peak of the

electric field at $t = 0$ (for $\varphi_{ce} = 0$) as shown in Fig. 6.8 (right axis). As a consequence, the cutoff remains at around 90-100 U_p for intensities above 3×10^{14} W/cm^2 (see Fig. 6.3(a)).

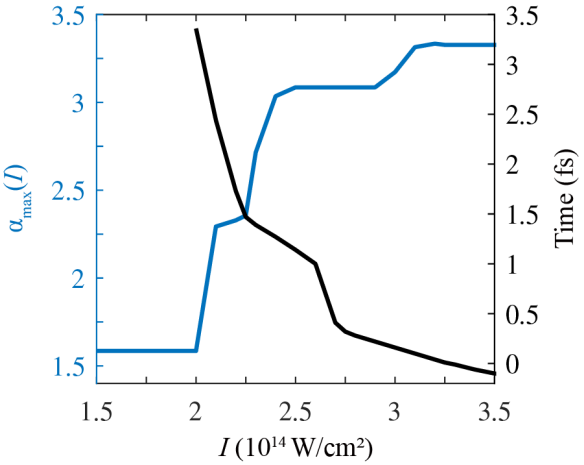

Figure 6.8: The maximum field enhancement (blue line, left axis) and insulator-to-metal transition time (black line, right axis) as a function of peak intensities. The data were calculated with CEP $\varphi_{ce} = 0$.

6.4 Conclusions

Few-cycle laser pulses have permitted to study SiO_2 under extreme conditions, where the solid remains intact during the interaction time. The photoemission energy spectra and CEP dependent asymmetry maps were presented. The field-driven ultrafast insulator-to-metal transition was monitored by CEP-dependent electron emission and comparison to semi-classical simulations. The results show that the rapid increase of free electron density inside the particles above a turnover intensity of 1.8×10^{14} W/cm^2 results in an increase of the electron cutoff energy up to 90-100 U_p and a modification of the sub-cycle acceleration dynamics. At intensities below the turnover intensity, the rescaled electron cutoff energy is constant at around 53 U_p, and agree with the reported results measured by VMI at moderate laser intensities.

We expect that a similar insulator-to-metal transition will occur for other materials at related intensities, where the dielectrically reduced field inside the particles reaches a sufficient intensity to induce a sufficient free electron density inside the sphere. More generally, our results indicate that accelerated electrons in few-cycle fields can elucidate the sub-cycle electronic dynamics of ultrafast phase transitions, not only for nanoparticles, but also for bulk solids, including thin films or other nanotargets, which are of relevance for few-cycle laser driven electron acceleration.

Appendix A

Data Archiving

The experimental raw data, evaluation files, and original figures can be found on the Data Archive Server of the Laboratory for Attosecond Physics at the Max Planck Institute of Quantum Optics: `/afs/rzg/mpq/lap/publication_archive`

Refer to `ReadMe.txt` for an overview and instructions how the codes are used. Note, that due to size constraints only preprocessed data is archived here. The complete raw data is available from Prof. Matthias Kling. The list below contains paths to all the relevant files given with respect to the root folder of the thesis. The canvases were prepared and exported by Adobe Illustrator CC. The figures were plotted by Matlab R2017b. The data used for figures are specified in the plot scripts.

Figure 2.1
- ▶ figure `Theory/figures/CEP_Up/CEP_Up-01.png`
- ▶ source `Theory/figures/CEP_Up/CEP_Up.ai`
- ▶ plot script (a) `Theory/figures/CEP_Up/plot_CEP.m`
- ▶ plot script (b) `Theory/figures/CEP_Up/plot_Up.m`

Figure 2.2
- ▶ figure `Theory/figures/ionization_mechanism/ionization_mechanism.ai`
- ▶ source `Theory/figures/ionization_mechanism/ionization_mechanism-01.png`

Figure 2.3
- ▶ figure `Theory/figures/three-step/three-step.png`

Figure 2.4
- ▶ figure `Theory/figures/SMM/SMM_cutoff-01.png`
- ▶ source `Theory/figures/SMM/SMM_cutoff.ai`
- ▶ plot script (a,b) `/Theory/figures/SMM/plot_SMM.m`

Figure 2.5
- ▶ figure Theory/figures/m3c_model/m3c.png

Figure 2.6
- ▶ figure Theory/figures/streaking_show/streaking_show-01.png
- ▶ source Theory/figures/streaking_show/streaking_show.ai

Figure 3.1
- ▶ figure ExpTech/figures/NP_source/TEM/TEM-01.png
- ▶ source ExpTech/figures/NP_source/TEM/TEM.ai

Figure 3.2
- ▶ figure ExpTech/figures/NP_source/aerosol_generator/aerosol_generator-01.png
- ▶ source ExpTech/figures/NP_source/aerosol_generator/aerosol_generator.ai

Figure 3.3
- ▶ figure ExpTech/figures/NP_source/aerodynamic_lens_cad/aerodynamic-01.png
- ▶ source ExpTech/figures/NP_source/aerodynamic_lens_cad/aerodynamic.ai

Figure 3.4
- ▶ figure ExpTech/figures/VMI/VMI_Simion/VMI_Simion-01.png
- ▶ source ExpTech/figures/VMI/VMI_Simion/VMI_Simion.ai
- ▶ source (a) ExpTech/figures/VMI/VMI_Simion/Eppik_style/image.tif
- ▶ source (b) ExpTech/figures/VMI/VMI_Simion/HEVMI/image.tif
- ▶ plot script (c) ExpTech/figures/VMI/VMI_Simion/HEVMI/vmi_resolution.m

Figure 3.5
- ▶ figure ExpTech/figures/VMI/VMI_calibration/vmi_calibration-01.png
- ▶ source ExpTech/figures/VMI/VMI_calibration/vmi_calibration.ai
- ▶ plot script (a,b) ExpTech/figures/VMI/VMI_calibration/run_calibrate.m

Figure 3.6
- ▶ figure ExpTech/figures/VMI/Marathon/plotMarathon-01.png
- ▶ source ExpTech/figures/VMI/Marathon/plotMarathon.ai
- ▶ plot script (a-c) ExpTech/figures/VMI/Marathon/plotMarathon.m

Figure 3.7
- ▶ figure ExpTech/figures/VMI/centroiding/centroiding-01.png
- ▶ source ExpTech/figures/VMI/centroiding/centroiding.ai
- ▶ plot script (a,b) ExpTech/figures/VMI/centroiding/rawImage/CameraPlotGas.m
- ▶ plot script (c) ExpTech/figures/VMI/centroiding/histogram/HistogramPlot.m

Figure 3.8
- ▶ figure ExpTech/figures/AS5/frontend_layer-01.png
- ▶ source ExpTech/figures/AS5/frontend_layer.ai
- ▶ plot script (b) ExpTech/figures/AS5/plot_CEP4.m
- ▶ plot script (c,d) ExpTech/figures/AS5/plot_FROG.m

Figure 3.9
- ▶ figure ExpTech/figures/laser_spectra/laser_spectra-01.png
- ▶ source ExpTech/figures/laser_spectra/laser_spectra.ai
- ▶ plot script (a) ExpTech/figures/laser_spectra/plotSpectra.m
- ▶ plot script (b) ExpTech/figures/laser_spectra/plot_wavelength.m

Figure 3.10
- ▶ figure ExpTech/figures/w2w_linear/setup_mz/w2w_setup-01.png
- ▶ source ExpTech/figures/w2w_linear/setup_mz/w2w_setup.ai
- ▶ plot script (a) ExpTech/figures/w2w_linear/setup_mz/spectra.m

Figure 3.11
- ▶ figure ExpTech/figures/w2w_linear/tgfrog/frog-01.png
- ▶ source ExpTech/figures/w2w_linear/tgfrog/frog.ai
- ▶ plot script (a) ExpTech/figures/w2w_linear/tgfrog/plot_frog.m

Figure 3.12
- ▶ figure ExpTech/figures/w2w_linear/stablization/stablization-01.png
- ▶ source ExpTech/figures/w2w_linear/stablization/stablization.ai
- ▶ plot script (a) ExpTech/figures/w2w_linear/stablization/plotFringes.m
- ▶ plot script (b) ExpTech/figures/w2w_linear/stablization/plotCompareStablized.m

Figure 3.13
- ▶ figure ExpTech/figures/w2w_linear/setup_exp/w2w_setup-01.png
- ▶ source ExpTech/figures/w2w_linear/setup_exp/w2w_setup.ai

▶ plot script (b,c) ExpTech/figures/w2w_linear/setup_exp/Beamprofile/plot_beamprofile.m

Figure 3.14

▶ figure ExpTech/figures/w2w_linear/photoemission_np/photoemission_np-01.png
▶ source ExpTech/figures/w2w_linear/photoemission_np/photoemission_np.ai
▶ plot script (a,b) ExpTech/figures/w2w_linear/photoemission_np/plot_histogram_images.m

Figure 3.15

▶ figure ExpTech/figures/w2w_linear/analysis_asy/analysis_asy-01.png
▶ source ExpTech/figures/w2w_linear/analysis_asy/analysis_asy.ai
▶ plot script (a-f) ExpTech/figures/w2w_linear/analysis_asy/plotAsyAnalysis.m

Figure 3.21

▶ figure ExpTech/figures/nanoPlasma/setup/setup_v5-01.png
▶ source ExpTech/figures/nanoPlasma/setup/setup_v5.ai

Figure 3.22

▶ figure ExpTech/figures/nanoPlasma/asymmetryMap_gas/asymmetry_gas-01.png
▶ source ExpTech/figures/nanoPlasma/asymmetryMap_gas/asymmetry_gas.ai
▶ plot script (a,b) ExpTech/figures/nanoPlasma/asymmetryMap_gas/plotAsymmetry.m

Figure 3.22

▶ figure ExpTech/figures/nanoPlasma/getCutoff/getCutoff-01.png
▶ source ExpTech/figures/nanoPlasma/getCutoff/getCutoff.ai
▶ plot script ExpTech/figures/nanoPlasma/getCutoff/plotGetCutoff.m

Figure 3.16

▶ figure ExpTech/figures/attosecond/attosecond_setup/attosecond_setup-01.png
▶ source ExpTech/figures/attosecond/attosecond_setup/attosecond_setup.ai
▶ source (a) ExpTech/figures/attosecond/attosecond_setup/XUV_IR.png
▶ source (b) ExpTech/figures/attosecond/attosecond_setup/spectra_IR_XUV.png

Figure 3.17

- ▶ figure ExpTech/figures/attosecond/attosecond_HHG/HHG_spectra-01.png
- ▶ source ExpTech/figures/attosecond/attosecond_HHG/HHG_spectra.ai
- ▶ plot script ExpTech/figures/attosecond/attosecond_HHG/HHG_spectra.m

Figure 3.18

- ▶ figure ExpTech/figures/attosecond/attosecond_FROG/frog_crab-01.png
- ▶ source ExpTech/figures/attosecond/attosecond_FROG/frog_crab.ai
- ▶ plot script (a) ExpTech/figures/attosecond/attosecond_FROG/plot_frog.m
- ▶ plot script (b) ExpTech/figures/attosecond/attosecond_FROG/intensity_phase.m

Figure 3.19

- ▶ figure ExpTech/figures/streaking_setup/setup_v2-01.png
- ▶ source ExpTech/figures/streaking_setup/setup_v2.ai

Figure 3.20

- ▶ figure ExpTech/figures/streaking_pixels/pixels-01.png
- ▶ source ExpTech/figures/streaking_pixels/pixels.ai
- ▶ plot script (a) ExpTech/figures/streaking_pixels/rawImage/CameraPlotGas.m
- ▶ plot script (b) ExpTech/figures/streaking_pixels/rawImage/CameraPlotNp.m
- ▶ plot script (c) ExpTech/figures/streaking_pixels/histogram/HistogramPlot.m

Figure 4.1

- ▶ figure streaking/figures/hit_statistics_model/hit_statistics_model-01.png
- ▶ source streaking/figures/hit_statistics_model/hit_statistics_model.ai
- ▶ model script streaking/figures/hit_statistics_model/hit_statistics_model.m
- ▶ plot script (b-d) streaking/figures/hit_statistics_model/plotCountRate.m

Figure 4.2

- ▶ figure streaking/figures/distanceMap/distanceMap-01.png
- ▶ source streaking/figures/distanceMap/distanceMap.ai
- ▶ plot script (a,b) streaking/figures/distanceMap/distanceMap/DistanceMapPlot.m
- ▶ plot script (c,d) streaking/figures/distanceMap/images/CurrentImagePlot.m

Figure 4.3

- ▶ figure streaking/figures/streaking_fit/v2/streaking-01.png
- ▶ source streaking/figures/streaking_fit/v2/streaking.ai
- ▶ plot script (a) streaking/figures/streaking_fit/v2/streak_contour_fit_gas.m

▶ plot script (b) `streaking/figures/streaking_fit/v2/streak_contour_fit_np.m`

Figure 4.4
▶ figure `streaking/figures/streaking_fit/fit_shift-01.png`
▶ source `streaking/figures/streaking_fit/fit_shift.ai`
▶ plot script (a) `streaking/figures/streaking_fit/v2/gas_plot_new.m`
▶ plot script (b) `streaking/figures/streaking_fit/v2/np_plot.m`
▶ plot script (c) `streaking/figures/streaking_fit/relativeShift/relativeShift.m`

Figure 4.5
▶ figure `streaking/figures/spectra_ratio/spectra_ratio-01.png`
▶ source `streaking/figures/spectra_ratio/spectra_ratio.ai`
▶ plot script (a,b) `streaking/figures/spectra_ratio/averageRatio/plotSpectra_Ratio.m`

Figure 4.6
▶ figure `streaking/figures/mie_xuv/field_delays_part1-01.png`
▶ source `streaking/figures/mie_xuv/field_delays_part1.ai`
▶ plot script (a) `streaking/figures/mie_xuv/mie_xuv.m`
▶ plot script (b) `streaking/figures/mie_xuv/plot_all_delays.m`
▶ plot script (c) `streaking/figures/mie_xuv/permittivity.m`

Figure 4.7
▶ figure `streaking/figures/MIE_XUV/field_delays_part2-01.png`
▶ source `streaking/figures/MIE_XUV/field_delays_part2.ai`
▶ plot script (a) `streaking/figures/MIE_XUV/plot_all_delays.m`
▶ plot script (b) `streaking/figures/MIE_XUV/plot_all_delays.m`

Figure 4.8
▶ figure `streaking/figures/chirped_xuv/chirped_XUV-01.png`
▶ source `streaking/figures/chirped_xuv/chirped_XUV.ai`
▶ source (a,b) `streaking/figures/chirped_xuv/chirped_XUV.png`

Figure 4.9
▶ figure `streaking/figures/MIE_XUV/field_delays_part3-01.png`
▶ source `streaking/figures/MIE_XUV/field_delays_part3.ai`
▶ source (a,b) `streaking/figures/MIE_XUV/plot_all_diameters.m`

Figure 4.10

▶ figure `streaking/figures/elastic_model/elastic_model-01.png`
▶ source `streaking/figures/elastic_model/elastic_model.ai`

Figure 4.11
▶ figure `streaking/figures/momentum_gain/momentum_gain-01.png`
▶ source `streaking/figures/momentum_gain/momentum_gain.ai`

Figure 4.12
▶ figure `streaking/figures/elastic_collision/elastic_collision-01.png`
▶ source `streaking/figures/elastic_collision/elastic_collision.ai`
▶ source (a-f) `streaking/figures/elastic_collision/elastic_collision.png`

Figure 4.13
▶ figure `streaking/figures/inelastic_scattering/inelastic_scattering-01.png`
▶ source `streaking/figures/inelastic_scattering/inelastic_scattering.ai`

Figure 4.14
▶ figure `streaking/figures/IMFP/IMFP-01.png`
▶ source `streaking/figures/IMFP/IMFP.ai`

Figure 5.1
▶ figure `Theory/figures/CEP_Up/CEP_Up-01.png`
▶ plot script `Theory/figures/CEP_Up/mie_parameter.m`

Figure 5.2
▶ figure `w2w_linear/figures/field_enhancement/field_enhancement-01.png`
▶ source `w2w_linear/figures/field_enhancement/field_enhancement.ai`
▶ plot script (a-d) `w2w_linear/figures/field_enhancement/plotMaxErMap_new.m`

Figure 5.3
▶ figure `w2w_linear/figures/surface_field_evolution/time_evolution-01.png`
▶ source `w2w_linear/figures/surface_field_evolution/time_evolution.ai`
▶ plot script (a-d) `w2w_linear/figures/surface_field_evolution/surface_field_evolution.m`

Figure 5.4

- ▶ figure `w2w_linear/figures/diff_image/diff_image-01.png`
- ▶ source `w2w_linear/figures/diff_image/diff_image.ai`
- ▶ plot script (a-c) `w2w_linear/figures/diff_image/plot_diff_image_60nm.m`
- ▶ plot script (d-f) `w2w_linear/figures/diff_image/plot_diff_image_300nm.m`

Figure 5.5

- ▶ figure `w2w_linear/figures/phase_dependence/phase_dependence-01.png`
- ▶ source `w2w_linear/figures/phase_dependence/phase_dependence.ai`
- ▶ plot script (a-c) `w2w_linear/figures/phase_dependence/plot_yield_fit_60nm_new.m`
- ▶ plot script (d-f) `w2w_linear/figures/phase_dependence/plot_yield_fit_300nm_new.m`

Figure 5.6

- ▶ figure `w2w_linear/figures/fermiFit/fermiFit-01.png`
- ▶ source `w2w_linear/figures/fermiFit/fermiFit.ai`
- ▶ plot script (a,b) `w2w_linear/figures/fermiFit/plot_fermiFit.m`

Figure 5.7

- ▶ figure `w2w_linear/figures/fft_filter/fft_filter-01.png`
- ▶ source `w2w_linear/figures/fft_filter/fft_filter.ai`
- ▶ plot script (a,b) `w2w_linear/figures/fft_filter/plot_output_Ke.m`

Figure 5.8

- ▶ figure `w2w_linear/figures/angle_phase_cutoff_new/angle_phase_cutoff-01.png`
- ▶ source `w2w_linear/figures/angle_phase_cutoff_new/angle_phase_cutoff.ai`
- ▶ plot script (a) `w2w_linear/figures/angle_phase_cutoff_new/exp60nm_0.05/plot_output_Ke.m`
- ▶ plot script (b) `w2w_linear/figures/angle_phase_cutoff_new/exp300nm_0.05/plot_output_Ke.m`
- ▶ plot script (c) `w2w_linear/figures/angle_phase_cutoff_new/exp300nm_0.5/plot_output_Ke.m`
- ▶ plot script (d) `w2w_linear/figures/angle_phase_cutoff_new/smm60nm_0.05/plot_output_Ke.m`
- ▶ plot script (e) `w2w_linear/figures/angle_phase_cutoff_new/smm300nm_0.05/plot_output_Ke.m`
- ▶ plot script (f) `w2w_linear/figures/angle_phase_cutoff_new/smm300nm_0.5/plot_output_Ke.m`

Figure 5.9

- ▶ figure `w2w_linear/figures/optimalAngle/optimalAngle-01.png`

- source `w2w_linear/figures/optimalAngle/optimalAngle.ai`
- plot script (a) `w2w_linear/figures/optimalAngle/optimalAngle.m`

Figure 5.10
- figure `w2w_linear/figures/cutoffPlots/cutoffPlots-01.png`
- source `w2w_linear/figures/cutoffPlots/cutoffPlots.ai`
- plot script (a) `w2w_linear/figures/cutoffPlots/cutoffAngle.m`

Figure 5.11
- figure `w2w_linear/figures/angle_phase_cutoff_new/compare_phase_all/compare_cutoff_map-01.png`
- source `w2w_linear/figures/angle_phase_cutoff_new/compare_phase_all/compare_cutoff_map.ai`
- plot script (a) `w2w_linear/figures/angle_phase_cutoff_new/smm300nm_0.05_propagation/plot_output_Ke.m`
- plot script (b) `w2w_linear/figures/angle_phase_cutoff_new/smm300nm_0.05_ionization/plot_output_Ke.m`

Figure 5.12
- figure `w2w_linear/figures/angle_phase_cutoff_new/compare_phase_all/compare_phase_all-01.png`
- source `w2w_linear/figures/angle_phase_cutoff_new/compare_phase_all/compare_phase_all.ai`
- plot script (a,b) `w2w_linear/figures/angle_phase_cutoff_new/compare_phase_all/compare_phase_all.m`

Figure 6.1
- figure `nanoPlasma/figures/spectra_SiO2/spectra_SiO2-01.png`
- source `nanoPlasma/figures/spectra_SiO2/spectra_SiO2.ai`
- plot script (a-c) `nanoPlasma/figures/spectra_SiO2/plot_spectra.m`

Figure 6.2
- figure `nanoPlasma/figures/asymmetry_SiO2/asyMap_SiO2-01.png`
- source `nanoPlasma/figures/asymmetry_SiO2/asyMap_SiO2.ai`
- plot script (a) `nanoPlasma/figures/asymmetry_SiO2/SiO2_asy_exp_1.m`
- plot script (b) `nanoPlasma/figures/asymmetry_SiO2/SiO2_asy_exp_2.m`
- plot script (c) `nanoPlasma/figures/asymmetry_SiO2/SiO2_asy_exp_3.m`
- plot script (d) `nanoPlasma/figures/asymmetry_SiO2/SiO2_asy_exp_4.m`

Figure 6.3
- ▶ figure `nanoPlasma/figures/cutoff_SiO2/cutoff_SiO2-01.png`
- ▶ source `nanoPlasma/figures/cutoff_SiO2/cutoff_SiO2.ai`
- ▶ plot script (a) `nanoPlasma/figures/cutoff_SiO2/plot_cutoff.m`
- ▶ plot script (b,c) `nanoPlasma/figures/cutoff_SiO2/plot_spectra.m`

Figure 6.4
- ▶ figure `nanoPlasma/figures/keldysh/keldysh_rate-01.png`
- ▶ source `nanoPlasma/figures/keldysh/keldysh_rate.ai`
- ▶ plot script `nanoPlasma/figures/keldysh/plot_keldysh.m`

Figure 6.5
- ▶ figure `nanoPlasma/figures/asymmetry_SiO2_M3C/asyMap-01.png`
- ▶ source `nanoPlasma/figures/asymmetry_SiO2_M3C/asyMap.ai`
- ▶ plot script (a-c) `nanoPlasma/figures/asymmetry_SiO2_M3C/plot_asy.m`

Figure 6.6
- ▶ figure `nanoPlasma/figures/CB_density_fields/analysis-01.png`
- ▶ source `nanoPlasma/figures/CB_density_fields/analysis.ai`
- ▶ plot script (a-d) `nanoPlasma/figures/CB_density_fields/plot_data.m`

Figure 6.6
- ▶ figure `nanoPlasma/figures/permittivity/permittivity-01.png`
- ▶ source `nanoPlasma/figures/permittivity/permittivity.ai`
- ▶ plot script (a,b) `nanoPlasma/figures/permittivity/plot_permittivity.m`

Figure 6.7
- ▶ figure `nanoPlasma/figures/fields/fields-01.png`
- ▶ source `nanoPlasma/figures/fields/fields.ai`
- ▶ plot script (a-c) `nanoPlasma/figures/fields/plot_fields.m`

Figure 6.8
- ▶ figure `nanoPlasma/figures/enhancement/enhancement-01.png`
- ▶ source `nanoPlasma/figures/enhancement/enhancement.ai`
- ▶ plot script (a-c) `nanoPlasma/figures/enhancement/plot_data.m`

Bibliography

[1] P. Krehl and S. Engemann, "August Toepler - The first who visualized shock waves," *Shock Waves*, vol. 5, pp. 1–18, 1995.

[2] A. H. Zewail, *Femtochemistry: Ultrafast Dynamics of the Chemical Bond*, vol. 3 of *World Scientific Series in 20th Century Chemistry*. World Scientific Publishing Company, 1994.

[3] A. H. Zewail, "Femtochemistry: Atomic-Scale Dynamics of the Chemical Bond," *The Journal of Physical Chemistry A*, vol. 104, pp. 5660–5694, 2000.

[4] M. Hentschel, R. Kienberger, C. Spielmann, G. A. Reider, N. Milosevic, T. Brabec, P. Corkum, U. Heinzmann, M. Drescher, and F. Krausz, "Attosecond metrology," *Nature*, vol. 414, pp. 509–513, 2001.

[5] E. Goulielmakis, M. Schultze, M. Hofstetter, V. S. Yakovlev, J. Gagnon, M. Uiberacker, A. L. Aquila, E. M. Gullikson, D. T. Attwood, R. Kienberger, F. Krausz, and U. Kleineberg, "Single-cycle nonlinear optics," *Science*, vol. 320, p. 1614, 2008.

[6] X. Feng, S. Gilbertson, H. Mashiko, H. Wang, S. D. Khan, M. Chini, Y. Wu, K. Zhao, and Z. Chang, "Generation of isolated attosecond pulses with 20 to 28 femtosecond lasers," *Physical Review Letters*, vol. 103, p. 183901, 2009.

[7] E. Goulielmakis, M. Uiberacker, R. Kienberger, A. Baltuška, V. Yakovlev, A. Scrinzi, T. Westerwalbesloh, U. Kleineberg, U. Heinzmann, M. Drescher, and F. Krausz, "Direct measurement of light waves," *Science*, vol. 305, pp. 1267–1269, 2004.

[8] G. Sansone, E. Benedetti, F. Calegari, C. Vozzi, L. Avaldi, R. Flammini, L. Poletto, P. Villoresi, C. Altucci, R. Velotta, S. Stagira, S. De Silvestri, and M. Nisoli, "Isolated single-cycle attosecond pulses," *Science*, vol. 314, pp. 443–446, 2006.

[9] F. Krausz and M. I. Stockman, "Attosecond metrology: from electron capture to future signal processing," *Nature Photonics*, vol. 8, pp. 205–213, 2014.

[10] F. Calegari, G. Sansone, S. Stagira, C. Vozzi, and M. Nisoli, "Advances in attosecond science," *Journal of Physics B: Atomic, Molecular and Optical Physics*, vol. 49, p. 062001, 2016.

[11] P. Balling and J. Schou, "Femtosecond-laser ablation dynamics of dielectrics: Basics and applications for thin films," *Reports on Progress in Physics*, vol. 76, p. 036502, 2013.

[12] L. H. Toburen, S. L. McLawhorn, R. a. McLawhorn, K. D. Carnes, M. Dingfelder, and J. L. Shinpaugh, "Electron emission from amorphous solid water induced by passage of energetic protons and fluorine ions.," *Radiation research*, vol. 174, pp. 107–118, 2010.

[13] B. C. Garrett, D. A. Dixon, D. M. Camaioni, D. M. Chipman, M. A. Johnson, C. D. Jonah, G. A. Kimmel, J. H. Miller, T. N. Rescigno, P. J. Rossky, S. S. Xantheas, S. D. Colson, A. H. Laufer, D. Ray, P. F. Barbara, D. M. Bartels, K. H. Becker, K. H. Bowen, S. E. Bradforth, I. Carmichael, J. V. Coe, L. R. Corrales, J. P. Cowin, M. Dupuis, K. B. Eisenthal, J. A. Franz, M. S. Gutowski, K. D. Jordan, B. D. Kay, J. A. LaVerne, S. V. Lymar, T. E. Madey, C. W. McCurdy, D. Meisel, S. Mukamel, A. R. Nilsson, T. M. Orlando, N. G. Petrik, S. M. Pimblott, J. R. Rustad, G. K. Schenter, S. J. Singer, A. Tokmakoff, L. S. Wang, C. Wittig, and T. S. Zwier, "Role of water in electron-initiated processes and radical chemistry: Issues and scientific advances," *Chemical Reviews*, vol. 105, pp. 355–389, 2005.

[14] C. Caleman, C. Ortiz, E. Marklund, F. Bultmark, M. Gabrysch, F. G. Parak, J. Hajdu, M. Klintenberg, and N. Tîmneanu, "Radiation damage in biological material: Electronic properties and electron impact ionization in urea," *Europhysics Letters*, vol. 85, p. 18005, 2009.

[15] S. H. Pandya, B. G. Vaishnav, and K. N. Joshipura, "Electron inelastic mean free paths in solids: A theoretical approach," *Chinese Physics B*, vol. 21, p. 093402, 2012.

[16] C. J. Powell, "Inelastic Scattering of Kilovolt Electrons by Solids and Liquids," *Health Physics*, vol. 13, pp. 1265–1275, 1967.

[17] M. Goldmann, J. Miguel-Sánchez, A. H. West, B. L. Yoder, and R. Signorell, "Electron mean free path from angle-dependent photoelectron spectroscopy of aerosol particles," *Journal of Chemical Physics*, vol. 142, p. 224304, 2015.

[18] S. Neppl, R. Ernstorfer, E. M. Bothschafter, A. L. Cavalieri, D. Menzel, J. V. Barth, F. Krausz, R. Kienberger, and P. Feulner, "Attosecond time-resolved photoemission from core and valence states of magnesium," *Physical Review Letters*, vol. 109, p. 087401, 2012.

[19] W. A. Okell, T. Witting, D. Fabris, C. A. Arrell, J. Hengster, S. Ibrahimkutty, A. Seiler, M. Barthelmess, S. Stankov, D. Y. Lei, Y. Sonnefraud, M. Rahmani, T. Uphues, S. A. Maier, J. P. Marangos, and J. W. G. Tisch, "Temporal broadening of attosecond photoelectron wavepackets from solid surfaces," *Optica*, vol. 2, pp. 383–387, 2015.

[20] R. Locher, L. Castiglioni, M. Lucchini, M. Greif, L. Gallmann, J. Osterwalder, M. Hengsberger, and U. Keller, "Energy-dependent photoemission delays from noble metal surfaces by attosecond interferometry," *Optica*, vol. 2, pp. 405–410, 2015.

[21] A. G. Borisov, D. Sánchez-Portal, A. K. Kazansky, and P. M. Echenique, "Resonant and nonresonant processes in attosecond streaking from metals," *Physical Review B - Condensed Matter and Materials Physics*, vol. 87, p. 121110, 2013.

[22] C. H. Zhang and U. Thumm, "Attosecond photoelectron spectroscopy of metal surfaces," *Journal of Physics: Conference Series*, vol. 102, p. 123601, 2009.

[23] F. Kelkensberg, A. F. Koenderink, and M. J. Vrakking, "Attosecond streaking in a nano-plasmonic field," *New Journal of Physics*, vol. 14, p. 93034, 2012.

[24] J. Li, E. Saydanzad, and U. Thumm, "Retrieving plasmonic near-field information: A quantum-mechanical model for streaking photoelectron spectroscopy of gold nanospheres," *Physical Review A*, vol. 94, p. 051401, 2016.

[25] J. S. Prell, L. J. Borja, D. M. Neumark, and S. R. Leone, "Simulation of attosecond-resolved imaging of the plasmon electric field in metallic nanoparticles," *Annalen der Physik*, vol. 525, pp. 151–161, 2013.

[26] S. Neppl, R. Ernstorfer, A. L. Cavalieri, C. Lemell, G. Wachter, E. Magerl, E. M. Bothschafter, M. Jobst, M. Hofstetter, U. Kleineberg, J. V. Barth, D. Menzel, J. Burgdorfer, P. Feulner, F. Krausz, R. Kienberger, J. Burgdörfer, P. Feulner, F. Krausz, and R. Kienberger, "Direct observation of electron propagation and dielectric screening on the atomic length scale," *Nature*, vol. 517, pp. 342–346, 2015.

[27] Q. Liao and U. Thumm, "Quantum-mechanical simulation of attosecond streaked photoemission from Mg-covered W(110) surfaces," *Journal of Physics: Conference Series*, vol. 92, p. 031401, 2015.

[28] F. Krausz and M. Ivanov, "Attosecond physics," *Reviews of Modern Physics*, vol. 81, pp. 163–234, 2009.

[29] S. De, I. Znakovskaya, D. Ray, F. Anis, N. G. Johnson, I. A. Bocharova, M. Magrakvelidze, B. D. Esry, C. L. Cocke, I. V. Litvinyuk, and M. F. Kling, "Field-Free Orientation of CO Molecules by Femtosecond Two-Color Laser Fields," *Physical Review Letters*, vol. 103, p. 153002, 2009.

[30] M. Förster, T. Paschen, M. Krüger, C. Lemell, G. Wachter, F. Libisch, T. Madlener, J. Burgdörfer, and P. Hommelhoff, "Two-color coherent control of femtosecond above-threshold photoemission from a Tungsten nanotip," *Physical Review Letters*, vol. 117, p. 217601, 2016.

[31] L. Seiffert, T. Paschen, P. Hommelhoff, and T. Fennel, "High-order above-threshold photoemission from nanotips controlled with two-color laser fields," *Journal of Physics B: Atomic, Molecular and Optical Physics*, vol. 51, p. 134001, 2018.

[32] S. Skruszewicz, J. Tiggesbäumker, K. H. Meiwes-Broer, M. Arbeiter, T. Fennel, and D. Bauer, "Two-Color Strong-Field Photoelectron Spectroscopy and the Phase of the Phase," *Physical Review Letters*, vol. 115, p. 043001, 2015.

[33] N. Eicke and M. Lein, "Extracting trajectory information from two-color strong-field ionization," *Journal of Modern Optics*, vol. 64, pp. 981–986, 2017.

[34] S. Kerbstadt, D. Pengel, D. Johannmeyer, L. Englert, T. Bayer, and M. Wollenhaupt, "Control of photoelectron momentum distributions by bichromatic polarization-shaped laser fields," *New Journal of Physics*, vol. 19, p. 103017, 2017.

[35] D. Shafir, Y. Mairesse, D. M. Villeneuve, P. B. Corkum, and N. Dudovich, "Atomic wavefunctions probed through strong-field light-matterinteraction," *Nature Physics*, vol. 5, pp. 412–416, 2009.

[36] K. Lin, X. Jia, Z. Yu, F. He, J. Ma, H. Li, X. Gong, Q. Song, Q. Ji, W. Zhang, H. Li, P. Lu, H. Zeng, J. Chen, and J. Wu, "Comparison Study of Strong-Field Ionization of Molecules and Atoms by Bicircular Two-Color Femtosecond Laser Pulses," *Physical Review Letters*, vol. 119, p. 203202, 2017.

[37] X. Gong, C. Lin, F. He, Q. Song, K. Lin, Q. Ji, W. Zhang, J. Ma, P. Lu, Y. Liu, H. Zeng, W. Yang, and J. Wu, "Energy-Resolved Ultrashort Delays of Photoelectron Emission Clocked by Orthogonal Two-Color Laser Fields," *Physical Review Letters*, vol. 118, p. 143203, 2017.

[38] N. Dudovich, O. Smirnova, J. Levesque, Y. Mairesse, M. Y. Ivanov, D. M. Villeneuve, and P. B. Corkum, "Measuring and controlling the birth of attosecond XUV pulses," *Nature Physics*, vol. 2, pp. 781–786, 2006.

[39] M. Kling and F. Krausz, "Attoscience: An attosecond stopwatch," *Nature Physics*, vol. 4, pp. 515–516, 2008.

[40] E. Goulielmakis, V. S. Yakovlev, A. L. Cavalieri, M. Uiberacker, V. Pervak, A. Apolonski, R. Kienberger, U. Kleineberg, and F. Krausz, "Attosecond Control and Measurement:," *Science*, vol. 317, pp. 769–775, 2007.

[41] M. F. Ciappina, J. A. Pérez-Hernández, A. S. Landsman, W. A. Okell, S. Zherebtsov, B. Förg, J. Schötz, L. Seiffert, T. Fennel, T. Shaaran, T. Zimmermann, A. Chacón, R. Guichard, A. Zaïr, J. W. G. Tisch, J. P. Marangos, T. Witting, A. Braun, S. A. Maier, L. Roso, M. Krüger, P. Hommelhoff, M. F. Kling, F. Krausz, M. Lewenstein, A. Za\"\ir, J. W. G. Tisch, J. P. Marangos, T. Witting, A. Braun, S. A.

Maier, L. Roso, M. Krüger, P. Hommelhoff, M. F. Kling, F. Krausz, and M. Lewenstein, "Attosecond physics at the nanoscale," *Reports on Progress in Physics*, vol. 80, p. 054401, 2017.

[42] L. Seiffert, Q. Liu, S. Zherebtsov, A. Trabattoni, P. Rupp, M. C. Castrovilli, M. Galli, F. Submann, K. Wintersperger, J. Stierle, G. Sansone, L. Poletto, F. Frassetto, I. Halfpap, V. Mondes, C. Graf, E. Ruhl, F. Krausz, M. Nisoli, T. Fennel, F. Calegari, and M. F. Kling, "Attosecond chronoscopy of electron scattering in dielectric nanoparticles," *Nature Physics*, vol. 13, pp. 766–770, 2017.

[43] D. K. Gramotnev and S. I. Bozhevolnyi, "Nanofocusing of electromagnetic radiation," *Nature Photonics*, vol. 8, pp. 13–22, 2014.

[44] S. A. Maier and H. A. Atwater, "Plasmonics: Localization and guiding of electromagnetic energy in metal/dielectric structures," *Journal of Applied Physics*, vol. 98, p. 011101, 2005.

[45] V. Apalkov and M. I. Stockman, "Metal nanofilm in strong ultrafast optical fields," *Physical Review B - Condensed Matter and Materials Physics*, vol. 88, p. 245438, 2013.

[46] M. I. Stockman, K. Kneipp, S. I. Bozhevolnyi, S. S, and A. Datta, "Roadmap on plasmonics," *Journal of Optics*, vol. 20, p. 043001, 2018.

[47] G. Vampa, H. Fattahi, J. Vuckovic, and F. Krausz, "Nonlinear optics: Attosecond nanophotonics," *Nature Photonics*, vol. 11, pp. 210–212, 2017.

[48] F. Süßmann, L. Seiffert, S. Zherebtsov, V. Mondes, J. Stierle, M. Arbeiter, J. Plenge, P. Rupp, C. Peltz, A. Kessel, S. A. Trushin, B. Ahn, D. Kim, C. Graf, E. Rühl, M. F. Kling, and T. Fennel, "Field propagation-induced directionality of carrier-envelope phase-controlled photoemission from nanospheres," *Nature Communications*, vol. 6, p. 7944, 2015.

[49] D. Ray, F. He, S. De, W. Cao, H. Mashiko, P. Ranitovic, K. P. Singh, I. Znakovskaya, U. Thumm, G. G. Paulus, M. F. Kling, I. V. Litvinyuk, and C. L. Cocke, "Ion-energy dependence of asymmetric dissociation of D2 by a two-color laser field," *Physical Review Letters*, vol. 103, p. 223201, 2009.

[50] J. Mauritsson, J. M. Dahlström, E. Mansten, and T. Fordell, "Sub-cycle control of attosecond pulse generation using two-colour laser fields," *Journal of Physics B: Atomic, Molecular and Optical Physics*, vol. 42, p. 134003, 2009.

[51] O. Kfir, P. Grychtol, E. Turgut, R. Knut, D. Zusin, D. Popmintchev, T. Popmintchev, H. Nembach, J. M. Shaw, A. Fleischer, H. Kapteyn, M. Murnane, and O. Cohen, "Generation of bright phase-matched circularly-polarized extreme ultraviolet high harmonics," *Nature Photonics*, vol. 9, pp. 99–105, 2015.

[52] B. Sheehy, B. Walker, and L. F. DiMauro, "Phase control in the two-color photodissociation of HD+.pdf," *Physical Review Letters*, vol. 74, p. 4799, 1995.

[53] T. Otobe, M. Yamagiwa, J.-I. Iwata, K. Yabana, T. Nakatsukasa, and G. F. Bertsch, "First-principles electron dynamics simulation for optical breakdown of dielectrics under an intense laser field," *Physical Review B*, vol. 77, p. 165104, 2008.

[54] T. T. Luu, M. Garg, S. Y. Kruchinin, A. Moulet, M. T. Hassan, E. Goulielmakis, S. Yu. Kruchinin, A. Moulet, M. T. Hassan, and E. Goulielmakis, "Extreme ultraviolet high-harmonic spectroscopy of solids," *Nature*, vol. 521, pp. 498–502, 2015.

[55] S. Han, H. Kim, Y. J. Y. W. Y.-J. W. Kim, Y. J. Y. W. Y.-J. W. Kim, S. W. S.-W. S. Kim, I.-Y. I. Y. Park, and S. W. S.-W. S. Kim, "High-harmonic generation by field enhanced femtosecond pulses in metal-sapphire nanostructure," *Nature Communications*, vol. 7, p. 13105, 2016.

[56] M. Durach, A. Rusina, M. F. Kling, and M. I. Stockman, "Predicted ultrafast dynamic metallization of dielectric nanofilms by strong single-cycle optical fields," *Physical Review Letters*, vol. 107, p. 086602, 2011.

[57] M. Schultze, E. M. Bothschafter, A. Sommer, S. Holzner, W. Schweinberger, M. Fiess, M. Hofstetter, R. Kienberger, V. Apalkov, V. S. Yakovlev, M. I. Stockman, and F. Krausz, "Controlling dielectrics with the electric field of light," *Nature*, vol. 493, pp. 75–78, 2013.

[58] M. Schultze, K. Ramasesha, C. D. Pemmaraju, S. A. Sato, D. Whitmore, A. Gandman, J. S. Prell, L. J. Borja, D. Prendergast, K. Yabana, D. M. Neumark, and S. R. Leone, "Attosecond band-gap dynamics in silicon," *Science*, vol. 346, pp. 1348–1352, 2014.

[59] A. Schiffrin, T. Paasch-Colberg, N. Karpowicz, V. Apalkov, D. Gerster, S. Mühlbrandt, M. Korbman, J. Reichert, M. Schultze, S. Holzner, J. V. Barth, R. Kienberger, R. Ernstorfer, V. S. Yakovlev, M. I. Stockman, and F. Krausz, "Optical-field-induced current in dielectrics," *Nature*, vol. 493, pp. 70–74, 2013.

[60] M. Durach, A. Rusina, M. F. Kling, and M. I. Stockman, "Metallization of nanofilms in strong adiabatic electric fields," *Physical Review Letters*, vol. 105, p. 086803, 2010.

[61] X. Jing, Y. Tian, J. Zhang, S. Chen, Y. Jin, J. Shao, and Z. Fan, "Modeling validity of femtosecond laser breakdown in wide bandgap dielectrics," *Applied Surface Science*, vol. 258, pp. 4741–4749, 2012.

[62] K. Starke, D. Ristau, H. Welling, T. V. Amotchkina, M. Trubetskov, A. A. Tikhonravov, and A. S. Chirkin, "Investigations in the nonlinear behavior of dielectrics by using ultrashort pulses (Best Oral Presentation)," *Proceedings of SPIE*, vol. 5273, pp. 501–514, 2004.

[63] T. Gorkhover, S. Schorb, R. Coffee, M. Adolph, L. Foucar, D. Rupp, A. Aquila, J. D. Bozek, S. W. Epp, B. Erk, L. Gumprecht, L. Holmegaard, A. Hartmann, R. Hartmann, G. Hauser, P. Holl, A. Hömke, P. Johnsson, N. Kimmel, K.-U. U. Kühnel, M. Messerschmidt, C. Reich, A. Rouzée, B. Rudek, C. Schmidt, J. Schulz, H. Soltau, S. Stern, G. Weidenspointner, B. White, J. Küpper, L. Strüder, I. Schlichting, J. Ullrich, D. Rolles, A. Rudenko, T. Möller, and C. Bostedt, "Femtosecond and nanometre visualization of structural dynamics in superheated nanoparticles," *Nature Photonics*, vol. 10, pp. 93–97, 2016.

[64] K. R. Ferguson, M. Bucher, T. Gorkhover, S. Boutet, H. Fukuzawa, J. E. Koglin, Y. Kumagai, A. Lutman, A. Marinelli, M. Messerschmidt, K. Nagaya, J. Turner, K. Ueda, G. J. Williams, P. H. Bucksbaum, and C. Bostedt, "Transient lattice contraction in the solid-to-plasma transition," *Science Advances*, vol. 2, p. e1500837, 2016.

[65] C. Peltz, C. Varin, T. Brabec, and T. Fennel, "Time-Resolved X-Ray Imaging of Anisotropic Nanoplasma Expansion," *Physical Review Letters*, vol. 113, p. 133401, 2014.

[66] S. Zherebtsov, T. Fennel, J. Plenge, E. Antonsson, I. Znakovskaya, I. Ahmad, A. Wirth, O. Herrwerth, S. A. Trushin, V. Pervak, S. Karsch, M. J. J. Vrakking, B. Langer, C. Graf, M. I. Stockman, F. Krausz, E. Rühl, M. F. Kling, F. Sümann, C. Peltz, I. Ahmad, S. A. Trushin, V. Pervak, S. Karsch, M. J. J. Vrakking, B. Langer, C. Graf, M. I. Stockman, F. Krausz, E. Rühl, and M. F. Kling, "Controlled near-field enhanced electron acceleration from dielectric nanospheres with intense few-cycle laser fields," *Nature Physics*, vol. 7, pp. 656–662, 2011.

[67] P. Rupp, L. Seiffert, Q. Liu, F. Süßmann, B. Ahn, B. Förg, C. G. Schäfer, M. Gallei, V. Mondes, A. Kessel, S. Trushin, C. Graf, E. Rühl, J. Lee, M. S. Kim, D. E. Kim, T. Fennel, M. F. Kling, and S. Zherebtsov, "Quenching of material dependence in few-cycle driven electron acceleration from nanoparticles under many-particle charge interaction," *Journal of Modern Optics*, vol. 64, p. 995, 2017.

[68] S. Zherebtsov, F. Süßmann, C. Peltz, J. Plenge, K. J. Betsch, I. Znakovskaya, A. S. Alnaser, N. G. Johnson, M. Kübel, A. Horn, V. Mondes, C. Graf, S. A. Trushin, A. Azzeer, M. J. J. Vrakking, G. G. Paulus, F. Krausz, E. Rühl, T. Fennel, and M. F. Kling, "Carrier-envelope phase-tagged imaging of the controlled electron acceleration from SiO2nanospheres in intense few-cycle laser fields," *New Journal of Physics*, vol. 14, p. 075010, 2012.

[69] M. Krüger, M. Schenk, and P. Hommelhoff, "Attosecond control of electrons emitted from a nanoscale metal tip," *Nature*, vol. 475, pp. 78–81, 2011.

[70] G. Herink, D. R. Solli, M. Gulde, and C. Ropers, "Field-driven photoemission from nanostructures quenches the quiver motion," *Nature*, vol. 483, pp. 190–193, 2012.

[71] B. Piglosiewicz, S. Schmidt, D. J. Park, J. Vogelsang, P. Groß, C. Manzoni, P. Farinello, G. Cerullo, C. Lienau, P. Grosz, C. Manzoni, P. Farinello, G. Cerullo, and C. Lienau, "Carrier-envelope phase effects on the strong-field photoemission of electrons from metallic nanostructures," *Nature Photonics*, vol. 8, pp. 37–42, 2014.

[72] J. Vogelsang, J. Robin, B. J. Nagy, P. Dombi, D. Rosenkranz, M. Schiek, P. Groß, and C. Lienau, "Ultrafast Electron Emission from a Sharp Metal Nanotaper Driven by Adiabatic Nanofocusing of Surface Plasmons," *Nano Letters*, vol. 15, pp. 4685–4691, 2015.

[73] H. Yanagisawa, S. Schnepp, C. Hafner, M. Hengsberger, D. Kim, M. F. Kling, A. Landsman, L. Gallmann, and J. Osterwalder, "Delayed electron emission channel in strong-field driven tunneling from a metallic nanotip," *Scientific Reports*, vol. 6, p. 35877, 2016.

[74] P. Dombi, A. Hörl, P. Rácz, I. Márton, A. Trügler, J. R. Krenn, and U. Hohenester, "Ultrafast strong-field photoemission from plasmonic nanoparticles," *Nano Letters*, vol. 13, pp. 674–678, 2013.

[75] L. Seiffert, P. Henning, P. Rupp, S. Zherebtsov, P. Hommelhoff, M. F. Kling, and T. Fennel, "Trapping field assisted backscattering in strong- field photoemission from dielectric nanospheres," *Journal of Modern Optics*, vol. 64, pp. 1096–1103, 2017.

[76] L. Seiffert, F. Süßmann, S. Zherebtsov, P. Rupp, C. Peltz, E. Rühl, M. F. Kling, and T. Fennel, "Competition of single and double rescattering in the strong-field photoemission from dielectric nanospheres," *Applied Physics B: Lasers and Optics*, vol. 122, p. 101, 2016.

[77] M. F. Kling, C. Siedschlag, A. J. Verhoef, J. I. Khan, M. Schultze, T. Uphues, Y. Ni, M. Uiberacker, M. Drescher, F. Krausz, and M. J. Vrakking, "Control of electron localization in molecular dissociation," *Science*, vol. 312, pp. 246–248, 2006.

[78] S. Pabst, "Atomic and molecular dynamics triggered by ultrashort light pulses on the atto- to picosecond time scale," *European Physical Journal: Special Topics*, vol. 221, pp. 1–71, 2013.

[79] M. Wollenhaupt and T. Baumert, "Ultrafast laser control of electron dynamics in atoms, molecules and solids," *Faraday Discussions*, vol. 153, pp. 9–26, 2011.

[80] T. Brabec and F. Krausz, "Intense few-cycle laser fields: Frontiers of nonlinear optics," *Reviews of Modern Physics*, vol. 72, pp. 545–591, 2000.

[81] F. Frank, C. Arrell, T. Witting, W. A. Okell, J. McKenna, J. S. Robinson, C. A. Haworth, D. Austin, H. Teng, I. A. Walmsley, J. P. Marangos, and J. W. Tisch, "Invited review article: Technology for attosecond science," *Review of Scientific Instruments*, vol. 83, p. 071101, 2012.

[82] M. Meckel, D. Comtois, D. Zeidler, A. Staudte, D. Pavičić, H. C. Bandulet, H. Pépin, J. C. Kieffer, R. Dörner, D. M. Villeneuve, and P. B. Corkum, "Laser-induced electron tunneling and diffraction," *Science*, vol. 320, pp. 1478–1482, 2008.

[83] A. J. Verhoef, A. Fernández, M. Lezius, K. O'Keeffe, M. Uiberacker, and F. Krausz, "Few-cycle carrier envelope phase-dependent stereo detection of electrons," *Optics Letters*, vol. 31, pp. 3520–3522, 2006.

[84] T. Rathje, N. G. Johnson, M. Möller, F. Süßmann, D. Adolph, M. Kübel, R. Kienberger, M. F. Kling, G. G. Paulus, and A. M. Sayler, "Review of attosecond resolved measurement and control via carrierenvelope phase tagging with above-threshold ionization," *Journal of Physics B: Atomic, Molecular and Optical Physics*, vol. 45, p. 074003, 2012.

[85] T. Paasch-Colberg, A. Schiffrin, N. Karpowicz, S. Kruchinin, Ö. Sağlam, S. Keiber, O. Razskazovskaya, S. Mühlbrandt, A. Alnaser, M. Kübel, V. Apalkov, D. Gerster, J. Reichert, T. Wittmann, J. V. Barth, M. I. Stockman, R. Ernstorfer, V. S. Yakovlev, R. Kienberger, and F. Krausz, "Solid-state light-phase detector," *Nature Photonics*, vol. 8, pp. 214–218, 2014.

[86] P. Agostini and L. F. DiMauro, "The physics of attosecond light pulses," *Reports on Progress in Physics*, vol. 67, pp. 813–855, 2004.

[87] P. H. Bucksbaum, "The future of attosecond spectroscopy," *Science*, vol. 317, pp. 766–769, 2007.

[88] L. Gallmann, C. Cirelli, and U. Keller, "Attosecond Science: Recent Highlights and Future Trends," *Annual Review of Physical Chemistry*, vol. 63, pp. 447–469, 2012.

[89] P. Hommelhoff, M. F. Kling, and M. I. Stockman, "Ultrafast phenomena on the nanoscale," *Annalen der Physik*, vol. 525, pp. A13–A14, 2013.

[90] M. Protopapas, P. L. Knight, and C. H. Keitel, "Atomic physics with super-high intensity lasers," *Reports on Progress in Physics*, vol. 60, pp. 389–486, 1999.

[91] A. Baltuška, M. Uiberacker, E. Goulielmakis, R. Kienberger, V. S. Yakovlev, T. Udem, T. W. Hänsch, and F. Krausz, "Phase-Controlled Amplification of Few-Cycle Laser Pulses," *IEEE Journal on Selected Topics in Quantum Electronics*, vol. 9, pp. 972–989, 2003.

[92] N. B. Delone and V. P. Krainov, *Multiphoton processes in atoms*. Springer, 1994.

[93] G. Mainfray and G. Manus, "Multiphoton ionization of atoms," *Reports on Progress in Physics*, vol. 54, pp. 1333–1372, 1991.

[94] F. Fabre, G. Petite, P. Agostini, and M. Clement, "Multiphoton above-threshold ionisation of xenon at 0.53 and 1.06 um," *Journal of Physics B: Atomic and Molecular Physics*, vol. 15, pp. 1353–1369, 1982.

[95] G. Petite, F. Fabre, P. Agostini, M. Crance, and M. Aymar, "Nonresonant multiphoton ionization of cesium in strong fields: Angular distributions and above-threshold ionization," *Physical Review A*, vol. 29, pp. 2678–2689, 1984.

[96] P. Agostini, F. Fabre, G. Mainfray, G. Petite, and N. K. Rahman, "Free-Free Transitions Following Six-Photon Ionization of Xenon Atoms," *Physical Review Letters*, vol. 42, pp. 1127–1130, 1979.

[97] P. Kruit, J. Kimman, H. G. Muller, and M. J. van der Wiel, "Electron spectra from multiphoton ionization of xenon at 1064, 532, and 355 nm," *Physical Review A*, vol. 28, pp. 248–255, 1983.

[98] Y. Gontier and M. Trahin, "Energetic electron generation by multiphoton absorption," *Journal of Physics B: Atomic and Molecular Physics*, vol. 13, pp. 4383–4390, 1980.

[99] M. V. Ammosov, N. B. Delone, and V. P. Krainov, "Tunnel Ionization Of Complex Atoms And Atomic Ions In Electromagnetic Field," *Journal of Experimental and Theoretical Physics*, vol. 64, pp. 2008–2013, 1986.

[100] S. Augst, D. D. Meyerhofer, D. Strickland, and S. L. Chint, "Laser ionization of noble gases by Coulomb-barrier suppression," *Journal of the Optical Society of America B*, vol. 8, pp. 858–867, 1991.

[101] M. V. Ammosov, V. P. Krainov, V. M. Ristic, P. A. Golovinsky, and I. Y. Kiyan, "Tunneling ionization of atoms and atomic ions in an intense laser field with a nonhomogeneous space–time distribution," *Journal of the Optical Society of America B*, vol. 9, pp. 1225–1230, 2008.

[102] C. R. McDonald, G. Orlando, G. Vampa, and T. Brabec, "Tunneling time, what is its meaning?," *Journal of Physics: Conference Series*, vol. 594, p. 012019, 2015.

[103] Z. S. Wang, L. C. Kwek, C. H. Lai, and C. H. Oh, "Quantum tunneling time," *American Journal of Physics*, vol. 73, pp. 23–27, 2005.

[104] T. Zimmermann, S. Mishra, B. R. Doran, D. F. Gordon, and A. S. Landsman, "Tunneling Time and Weak Measurement in Strong Field Ionization," *Physical Review Letters*, vol. 116, p. 233603, 2016.

[105] M. Klaiber, K. Z. Hatsagortsyan, and C. H. Keitel, "Tunneling dynamics in multiphoton ionization and attoclock calibration," *Physical Review Letters*, vol. 114, p. 083001, 2015.

[106] P. B. Corkum, "Plasma perspective on strong field multiphoton ionization," *Physical Review Letters*, vol. 71, pp. 1994–1997, 1993.

[107] B. Wolter, M. G. Pullen, A. T. Le, M. Baudisch, K. Doblhoff-Dier, A. Senftleben, M. Hemmer, C. D. Schröter, J. Ullrich, T. Pfeifer, R. Moshammer, S. Gräfe, O. Vendrell, C. D. Lin, and J. Biegert, "Ultrafast electron diffraction imaging of bond breaking in di-ionized acetylene," *Science*, vol. 354, pp. 308–312, 2016.

[108] C. Figueira de Morisson Faria and X. Liu, "Electron-electron correlation in strong laser fields," *Journal of Modern Optics*, vol. 58, pp. 1076–1131, 2011.

[109] W. Becker, X. Liu, P. J. Ho, and J. H. Eberly, "Theories of photoelectron correlation in laser-driven multiple atomic ionization," *Reviews of Modern Physics*, vol. 84, pp. 1011–1043, 2012.

[110] K. J. Schafer and K. C. Kulander, "Energy analysis of time-dependent wave functions: Application to above-threshold ionization," *Physical Review A*, vol. 42, pp. 5794–5797, 1990.

[111] H. G. Muller and F. C. Kooiman, "Bunching and focusing of tunneling wave packets in enhancement of high-order above-threshold ionization," *Physical Review Letters*, vol. 81, pp. 1207–1210, 1998.

[112] G. G. Paulus, W. Nicklich, H. Xu, P. Lambropoulos, and H. Walther, "Plateau in above threshold ionization spectra," *Physical Review Letters*, vol. 72, pp. 2851–2854, 1994.

[113] L. Seiffert, *Semi-classical description of near-field driven attosecond photoemission from nanostructures*. PhD thesis, Universität Rostock, 2018.

[114] Q. Liu, L. Seiffert, A. Trabattoni, M. C. Castrovilli, M. Galli, P. Rupp, F. Frassetto, L. Poletto, M. Nisoli, E. Rühl, F. Krausz, T. Fennel, S. Zherebtsov, F. Calegari, and M. F. Kling, "Attosecond streaking metrology with isolated nanotargets," *Journal of Optics*, vol. 20, p. 024002, 2018.

[115] J. Jackson, *Classical Electrodynamics*. New York: Wiley, 1999.

[116] C. F. Bohren and D. R. Huffman, *Absorption and Scattering of Light by Small Particles*. Wiley, 1983.

[117] G. Mie, "Beiträge zur Optik trüber Medien, speziell kolloidaler Metallösungen," *Annalen der Physik*, vol. 330, pp. 377–445, 1908.

[118] Y. Mairesse and F. Quéré, "Frequency-resolved optical gating for complete reconstruction of attosecond bursts," *Physical Review A - Atomic, Molecular, and Optical Physics*, vol. 71, p. 011401, 2005.

[119] G. L. Tan, M. F. Lemon, and R. H. French, "Optical Properties and London Dispersion Forces of Amorphous Silica Determined by Vacuum Ultraviolet Spectroscopy and Spectroscopic Ellipsometry," *Journal of the American Ceramic Society*, vol. 86, pp. 1885–1892, 2003.

[120] W. Stöber, A. Fink, and E. Bohn, "Controlled growth of monodisperse silica spheres in the micron size range," *Journal of Colloid and Interface Science*, vol. 26, pp. 62–69, 1968.

[121] X. Wang, A. Gidwani, S. L. Girshick, and P. H. McMurry, "Aerodynamic focusing of nanoparticles: II. Numerical simulation of particle motion through aerodynamic lenses," *Aerosol Science and Technology*, vol. 39, pp. 624–636, 2005.

[122] D. W. Chandler and P. L. Houston, "Two-dimensional imaging of state-selected photodissociation products detected by multiphoton ionization," *The Journal of Chemical Physics*, vol. 87, pp. 1445–1447, 1987.

[123] A. T. Eppink and D. H. Parker, "Velocity map imaging of ions and electrons using electrostatic lenses: Application in photoelectron and photofragment ion imaging of molecular oxygen," *Review of Scientific Instruments*, vol. 68, pp. 3477–3484, 1997.

[124] C. Bartels, C. Hock, J. Huwer, R. Kuhnen, J. Schwöbel, and B. Von Issendorff, "Probing the angular momentum character of the valence orbitals of free sodium nanoclusters," *Science*, vol. 323, pp. 1323–1327, 2009.

[125] J. C. Pinaré, B. Baguenard, C. Bordas, and M. Broyer, "Photoelectron imaging spectroscopy of small clusters: Evidence for non-boltzmannian kinetic-energy distribution in thermionic emission," *Physical Review Letters*, vol. 81, pp. 2225–2228, 1998.

[126] T. Suzuki, L. Wang, and H. Kohguchi, "Femtosecond time-resolved photoelectron imaging on ultrafast electronic dephasing in an isolated molecule," *Journal of Chemical Physics*, vol. 111, pp. 4859–4861, 1999.

[127] V. Dribinski, A. Ossadtchi, V. A. Mandelshtam, and H. Reisler, "Reconstruction of Abel-transformable images: The Gaussian basis-set expansion Abel transform method," *Review of Scientific Instruments*, vol. 73, p. 2634, 2002.

[128] V. Schyja, T. Lang, and H. Helm, "Channel switching in above-threshold ionization of xenon," *Physical Review A - Atomic, Molecular, and Optical Physics*, vol. 57, pp. 3692–3697, 1998.

[129] F. Süßmann, S. Zherebtsov, J. Plenge, N. G. Johnson, M. Kbel, A. M. Sayler, V. Mondes, C. Graf, E. Rhl, G. G. Paulus, D. Schmischke, P. Swrschek, and M. F. Kling, "Single-shot velocity-map imaging of attosecond light-field control at kilohertz rate," *Review of Scientific Instruments*, vol. 82, p. 093109, 2011.

[130] F. Süßmann, *Attosecond dynamics of nano-localized fields probed by photoelectron spectroscopy*. PhD thesis, Ludwig-Maximilians-Universität München, 2013.

[131] T. Brabec, *Strong Field Laser Physics*. 2009.

[132] T. Brabec and F. Krausz, "Nonlinear optical pulse propagation in the single-cycle regime," *Physical Review Letters*, vol. 78, pp. 3282–3285, 1997.

[133] V. Pervak, I. Ahmad, M. K. Trubetskov, A. V. Tikhonravov, and F. Krausz, "Double-angle multilayer mirrors with smooth dispersion characteristics," *Optics Express*, vol. 17, p. 7943, 2009.

[134] F. Lücking, A. Trabattoni, S. Anumula, G. Sansone, F. Calegari, M. Nisoli, T. Oksenhendler, and G. Tempea, "In situ measurement of nonlinear carrier-envelope phase changes in hollow fiber compression," *Optics Letters*, vol. 39, pp. 2302–2305, 2014.

[135] I. J. Sola, E. Mével, L. Elouga, E. Constant, V. Strelkov, L. Poletto, P. Villoresi, E. Benedetti, J. P. Caumes, S. Stagira, C. Vozzi, G. Sansone, and M. Nisoli, "Controlling attosecond electron dynamics by phase-stabilized polarization gating," *Nature Physics*, vol. 2, pp. 319–322, 2006.

[136] S. Skruszewicz, J. Passig, A. Przystawik, N. X. Truong, M. Köther, J. Tiggesbäumker, and K. H. Meiwes-Broer, "A new design for imaging of fast energetic electrons," *International Journal of Mass Spectrometry*, vol. 365-366, pp. 338–342, 2014.

[137] L. Poletto, S. Bonora, M. Pascolini, and P. Villoresi, "Instrumentation for analysis and utilization of extreme-ultraviolet and soft x-ray high-order harmonics," *Review of Scientific Instruments*, vol. 75, pp. 4413–4418, 2004.

[138] M. Schultze, M. Fieß, N. Karpowicz, J. Gagnon, M. Korbman, M. Hofstetter, S. Neppl, A. L. Cavalieri, Y. Komninos, T. Mercouris, C. A. Nicolaides, R. Pazourek, S. Nagele, J. Feist, J. Burgdörfer, A. M. Azzeer, R. Ernstorfer, R. Kienberger, U. Kleineberg, E. Goulielmakis, F. Krausz, and V. S. Yakovlev, "Delay in photoemission," *Science*, vol. 328, pp. 1658–1662, 2010.

[139] K. R. Wilson, Z. Shengli, S. Jinian, E. Rühl, S. R. Leone, G. C. Schatz, M. Ahmed, S. Zou, J. Shu, E. Rühl, S. R. Leone, G. C. Schatz, and M. Ahmed, "Size-Dependent Angular Distributions of Low-Energy Photoelectrons Emitted from NaCl Nanoparticles," *Nano Letters*, vol. 7, pp. 2014–2019, 2007.

[140] R. Signorell, M. Goldmann, B. L. Yoder, A. Bodi, E. Chasovskikh, L. Lang, and D. Luckhaus, "Nanofocusing, shadowing, and electron mean free path in the photoemission from aerosol droplets," *Chemical Physics Letters*, vol. 658, pp. 1–6, 2016.

[141] D. Schomas, N. Rendler, J. Krull, R. Richter, and M. Mudrich, "A compact design for velocity-map imaging of energetic electrons and ions," *Journal of Chemical Physics*, vol. 147, p. 13942, 2017.

[142] G. G. Paulus, W. Becker, W. Nicklich, and H. Walther, "Rescattering effects in above-threshold ionization: a classical model," *Journal of Physics B: Atomic, Molecular and Optical Physics*, vol. 27, pp. L703–L708, 1994.

[143] E. P. Wigner, "Lower limit for the energy derivative of the scattering phase shift," *Physical Review*, vol. 98, pp. 145–147, 1955.

[144] O. Smirnova, A. S. Mouritzen, S. Patchkovskii, and M. Y. Ivanov, "Coulomb-laser coupling in laser-assisted photoionization and molecular tomography," *Journal of Physics B: Atomic, Molecular and Optical Physics*, vol. 40, pp. F197–F206, 2007.

[145] C. H. Zhang and U. Thumm, "Electron-ion interaction effects in attosecond time-resolved photoelectron spectra," *Physical Review A - Atomic, Molecular, and Optical Physics*, vol. 82, p. 43405, 2010.

[146] S. Nagele, R. Pazourek, J. Feist, K. Doblhoff-Dier, C. Lemell, K. Tókési, and J. Burgdörfer, "Time-resolved photoemission by attosecond streaking: Extraction of time information," *Journal of Physics B: Atomic, Molecular and Optical Physics*, vol. 44, pp. 81001–81007, 2011.

[147] J. M. Dahlström, D. Guénot, K. Klünder, M. Gisselbrecht, J. Mauritsson, A. L'Huillier, A. Maquet, and R. Taïeb, "Theory of attosecond delays in laser-assisted photoionization," *Chemical Physics*, vol. 414, pp. 53–64, 2013.

[148] S. Tanuma, C. J. Powell, and D. R. Penn, "Calculations of electron inelastic mean free paths," *Surface and Interface Analysis*, vol. 25, pp. 25–35, 2005.

[149] J. C. Ashley and V. E. Anderson, "Interaction of Low-Energy Silicon Dioxide," *Journal of Electron Spectroscopy and Related Phenomena*, vol. 24, pp. 127–148, 1981.

[150] A. Akkerman, T. Boutboul, A. Breskin, R. Chechik, A. Gibrekhterman, and Y. Lifshitz, "Inelastic electron interactions in the energy range 50 eV to 10 keV in insulators: Alkali halides and metal oxides," *Physica Status Solidi (B) Basic Research*, vol. 198, pp. 769–784, 1996.

[151] A. G. Borisov, P. M. Echenique, and A. K. Kazansky, "Attostreaking with metallic nano-objects," *New Journal of Physics*, vol. 14, p. 023036, 2012.

[152] C. Varin, C. Peltz, T. Brabec, and T. Fennel, "Attosecond plasma wave dynamics in laser-driven cluster nanoplasmas," *Physical Review Letters*, vol. 108, p. 175007, 2012.

[153] I. Georgescu, U. Saalmann, and J. M. Rost, "Attosecond resolved charging of ions in a rare-gas cluster," *Physical Review Letters*, vol. 99, p. 183002, 2007.

[154] D. D. Hickstein, P. Ranitovic, S. Witte, X. M. Tong, Y. Huismans, P. Arpin, X. Zhou, K. E. Keister, C. W. Hogle, B. Zhang, C. Ding, P. Johnsson, N. Toshima, M. J. Vrakking, M. M. Murnane, and H. C. Kapteyn, "Direct visualization of laser-driven electron multiple scattering and tunneling distance in strong-field ionization," *Physical Review Letters*, vol. 109, p. 073004, 2012.

[155] Q. Liu, S. Zherebtsov, L. Seiffert, S. Skruszewicz, and D. Zietlow, "All-optical spatio-temporal control of electron emission from SiO2 nanospheres with femtosecond two-color laser fields," *New Journal of Physics*, vol. 21, p. 073011, 2019.

[156] P. Hommelhoff and M. F. Kling, "Attosecond Nanophysics: From Basic Science to Applications," 2015.

[157] S. H. Chew, A. Gliserin, J. Schmidt, H. Bian, S. Nobis, F. Schertz, M. Kübel, Y. Y. Yang, B. Loitsch, T. Stettner, J. J. Finley, C. Späth, H. Ouacha, A. M. Azzeer, and U. Kleineberg, "Laser intensity effects in carrier-envelope phase-tagged time of flight-photoemission electron microscopy," *Applied Physics B: Lasers and Optics*, vol. 122, p. 102, 2016.

[158] S. E. Irvine, P. Dombi, G. Farkas, and A. Y. Elezzabi, "Influence of the carrier-envelope phase of few-cycle pulses on ponderomotive surface-plasmon electron acceleration," *Physical Review Letters*, vol. 97, p. 146801, 2006.

[159] P. Rácz, S. E. Irvine, M. Lenner, A. Mitrofanov, A. Baltuška, A. Y. Elezzabi, and P. Dombi, "Strong-field plasmonic electron acceleration with few-cycle, phase-stabilized laser pulses," *Applied Physics Letters*, vol. 98, p. 111116, 2011.

[160] J. Passig, S. Zherebtsov, R. Irsig, M. Arbeiter, C. Peltz, S. Göde, S. Skruszewicz, K. H. Meiwes-Broer, J. Tiggesbäumker, M. F. Kling, and T. Fennel, "Nanoplasmonic electron acceleration by attosecond-controlled forward rescattering in silver clusters," *Nature Communications*, vol. 8, p. 1181, 2017.

[161] T. Paschen, M. Förster, M. Krüger, C. Lemell, G. Wachter, F. Libisch, T. Madlener, J. Burgdörfer, and P. Hommelhoff, "High visibility in two-color above-threshold photoemission from tungsten nanotips in a coherent control scheme," *Journal of Modern Optics*, vol. 64, pp. 1054–1060, 2017.

[162] Q. Liu, S. Zherebtsov, F. Süßmann, J. Passig, L. Seiffert, V. Mondes, A. Kessel, C. Graf, E. Rühl, J. Tiggesbäumker, K. H. Meiwes-Broer, M. I. Stockman, L. Veisz, S. Karsch, T. Fennel, and M. Kling, "Sub-cycle Metallization of SiO_2 Nanoparticles Probed via Carrier- Envelope Phase Dependent Electron Acceleration," *in preparation*, 2019.

[163] S. Zherebtsov, A. Wirth, T. Uphues, I. Znakovskaya, O. Herrwerth, J. Gagnon, M. Korbman, V. S. Yakovlev, M. J. J. Vrakking, M. Drescher, and M. F. Kling, "Attosecond imaging of XUV-induced atomic photoemission and Auger decay in strong laser fields," *Journal of Physics B: Atomic, Molecular and Optical Physics*, vol. 44, p. 105601, 2011.

[164] J. E. A. P. Owell, A. D. A. M. M. S. Ummers, Q. Ingcao, L. Iu, S. E. J. A. R. Obatjazi, P. H. R. Upp, J. Ohannes, S. Tierle, C. A. T. R. Errero, M. F. Atthias, K. Ling, and A. R. R. Udenko, "Interplay of pulse duration , peak intensity , and particle size in laser-driven electron emission from silica nanospheres," *Optics Express*, vol. 27, p. 027124, 2019.

[165] Jean-Claude Diels and Wolfgang Rudolph, *Ultrashort Laser Pulse Phenomena: Fundamentals, Techniques, and Applications on a Femtosecond Time Scale*. San Diego CA, USA: Academic Press, 2006.

[166] R. Adair, L. L. Chase, and S. A. Payne, "Nonlinear refractive index of optical crystals," *Physical Review B*, vol. 39, pp. 3337–3350, 1989.

[167] Leonid V. Keldysh, "Ionization in the Field of a Strong Electromagnetic Wave," *Journal of Experimental and Theoretical Physics*, vol. 47, pp. 1945–1957, 1964.

[168] L. Sudrie, A. Couairon, M. Franco, B. Lamouroux, B. Prade, S. Tzortzakis, A. Mysyrowicz, . L. Sudrie, A. Couairon, M. Franco, B. Lamouroux, B. Prade, S. Tzortzakis, A. Mysyrowicz, L. Sudrie, A. Couairon, M. Franco, B. Lamouroux, B. Prade, S. Tzortzakis, and A. Mysyrowicz, "Femtosecond Laser-Induced Damage and Filamentary Propagation in Fused Silica," *Physical Review Letters*, vol. 89, p. 186601, 2002.

[169] V. E. Gruzdev, "Laser-induced ionization of solids: back to Keldysh," *Laser-Induced Damage In Optical Materials: 2004*, vol. 5647, pp. 480–492, 2005.

[170] B. C. Stuart, M. D. Feit, A. M. Rubenchik, B. W. Shore, and M. D. Perry, "Laser-induced damage in dielectrics with nanosecond to subpicosecond pulses," *Physical Review Letters*, vol. 74, pp. 2248–2251, 1995.

[171] B. C. Stuart, M. D. Feit, S. Herman, A. M. Rubenchik, B. W. Shore, and M. D. Perry, "Optical ablation by high-power short-pulse lasers," *Journal of the Optical Society of America B*, vol. 13, pp. 459–468, 1996.

[172] B. Stuart, M. Feit, S. Herman, A. Rubenchik, B. Shore, and M. Perry, "Nanosecond-to-femtosecond laser-induced breakdown in dielectrics," *Physical Review B - Condensed Matter and Materials Physics*, vol. 53, pp. 1749–1761, 1996.

[173] M. Sparks and C. Duthler, *Theoretical studies of high-power ultraviolet and infrared materials*. Van Nuys, CA: Xonics Inc, 1975.

[174] K. K. Thornber, "Applications of scaling to problems in high-field electronic transport," *Journal of Applied Physics*, vol. 52, pp. 279–290, 1981.

[175] N. Bloembergen, "Laser Induced Electric Breakdown in Solids," *IEEE Journal of Quantum Electronics*, vol. 10, pp. 375–386, 1974.

[176] A. Q. Wu, I. H. Chowdhury, and X. Xu, "Femtosecond laser absorption in fused silica: Numerical and experimental investigation," *Physical Review B - Condensed Matter and Materials Physics*, vol. 72, p. 085128, 2005.

[177] X. Jing, J. Shao, J. Zhang, Y. Jin, H. He, and Z. Fan, "Calculation of femtosecond pulse laser induced damage threshold for broadband antireflective microstructure arrays," *Optics Express*, vol. 17, p. 24137, 2009.

[178] E. G. Gamaly and A. V. Rode, "Transient optical properties of dielectrics and semiconductors excited by an ultrashort laser pulse," *Journal of the Optical Society of America B*, vol. 31, p. C36, 2014.

[179] Q. Sun, H. Jiang, Y. Liu, Z. Wu, H. Yang, and Q. Gong, "Measurement of the collision time of dense electronic plasma induced by a femtosecond laser in fused silica," *Optics Letters*, vol. 30, p. 320, 2005.

[180] P. A. Zhokhov and A. M. Zheltikov, "Optical breakdown of solids by few-cycle laser pulses," *Scientific Reports*, vol. 8, p. 1824, 2018.

Acknowledgements

Throughout this thesis I presented my participation in all the experiments discussed and our contributions to the overall scientific community. None of the work could have been done without those who have helped and encouraged me. It is the time to express my gratitude to those who have made this thesis possible.

First of all, I would like to express my earnest gratitude to my supervisor, Prof. Matthias Kling, who provided me a great scientific training throughout my doctoral studies. I am grateful for his patience in scientific discussions during my doctoral research work. He has sent me to a number of conferences/workshops and involved me in large collaborative projects. His enthusiasm and helpful suggestions increased my motivation of going even deeper into the essence of my work. I have learnt the virtue of optimism and continuous efforts in general from him. Matthias also cares about my living as a foreigner in Munich. He applied fund to cover my oral English training courses in the first year. Moreover, he generously offered part of his house to me for three months right after he knew that I could not find an apartment in time. What a luck to have a such fantastic supervisor!

For the initiating of my doctoral study, I would like to thank Prof. Bitao Hu from the department of nuclear physics and technology of Lanzhou University for guiding me in scientific research since 2009, and encouraging me to study abroad afterwards. Special thanks to the China Scholarship Council (CSC) for awarding me a four years scholarship, which is the foundation of everything. I thank Jing Jia and Dr. Yanling Guo from the Lanzhou University who kindly being my guarantees for my doctoral study.

For the good start into the work, I am so honoured to be part of Kling group, which is an excellent team. I would like to thank all group members, Dr. Sergey Zherebtsov, Dr. Hirofumi Yanagisawa, Dr. Boris Bergues, Dr. Philipp Rupp, Dr. Shaohua Sun, Dr. Zilong Wang, Dr. Shubhadeep Biswas, Johannes Schötz, Dziugas Kimbaras, Jia Mei, Sambit Mitra, Marcel Neuhaus, Philipp Rosenberger, Maximilian Seeger as well as the former members Dr. Nora Kling, Dr. Hui Li, Dr. Matthias Kübel, Dr. Frederik Süßmann, Johannes Stierle, Dr. William Okell, Dr. Pawel Wnuk, Dr. Harald Fuest, Dr. Benjamin Förg, Dr. Christian Burger and Seongjin Ahn. You guys always help each other generously. It was amazing experiences to be colleagues and friends with you. Many thanks to Dr. Hui Li and Dr. Nora Kling for helping me overcome the culture shock at the very beginning of my staying in Munich. I also appreciate Dr. Sergey Zherebtsov, Dr. Frederik Süßmann and Dr. Philipp Rupp for guiding me into the nanoparticle world, and sharing with me really

helpful experiences in the lab. I would also thank Prof. Matthias Kling, Dr. Christian Burger, Marcel Neuhaus and Philipp Rosenberger for teaching me skiing during our group excursions in Alps.

As the work in this thesis was done with tight worldwide collaborations, I am deeply indebted to Prof. Thomas Fennel and Dr. Lennart Seiffert from the University of Rostock for providing us with most of the theoretical support and involving me in the experimental campaign at SLAC. Special thanks go to Prof. Francesca Calegari from the University of Hamburg and her group members Dr. Andrea Trabattoni, Dr. Erik Mansson, Dr. Mara Galli and Vincent Wanie for carrying out the pump-probe measurements on their state-of-the-art laser systems. I would like to thank Prof. Stefan Karsch, Dr. Sergei Trushin, Dr. Vyacheslav Leshchenko and Dr. Alexander Kessel from the Max Planck Institute of Quantum Optics for sharing the laser beam time and helping us build up the FemtoPower laser lab. I would also like to thank Prof. Eckart Rühl from the Freie Universität Berlin and Prof. Markus Gallei from the Saarland University for providing us with the nanoparticle samples.

I would like to thank all my supportive friends, Dr. Jinwei Zhang, Jinzhao Li, Yu Qin, Dr. Zaijun Chen, Dr. Jia Xu, *et al.*. The environment created by you in Munich has reduced my homesickness and led to a joyful experience. So many sweet memories come to my mind whenever I recall your names.

Finally, I have to express my highest respect and deepest gratitude to my parents, my brother and my sister for their support and encouragement in all the steps that I have taken over the years, and to my dear wife for her endless love and accompaniment!